Diss. ETH No. 15104

Phase Transitions in Quantum Condensed Matter

A dissertation submitted to the

SWISS FEDERAL INSTITUTE OF TECHNOLOGY ZÜRICH
(ETH Zürich)

for the degree of
Doctor of Natural Science

presented by

HANS PETER BÜCHLER

Dipl. Phys. ETH
born December 5, 1973
Swiss citizien

accepted on the recommendation of
Prof. Dr. J. W. Blatter, examiner
Prof. Dr. W. Zwerger, co-examiner
PD. Dr. V. B. Geshkenbein, co-examiner

2003

Abstract

In this thesis, phase transitions in superconducting metals and ultra-cold atomic gases (Bose-Einstein condensates) are studied. Both systems are examples of quantum condensed matter, where quantum effects operate on a macroscopic level. Their main characteristics are the condensation of a macroscopic number of particles into the same quantum state and their ability to sustain a particle current at a constant velocity without any driving force. Pushing these materials to extreme conditions, such as reducing their dimensionality or enhancing the interactions between the particles, thermal and quantum fluctuations start to play a crucial role and entail a rich phase diagram. It is the subject of this thesis to study some of the most intriguing phase transitions in these systems.

Reducing the dimensionality of a superconductor one finds that fluctuations and disorder strongly influence the superconducting transition temperature and eventually drive a superconductor to insulator quantum phase transition. In one-dimensional wires, the fluctuations of Cooper pairs appearing below the mean-field critical temperature T_{c0} define a finite resistance via the nucleation of thermally activated phase slips, removing the finite temperature phase transition. Superconductivity possibly survives only at zero temperature. The focus then is shifted on the quantum nucleation of phase slips which may trigger a superconductor to insulator transition. The transition present in infinite wires disappears in realistic wires of finite length. Here, we analyze the bosonic Cooper pair fluctuations in such realistic wires which are naturally coupled to their environment through the boundaries. We find, that the coupling to the environment provides the resurrection of a transition in the environmental parameters. The insulating state is characterized via the opening of an excitation gap. We discuss the phase diagram with different regimes exhibiting insulating and strong/weak superconducting behavior and identify distinctive features in the current-voltage characteristic pointing to these phases.

Strong quantum fluctuations are present in atomic gases confined to one dimension as well. The absence of an environment allowing for dissipative processes modifies the phase diagram. Probing the superfluid response in an atomic gas, we find that the perturbation itself acts as nucleation point for quantum phase slips. We study the response in two geometries: while in a ring the quantum nucleation of phase slips is quenched, they proliferate in a finite tube with Bloch oscillations appearing at low driving velocities.

In a recent experiment, it has been shown that subjecting a Bose-Einstein condensate to an optical lattice allows to increase the effect of interactions and drive the system through a superfluid to Mott insulator transition. Here, we study this transition in one dimension. In this geometry, the strongly interacting limit with large phase fluctuations is achieved by either increasing the strength of the optical lattice or by increasing the transverse confinement. We map the problem in the weak- and strong confinement limit to two classical problems, the Bose-Hubbard model and the sine-Gordon model, respectively. Using this mapping we derive the complete phase diagram. The superfluid to Mott insulator transition is closely related to the superconductor to insulator transition in long superconducting wires. In both systems, the insulating phase is characterized by the opening of an excitation gap and the disappearance of phase coherence.

The recent progress in sympathetic cooling of bosons and fermions allows for the realization of degenerate Fermi gases. These Bose-Fermi mixtures represent a highly tunable laboratory system allowing for the realization of complex quantum phases. Subjecting such a two-dimensional Bose-Fermi mixture to an optical lattice, we demonstrate the emergence of a supersolid phase within the weak coupling description. A supersolid combines the main characteristics of superfluids, the presence of a condensate and superfluid stiffness, with crystalline order usually present in solids. Within this system the supersolid phase appears via a fermionic density wave instability, which in turn imprints a bosonic density modulation. We study the phase diagram in the weak coupling limit, where the supersolid instability competes with an instability towards phase separation.

The continuing miniaturization of devices has reached system sizes of ten nanometers, where quantum effects start to play a crucial role. The phase transitions studied in this dissertation provide fundamental insight into the behavior of quantum condensed matter under such extreme conditions. The deeper understanding gained in these model systems is important for the development of future technologies and further progress in miniaturization.

Kurzfassung

In der vorliegenden Dissertation werden Phasenübergänge in supraleitenden Metallen und in ultrakalten atomaren Gasen (Bose-Einstein Kondensate) untersucht. Beide Systeme sind Beispiele quantenkondensierter Materie, in der Quanteneffekte auf einem makroskopischen Niveau erscheinen. Ihre herausragendsten Eigenschaften sind die Kondensation einer makroskopischen Anzahl von Teilchen in denselben Quantenzustand und die Fähigkeit zum Transport eines verlustfreien Teilchenstromes. Setzt man diese Materialien extremen Bedingungen aus, wie zum Beispiel einer dimensionellen Reduktion oder einer starken Wechselwirkung zwischen den Teilchen, so spielen thermische und quantenmechanische Fluktuationen eine wichtige Rolle und bringen ein reichhaltiges Phasendiagramm hervor. In dieser Dissertation werden ausgewählte Phasenübergänge in diesen Systemen untersucht.

In niedrigdimensionalen Supraleitern unterdrücken Fluktuationen und Unordnung die kritische Temperatur des Supraleiters und können gar einen Phasenübergang zwischen dem Supraleiter und einem Isolator hervorrufen. Die starken Fluktuationen von Cooperpaaren, welche unterhalb der Paarungstemperatur T_{c0} erscheinen, führen via Nukleation von thermischen Phasensprüngen zu einem endlichen Widerstand in eindimensionalen Drähten. Der thermodynamische Phasenübergang bei endlichen Temperaturen verschwindet und Supraleitung kann nur noch beim absoluten Nullpunkt überleben. Das Interesse richtet sich dann auf die Nukleation von quantenmechanischen Phasensprüngen, welche einen Phasenübergang vom Supraleiter zum Isolator treiben können. Die Fluktuationen der bosonischen Cooperpaare in realistischen Drähten mit endlicher Länge koppeln mit der Umgebung. Der Übergang, welcher in unendlich langen Drähten vorhanden ist, verschwindet in endlichen Drähten. Andererseits erzeugt die Kopplung des Drahtes mit der Umgebung einen neuen Phasenübergang im Umgebungsparameter. Der isolierende Grundzustand ist durch eine Energielücke im Anregungspektrum ausgezeichnet. In der vorliegenden Arbeit untersuchen wir das Phasendiagramm und beschreiben die Strom-Spannungscharakteristik der einzelnen Phasen.

Ein ähnlicher Vorgang ist in eindimensionalen Bose-Einstein Kondensaten zubeobachten. Da keine dämpfenden Prozesse durch die Umgebung vorhanden sind, wird das Phasendiagramm verändert. Die Untersuchung der superfluiden Antwort verlangt eine Störung im Medium, welche selber als Nukleationskeim quantenmechanischer Phasensprünge wirkt. Wir untersuchen zwei Geometrien mit endlicher Länge: in einem Ring ist die quantenmechanische Nukleation von Phasensprüngen verboten was eine superfluide Antwort hervorruft, während Phasensprünge in einem Tubus von endlicher Länge massenweise entstehen und eine nicht-superfluide Antwort bei kleinen Treibergeschwindigkeiten verursachen.

In einem kürzlich durchgeführten Experiment in atomaren Gasen, wurde ein Phasenübergang von einem Superfluidum zum Mottisolator beobachtet. Dieser Übergang ist getrieben durch die Präsenz eines optischen Gitters, welches es erlaubt den Einfluss von Wechselwirkungen zu verstärken. In dieser Arbeit wird dieser Übergang in eindimensionalen Systemen untersucht. Der stark wechselwirkende Grenzfall mit ausgeprägten quantenmechanischen Fluktuationen wird entweder durch ein starkes optisches Gitterpotential oder durch extremes Einsperren in einer Dimension erreicht. Dieser Übergang kann durch die Abbildung auf zwei klassische Modelle, das Bose-Hubbard Modell und das Sine-Gordon Modell beschrieben werden. Der Übergang ist eng verbunden mit dem Übergang vom Supraleiter zum Isolator in metallischen Systemen.

Der kürzlich erzielte Fortschritt beim Kühlen von Bose-Fermi Mischungen ermöglicht das Erreichen der fermionischen Quantenentartung. Diese Systeme von Bose-Fermi Mischungen erlauben die Analyse von komplexen Quantenphasen. In dieser Arbeit wird das Erscheinen eines Superkristalles in zweidimensionalen Bose-Fermi Mischungen unter dem Einfluss eines optischen Gitters demonstriert. Ein Superkristall kombiniert die superfluide Antwort mit der kristallinen Struktur eines Festkörpers. Der Superkristall entsteht durch eine Dichtewelleninstabilität der Fermionen, welche auch eine Dichtemodulation der Bosonen nach sich zieht. Wir untersuchen das Phasendiagramm im Grenzfall schwacher Wechselwirkung und analysieren das kompetitive Verhalten zwischen der Superkristallinstabilität und der Phasenseparation.

Elektronische Schaltkreise haben dank fortschreitender Miniaturisierung Grössen im Nanometerbereich erreicht wo Quanteneffekte ein wichtige Rolle spielen. Die Phasenübergänge, die in dieser Dissertation untersucht werden, ermöglichen eine tiefere Einsicht in das Verhalten von quantenkondensierter Materie unter solch extremen Bedingungen. Das in diesen Systemen gewonnene Wissen ermöglicht die Entwickelung von neuen Bauteilen und weitere Fortschritte in der Miniaturisierung technologisch relevanter Systeme.

Contents

Abstract **iii**

Kurzfassung **v**

1 Introduction **1**

2 Thin Superconducting Wires **13**

2.1 Introduction 13

2.2 Voltage-biased vs. current-biased circuits 16

2.3 Superconducting wire and environment 22

2.4 Instanton Expansion 25

2.5 Zero temperature phase diagram 28

2.5.1 Infinite system 28

2.5.2 Wires with finite length L 30

2.6 Current-Voltage characteristic 39

2.6.1 Superconducting phase 39

2.6.2 Insulating phase 43

2.7 Conclusions 45

3 Superfluidity versus Bloch Oscillations **51**

3.1 Introduction 51

3.2 Experimental setups 53

3.3 Effective Action 55

3.3.1 Integrating out the impurity 58

3.3.2 Integrating out the leads 59

3.3.3 Action for the phase difference 60

3.4 Infinite Geometry 62

3.4.1 Thermodynamics 62

3.4.2 Quantum Nucleation of Phase Slips 63
3.5 Finite Geometries 65
3.5.1 Ring 66
3.5.2 Tube 69
3.6 Conclusions 74

4 Commensurate-Incommensurate Transition 77
4.1 Introduction 77
4.2 Boson Hamiltonian 80
4.3 Weakly interacting bosons 81
4.3.1 Derivation of the Bose-Hubbard model 81
4.3.2 Phase diagram for $\gamma \ll 1$ 83
4.4 Strongly interacting bosons 85
4.4.1 Derivation of the sine-Gordon model 86
4.4.2 Phase diagram for $\gamma \gg 1$ 89
4.5 Influence of a trapping potential 92
4.6 Discussion and conclusions 96

5 Supersolid versus Phase Separation 101
5.1 Introduction 101
5.2 Bose-Fermi mixtures 104
5.2.1 Hamiltonian within tight-binding approximation 104
5.2.2 Effective boson Hamiltonian 107
5.3 Phase separation 108
5.3.1 Instability at $q = 0$ 108
5.3.2 Thomas-Fermi approximation 109
5.3.3 Phase diagram 112
5.4 Supersolids 113
5.4.1 Instability at $\mathbf{k}_{\mathrm{DW}}$ 113
5.4.2 Mean field theory 115
5.5 Phase diagram and conclusions 119

A Quantum Nucleation Rates 123

B Modified Renormalization Group Equation 127

C Path Integral Approach 131

D General concepts 133
D.1 The boundary sine-Gordon problem 133
D.2 Application to physical relevant systems 135
    D.2.1 Luttinger liquid with impurity 135
    D.2.2 Particle in periodic potential with damping 137
D.3 Quantitative Comparison 138

List of Figures

1.1 Classical and quantum mechanical state 3
1.2 Superfluid and Mott insulator states 8

2.1 Preview of the phase diagram 15
2.2 Generic setup of an environment 17
2.3 Model of the environment 20
2.4 Impedances of the device 21
2.5 Phase slip solution in the inifnite system 29
2.6 Kosterlitz-Thouless scaling flow 29
2.7 Mirror vortices 32
2.8 Phase slip solutions with boundary conditions 32
2.9 Renormalization group flow 34
2.10 Phase diagram of a wires with finite length 38
2.11 I-V characteristic in the superconducting phase 42
2.12 I-V characteristic in the insulating phase 44
2.13 Relation between I_s and V_s 47

3.1 Superfluid in a small thin cylindrical trap 54
3.2 Form of the condensate wave function near the impurity 57
3.3 Quantum nucleation rate of phase slips 65
3.4 Effective potential $V(\varphi)$ in a ring 67
3.5 Response 75

4.1 Sketch of the phase diagram for the Bose-Hubbard model 84
4.2 Phase diagram for large $V \gg E_r$ and small interactions $\gamma \ll 1$ . . 85
4.3 Relation between K and γ 87
4.4 The size of the excitation gap Δ 90
4.5 Schematic phase diagram 91

4.6 Different density profiles 94
4.7 Variation of the chemical potential 95
4.8 Fraction of particles in the Mott insulating state 96
4.9 Phase diagram 97

5.1 Sketch of the λ_{FB}-$1/t_{\mathrm{B}}$-T phase diagram 102
5.2 Fermi surface of 2D fermions 106
5.3 Phase diagram of the transition towards phase separation 113
5.4 Degenerated ground state of the supersolid 118
5.5 Sketch of the T-$\Delta\mu$ phase diagram of the supersolid 119
5.6 V_{F}-γ phase diagram at low temperatures 121

Chapter 1

Introduction

The discovery of superconductivity by Kamerlingh Onnes in 1911 marks a milestone in condensed matter physics. He observed that the resistance of various metals vanishes below a material-dependent critical temperature T_c. This perfect conductivity represents the most intriguing property of superconducting materials and is the prerequisite for most of the current applications. A deeper understanding of superconductivity was provided by the microscopic theory developed by Bardeen, Cooper, and Schrieffer [1] (BCS-theory) in 1957 and later on, the derivation of the Ginzburg-Landau theory by Gor'kov [2] in 1959. Their theories show, that superconductivity represents a remarkable example of a phenomenon where quantum effects operate on a truly macroscopic scale. The main characteristic of superconductivity, the ability to sustain particle currents at a constant velocity for long periods of time without any driving force, involves the flow of a macroscopic number of particles all condensed into the same quantum state. This condensation appears via the pairing of electrons with opposite momenta and spin into Cooper pairs, and is an example for quantum condensed matter. Beside the discovery of superconductivity, other examples of quantum condensed matter systems have been discovered, such as superfluid ^{4}He (see Ref. [3]) and the Bose-Einstein condensation of atomic gases [4, 5]. In the following, we will first focus on superconducting systems and discuss superfluid systems and Bose-Einstein condensation later.

The special behavior of quantum condensed matter originates from the appearance of off-diagonal long-range order [6] breaking the $U(1)$ gauge symmetry of the system. This long-range order is often described by a complex order parameter $\psi = |\psi| \exp(i\,\phi)$ with $|\psi|^2$ accounting for the condensate density and the phase ϕ describing the $U(1)$ symmetry breaking. Within superconductivity, the order parameter ψ naturally appears in the phenomenological Ginzburg-Landau theory and describes the behavior of the superconducting electrons. This mean-field theory was extremely successful in explaining many fundamental properties of superconductivity and providing a microscopic foundation of the Ginzburg-Landau theory.

Pushing superconducting materials to extreme conditions, e.g., via reducing their dimension or introducing strong disorder, fluctuations start to play a crucial role and lead to substantial modifications of the mean-field predictions. As a consequence, the distinction between the mean-field critical temperature T_{c0} where the formation of Cooper pairs takes place, and the superconducting transition temperature T_c where long-range order is established, becomes crucial for the description of superconductors. Thin superconducting films undergo a Kosterlitz-Thouless transition at $T_{\rm KT} < T_{c0}$ [7, 8]. At temperatures $T_{\rm KT} < T < T_{c0}$, thermal fluctuations of the order parameter produce free vortices which suppress long-range order. Such vortices are topological excitations where the local superconducting order parameter drops to zero at the center of the vortex core, while the phase exhibits a finite winding around the core region. These vortices move under the influence of a transport current and cause a finite flux-flow resistance. In turn, below $T_{\rm KT}$, topological excitations are bound in vortex-antivortex pairs and quasi long-range order is established; this quasi long-range order is sufficient to provide a superconducting response in the system.

Going over to one-dimensional systems such as thin wires, the situation becomes even more dramatic as the influence of fluctuations is further increased. The thermal nucleation of phase slips removes the finite temperature transition [9, 10, 11, 12] and superconductivity may only survive at zero temperature. However, the resistance decreases exponentially and in real experiments performed on wires with finite length, the time scale for a single phase slip nucleation easily exceeds the experimental time scale. Therefore, such wires behave superconducting at low temperatures.

With further decreasing width of the superconducting wires, the focus is on the observation of phase slips driven by quantum fluctuations [13] and on the possible appearance of a zero temperature quantum phase transition [14]. Such quantum phase slips have been previously predicted to appear in superconducting Josephson junctions [15, 16, 17, 18, 19] and have been observed in a series of experiments [20, 21, 22]. The general behavior of quantum phase slips in

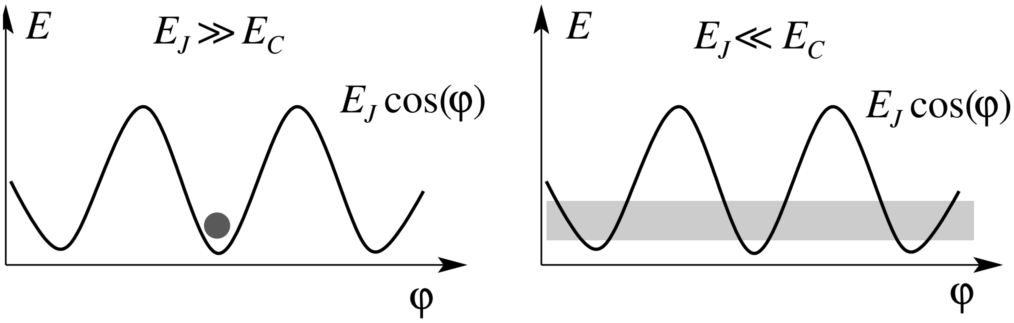

Figure 1.1: Classical versus quantum mechanical state of a Josephson junction. Left: The classical state is characterized by a localized phase within a minima of the periodic potential, which establishes a superconducting response. Right: The quantum ground state exhibits a delocalized phase associated with the opening of an energy band. Two process allow to drive the quantum mechanical ground state into the classic limit: First, for small charging energy $E_C \ll E_J$ the time scale associated with coherent hopping exceeds the observation time. Second, dissipative processes in the environment provide decoherence and localize the phase within a minima of the potential.

Josephson junctions derives from the Hamiltonian describing two weakly coupled superconducting islands

$$H = 4E_C\left(\frac{Q}{\hbar}\right)^2 - E_J\cos\varphi, \tag{1.1}$$

Here, φ is the phase difference across the Josephson junction and the Q conjugate variable, while E_J denotes the Josephson coupling energy and $E_C = e^2/2C$ is the charging energy with C the capacitance of the junction. For a classical system with $Q = \hbar^2\partial_t\varphi/8E_C$, the ground state is phase coherent with $\varphi = 2\pi n$ ($n \in \mathrm{Z}$) and describes a superconducting state, see Fig. 1.1. In turn, allowing for quantum mechanical fluctuations $[\varphi, Q] = i\hbar$, the phase φ delocalizes and it is the charge Q on each superconducting island which becomes the appropriate sharp observable. As a consequence, the system develops a Coulomb gap at low drives. From this quantum mechanical ground state, the superconducting behavior can be recovered by two processes: First, for large capacitance $E_C \ll E_J$, the hopping between different minima decreases exponentially $\sim \sqrt{E_J E_C}\exp(-\sqrt{8E_J/E_C})$ [19], and the time scale for the quantum nucleation of phase slips exceeds the observation time. As a consequence, quantum phenomena are expected to be observed only in small-capacitance Josephson junctions. Second, even in small-capacitance Josephson junctions, the coupling of the superconducting island to the environment introduces dissipative processes providing decoherence. For a current-biased device, the most important model environment involves a parallel shunt resistance R, which can be accounted for by an ohmic bath within a Caldeira-Leggett-type description [17]. The coupling to the environment entails a quantum phase transition at $R = R_Q$ [23, 24] ($R_Q = \pi\hbar/2e^2$ denotes the quantum resistance). For weak dissipation $R > R_Q$, the environment introduces only weak decoherence and the ground state is closely linked to the ground state in the quantum mechanical limit with a delocalized phase. In contrast, for strong dissipation $R < R_Q$ the strong decoherence effects localize the phase within a minimum of the potential and push the system into the classical limit with a superconducting ground state at zero temperature. However, at finite drives the quantum fluctuations still provide modifications in the current-voltage characteristic as compared to its classical counterpart with small charging energies. These effects are generally known as quantum nucleation of phase slips and have been observed by Devoret *et al.* [21]. Furthermore, direct evidence for the quantum phase transition in a resistively shunted Josephson junction has been found recently [25, 26].

The observed destruction of phase coherence in small-capacitance Josephson junctions stimulated an extensive study of quantum effects in ultra-thin superconducting wires. It was first pointed out by Mooij *et al.* [27] that quantum nucleation of phase slips could play an important role in thin wires. Applying instanton methods on a phenomenological time-dependent Ginzburg-Landau equation, Saito and Murayama [28, 29] derived a first estimate for the quantum nucleation rate. Later on, Duan [30] emphasized the relevance of the electromagnetic fields surrounding the superconducting wires. An appropriate description of the superconducting wire taking these effects into account is provided by the effective action theory developed in Ref. [31]. Within this description, the plasma mode acquires a linear spectrum [32, 33] and dominates the dynamics of quantum phase slips [34, 14, 35]. In long wires it was predicted, that the system undergoes a quantum phase transition from a superconducting to an insulating state [14]. Introducing the admittance μ, a parameter characterizing the wire's geometry and electronic structure, the transition takes place at $\mu = 2$. For $\mu > 2$, the wire is superconducting at zero temperature, while at finite temperatures the quantum nucleation of phase slips provides corrections in the current-voltage characteristic. In contrast, for $\mu < 2$ the nucleation of phase slips proliferates, and currents across the wire are blocked by the opening of an excitation gap.

First attempts to observe the quantum phase slips [13] are still debated due to the granular structure of the wires. It has been argued, that the long resistance tails observed at low temperatures were not due to quantum nucleation of phase slips, but rather due to weak links in the wire [30, 36]. In turn, the deviations from the theory for thermal activated phase slips observed on amorphous Pb wires [37] have been interpreted as the consequence of enhanced charge fluctuations. The conclusion that these enhanced charge fluctuations represent a precursor of quantum phase slips, has been hotly debated [38, 14, 39]. Later, experiments on ultrathin wires carried the signature of a superconductor to insulator quantum phase transition [40, 41]. However, the wires used in the experiment are relatively short, which rules out an interpretation in terms of a quantum phase transition predicted in infinite wires [42]. So far, studies of phase slips in finite systems involve a ring geometry where the finite length is introduced via periodic boundary conditions [34, 35], a setup not realized in experimental situations. An understanding of the behavior of quantum phase slips in short system requires to study the influence of the environment on the transport properties of the wire; this analysis is the central topic of Chapter 2.

In addition, the ultrathin wires used in experiments exhibit a high normal resistance indicating that the disorder-induced suppression of superconductivity also plays an important role. A comparison with the situation in thin films shows that disorder decreases the superconducting transition temperature giving way to a superconductor to insulator phase transition [43]. Starting from a microscopic description, the disorder decreases the screening properties of the electrons, which in turn increases the effectiveness of Coulomb interaction and reduces the attraction between the electrons [44, 45, 46]. As a consequence, the mean-field critical temperature decreases and may give way to a superconductor to insulator quantum phase transition in amorphous superconductors. In a different, approach disordered bosons in two dimensions are studied and a superconductor to insulator transition is predicted as well [47, 48]. These results are expected to apply for granular materials [49]. It was pointed out by Oreg and Finkel'stein [50] that a disorder-induced reduction of the mean-field critical temperature plays a crucial role in amorphus ultrathin wires. Recent calculations for the shift in the critical temperature [51, 52] provide a qualitative agreement with experiments on amorphous wires [36]. However, the consistent interpretation of the experimental results found by Bezryadin *et al.* [40] remains an open problem. The complete understanding of the behavior of thin superconducting wires requires a theory combining the influence of disorder and quantum nucleation of phase slips in finite systems. With this motivation for future research, we finish the discourse on superconductivity and focus on a different kind of quantum condensed matter.

Following the study of superconductivity in thin finite wires, we turn to a different example of quantum condensed matter which has been studied in great detail: the superfluid flow in bosonic quantum liquids. Historically, the exploration of superfluids starts with the prediction of a Bose-Einstein condensate for noninteracting bosonic particles at low temperatures, a phenomenon that has attracted physicist's attraction over the last century [53, 54]. The Bose-Einstein condensation appears via a macroscopic occupation of the system's eigenstate with lowest energy. The appearance of such a quantum degeneracy in a bosonic atomic gas requires that the de Broglie wavelength $\lambda_{\mathrm{db}} = \hbar/\sqrt{2mk_{\mathrm{B}}T}$ becomes comparable to the averaged interparticle distance. Below a critical temperature T_c, the formation of a condensate with density n_0 takes place. This condensate density is a thermodynamic quantity characterizing the off-diagonal-long-range order in the system [6]. The first experimental observation of a condensate was achieved in the superfluid phase of liquid ^{4}He. In ^{4}He interactions play a dominant role and the experimentally observed condensate involves about 10% of the particle density, see Ref. [3] for a review. In analogy to superconductivity, this formation of a condensate provides the ability to sustain particle currents at a constant velocity for long periods of time without any driving force; a phenomenon denoted as superfluidity.

A major recent breakthrough is the realization of Bose-Einstein condensation in weakly interacting alkali gases [4, 5]. This success was preceded by the development of advanced cooling techniques for neutral bosonic atoms, such as laser cooling and evaporative cooling, allowing to reach temperatures in the nK range. The neutral bosonic atomic gases are trapped by magnetic or optical dipole traps providing a harmonic potential and allowing for evaporative cooling. This confinement has important consequences on the transition temperature: For a noninteracting system, the critical temperature for Bose-Einstein condensation is determined by the constraint of a fixed particle number

$$N = \sum_k \frac{1}{\exp[\epsilon(k)/k_{\mathrm{B}} T_{\mathrm{BE}}] - 1} \tag{1.2}$$

with $\epsilon(k)$ the dispersion relation. In the thermodynamic limit, the dispersion relation is given by the kinetic energy of free particles $\epsilon(k) = \hbar^2 k^2/2m$ providing the transition temperature $T_{\mathrm{BE}} = 3.3\hbar^2 n^{2/3}/m$ [54]. The finite size of the trap transforms this phase transitions into a smooth crossover. Below the transition temperature T_{BE} the zero energy state is macroscopically occupied, defining the formation of a Bose-Einstein condensate in finite systems. As the typical particle number used in experiments is large, i.e., $N \sim 10^6$, this crossover shows a very sharp behavior with a well defined transition temperature for the onset of Bose-Einstein condensation. The trapping potential modifies the dispersion relation and for a harmonic trapping potential we obtain the energy levels of a harmonic oscillator $\epsilon(n) = \hbar[\omega_x n_x + \omega_y n_y + \omega_z n_z]$. The transition temperature becomes $T_{\mathrm{BE}} = 0.94\hbar(\omega_x\omega_y\omega_z\, N)^{1/3}$ [55].

The interactions in these alkali gases are weak and can be accounted for in the pseudo-potential approximation [56]. This contact interaction takes the form $V(x) = (4\pi\hbar^2 a_s/m)\delta(x)$ with a_s the s-wave scattering length; Feshbach resonances allow to tune the scattering length a_s in various alkali gases [57, 58, 59]. The ground state properties of the condensate are determined by the Gross-Pitaevskii equation; the analogue equation to the Ginzburg-Landau equation in superconductivity. The Gross-Pitaevskii equation determines the behavior of the condensate wave function ψ and derives from a microscopic theory. In turn, the excitation spectrum and the interaction-induced depletion of the condensate are successfully studied within the microscopic Bogoliubov theory, see Ref. [60, 56] for a review. The combination of these two theories has been extremely successful in explaining many fundamental properties of bulk Bose-Einstein condensates. The most prominent recent achievements are the detection of a superfluid flow around a moving object with the creation of defects above a critical velocity [61, 62, 63, 64] and the generation of a vortex lattice in a rotating Bose-Einstein condensate [65, 66, 67].

The high control of parameters pushes the study of atomic gases into the role of the ultimately tunable laboratory system for studying complex quantum phenomena and phase transitions. The main tool driving the bosonic gas into the regime of strong quantum fluctuations are the application of optical lattices

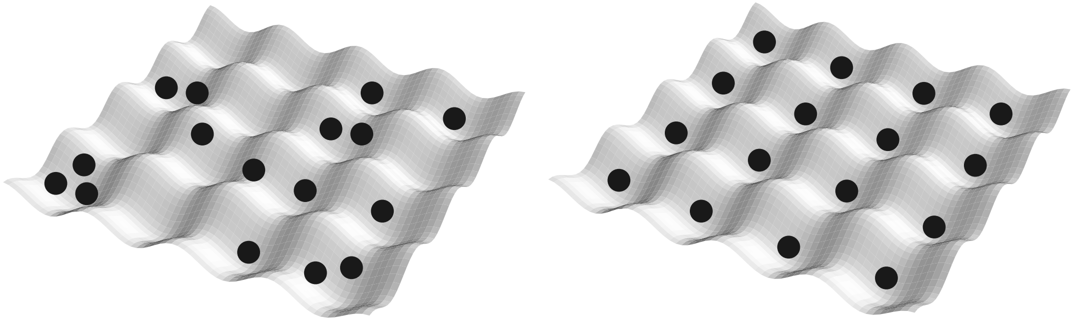

Figure 1.2: Comparison of the superfluid and the Mott insulating ground state. Left: A snap shot of the superfluid ground state at commensurate density. The particles travel coherently through the lattice and establish long range order. Right: Ground state of the Mott insulator. The atoms are pinned to the lattices site.

and geometric reduction to low dimensions. An optical lattice is obtained by a standing light wave generating a periodic lattice potential for the atomic gases via dipole interactions. Varying the strength of the optical lattice allows one to tune the kinetic energy (hopping energy J) relative to the interaction energy U. At a critical value $U/J|_{\text{S-MI}}$, the bosons undergo a quantum phase transition from a superfluid (large hopping J) to a Mott insulator (large interaction U) [47, 68]. Within the Mott insulating phase the system exhibits an excitation gap. This gap represents the analogue quantity to the excitation gap appearing in the superconductor to insulator transition discussed in the context of thin superconducting wires above. In a remarkable experiment, Greiner *et al.* have observed this quantum phase transition from a superfluid to a Mott insulator [69]. The transition appears via the competition between the condensation of the bosons into a matter wave characterized by a phase ϕ, and the granularity of the underlying particles preferring a fixed particle number n on each site, see Fig. 1.2. The reversible conversion of these two matter states has been recently demonstrated in Ref. [70].

The second tool allowing for the study of strong quantum fluctuations is dimensional reduction. This approach represents the standard method to increase fluctuations in quantum condensed matter, and was already discussed above in the context of superconducting devices. In homogeneous two-dimensional films, thermal fluctuations suppress true off-diagonal long-range order and a condensate may only survive at zero temperature. The quasi off-diagonal long-range order present below the Kosterlitz-Thouless transition temperature T_{KT} is sufficient to provide a superfluid stiffness [3]. However, the harmonic trapping potential of the traps used for atomic gases can stabilize the presence of a condensate even in two dimensions [60]. The focus then shifts to atomic gases in one-dimensional systems. Such one-dimensional bosons with a contact interaction have attracted a lot of interest as a toy model for an exactly solvable many-particle system [71, 72, 73]. The interaction strength is quantified by the dimensionless parameter $\gamma = mg/\hbar^2 n$, the ratio between the interaction and the kinetic energy (n denotes the 1D boson density and $g = 2\hbar\omega_\perp a_s$ the strength of the contact interaction with $\omega_\perp$the transverse trapping frequency). For weak interactions ($\gamma \ll 1$) the bosons condense into matter waves with quenched phase fluctuations. In contrast, for increasing interactions ($\gamma \gg 1$) the granular nature of the bosons starts to play an important role and finally culminates in the Bose-Fermi crossover in the limit $\gamma \rightarrow \infty$. In this so-called Tonks gas, the hard-core bosons behave as non-interacting fermions [71]. The recent theoretical advances provide a deeper understanding of the Bose-Fermi crossover in atomic gases and involve the study of phase fluctuations [74], interactions and scattering lengths [75], modifications of the density profiles [76], and the breakdown of mean-field theory [77, 78, 79, 80]. On the experimental side, three different approaches confine atomic gases into one dimension: highly anisotropic traps [81], trapping of atoms on a microelectronic chip [82, 83, 84], and transverse confinement by a strong 2D optical lattice [85]. Currently, the experimental setup with a 2D optical lattice producing a strong transverse confining is the most promising candidate to achieve a one dimensional atomic gas in the Tonks gas limit. The exploration of bosonic condensates in this extreme quantum regime remains an intriguing task for future studies. In this dissertation, we present the detailed study of the superfluid response of bosons confined in one dimension in Chapter 3. Combining the two main tools for driving bosonic gases into the regime of strong quantum effects, optical lattices and dimensional reduction, provides new insights into the superfluid to Mott insulator transition which are presented in Chapter 4.

Finally, the recent progress in sympathetic cooling allows to reach quantum degeneracy of fermionic atomic gases as well [86, 87, 88, 89]. These atomic mixtures of bosons and fermions allow for the realization and study of new thermodynamic phase transitions with an interesting synergy appearing between the fields of quantum optics and condensed matter physics. Phenomena studied so far are phase separation between the fermions and the bosons [90, 91] and the collapse of a degenerate Fermi gas [92]. Recent trends are the striving for the realization of a BCS-type condensate in a fermionic system [93, 94, 95], and the idea for the realization of system-modelling via an artificial quantum system. We investigate in Chapter 5 the appearance of a supersolid phase in such Bose-Fermi mixture. Such a supersolid combines the main characteristics of superfluids, the presence of a condensate and superfluid stiffness, with the crystalline order usually present in solids.

In conclusion, quantum condensed matter represents systems where quantum effects operate on a truly macroscopic level and a large number of particles condense into the same quantum state establishing a matter wave. Pushing these condensates to extreme conditions increases quantum effects, and the competition between the granularity of the underlying particles and the condensation into a matter wave entails fascinating phase transitions. In this thesis we study such phase transitions in quantum condensed matter.

The outline of this thesis is as follows: In Chapter 2, we study thin superconducting wires of finite length and focus on the destruction of superconductivity by quantum nucleation of phase slips. We derive the complete phase diagram taking into account the coupling of the wire to the environment. The renormalization of the mean-field critical temperature T_{c0} by disorder is included in our low energy action via an effective admittance μ. In analogy to the destruction of superconductivity in superconductors, we study the influence of quantum fluctuations on the superfluid response of atomic gases confined to one dimension in Chapter 3. Here, the absence of an environment inducing dissipation strongly modifies the analysis as compared to the superconducting situation. Introducing a moving object within the atomic gas allows to probe the superfluid response. In turn, this perturbation itself acts as nucleation point for quantum phase slips. We analyze the superfluid response for two finite geometries: a ring and a tube. In Chapter 4, we combine the two main tools driving atomic gases into the regime of strong quantum fluctuations: confined geometries and optical lattices. We find that the superfluid to Mott insulator transition can be driven via tuning of two different parameters: the Mott insulator is reached by increasing the strength of the optical lattice or by increasing the confinement of the bosons. Finally, in the last Chapter 5, we focus on Bose-Fermi mixtures in two dimensions and subjected to an optical lattice. Such a setup allows to drive the system into a supersolid phase. We study the phase diagram in the weak coupling limit, where the supersolid instability competes with an instability towards phase separation.

Chapter 2

Quantum Fluctuations in Thin Superconducting Wires of Finite Length

2.1 Introduction

The presence of fluctuations and disorder strongly influences the superconducting transition temperature in reduced dimensions (films and wires). In *two-dimensional* films, disorder decreases the critical temperature, which eventually vanishes and gives way to a superconductor-insulator phase transition [43]. Starting from a microscopic description with attractive *fermions*, the disorder increases the effectiveness of the Coloumb interaction and provides a reduction of the mean-field transition temperature T_{c0} [44, 45, 46]. Below T_{c0} the formation of Cooper pairs takes place and the quantum and thermal fluctuations of the *bosonic* Cooper pairs further reduce the superconducting transition temperature T_c: the films undergo a Berezinkii-Kosterlitz-Thouless (BKT) transition. Again, disorder provides an additional reduction of the critical temperature via the suppression of the superfluid density entailing an increase of bosonic fluctuations [48]. The *fermionic* and the *bosonic* suppression of the critical temperature can drive the superconductor-insulator phase transition for a critical disorder strength and in general the interplay of both mechanisms of T_c-suppression is expected to be observed [49].

In *one-dimensional* superconducting wires the influence of thermal and quantum fluctuations of the *bosonic* Cooper pairs is further increased. In addition, the usually high normal resistance also indicates that a *fermionic* renormalization of the mean-field transition temperature T_{c0} plays an essential role [50]. This disorder-induced *fermionic* suppression of the mean-field critical temperature T_{c0} [51, 52] provides qualitative agreement with experiments on amorphous wires [36]. In turn, the *bosonic* fluctuations of Cooper pairs appearing below the mean-field transition at T_{c0} define a finite resistenace via nucleation of thermally activated phase slips [9, 12] and hence remove the finite temperature transition; superconductivity possibly survives only at zero temperature. The focus then is on the quantum nucleation of phase slips; their proliferation may trigger a zero temperature SI quantum phase transition [13, 34, 14, 35]. While first attempts to observe quantum phase slips [13] are still debated due to the granular structure of the wires [30, 36], recent experiments on amorphous ultra-thin wires [40, 41] carry the signatures of a SI transition in a homogeneous system. In this chapter, we analyze the bosonic Cooper pair fluctuations in realistic wires of finite length which are naturally coupled to their environment through their boundaries; we demonstrate how the SI transition is quenched in the finite system and reappears through its coupling to the environment.

Previous studies of quantum fluctuations focused on the zero temperature phase diagram of infinite wires [14] and found a zero temperature phase transition separating a superconducting and an insulating phase at $\mu_c = 2$; the dimensionless parameter μ characterizes the superconducting properties and strongly depends on the thickness of the wire. Note, that in the following we ignore an additional dissipative channel due to excited quasi-particles and call the non-superconducting state an insulating one. The dynamics of the phase slips strongly depends on the presence of the plasma mode with linear spectrum [32, 14]. Real experiments are carried out on wires of finite length; the wires used in experiments [40] have a typical length $L \sim 0.5 - 2\mu m$ providing a discrete spectrum of the plasma modes. The wire's coupling to the environment through appropriate boundary conditions imposes a drastic change in the phase slip dynamics and modifies the wire's low energy physics. Previous studies of finite systems involve a ring geometry, where the finite length is introduced via periodic boundary conditions [34, 35], a setup not realized in experimental situations. Here, a generic description of the experimental setup is obtained by embedding the wire in a voltage driven loop with impedances $Z_{\parallel}(\omega)$ and $Z_{\perp}(\omega)$ placed in parallel and in series, see Fig. 2.1 and Sec. 2.2. As, we are mainly interested in thermodynamic aspects, the most relevant contributions of the environment are the static parallel and serial resistances $R_{\|}$ and $R_{\perp}$. Furthermore, we concentrate on the current-driven limit with $V, R_{\|} \to \infty$, keeping $I = V/R_{\perp}$ fixed. The voltage driven case with $R_{\|} \to \infty$ and other mixed cases ($R_{\perp}$, $R_{\|} < \infty$) are easily derived from the current-driven solution via Kirchhoff's laws, see Sec. 2.2.

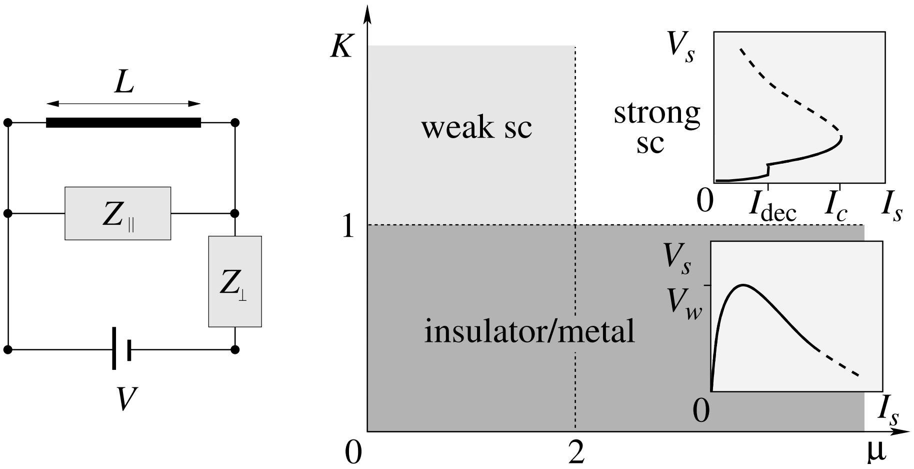

Figure 2.1: Left: Setup with the quantum wire embedded in a voltage driven loop with parallel ($Z_{\|}$) and serial ($Z_{\perp}$) impedances defining the environment. Right: Phase diagram with superconducting and insulating phases separated by a quantum phase transition at $K = 1$. The superconducting phase splits into weak and strong regimes separated by a crossover at $\mu \approx 2$, the leftover of the SI transition in the infinite wire. The insets show sketches of the wire's I_s-V_s characteristic at $T = 0$. In the superconductor ($K > 1$) the algebraic characteristic is dominated by the environment at small currents $I < I_{\text{dec}}$. A highly conducting shunt with $K \gg \mu$ allows to probe the wire above the deconfinement current I_{dec}; I_c denotes the depairing current of the wire. The insulator exhibits a Coulomb gab behavior below the critical voltage V_{W}.

The coupling to the environment changes the $T = 0$ phase diagram of the infinite system, see Fig. 2.1: The SI transition at $\mu = 2$ is turned into a crossover, while a new quantum phase transition appears at the critical value $K = R_Q/R_{\|} = 1$ of the shunt's conductance ($R_Q = \pi\hbar/2e^2$ denotes the quantum resistance). A highly conducting shunt with $K > 1$ relaxes the strain on the wire and produces a superconducting response with an algebraic I–V characteristic, while a low conductance $K < 1$ leads to the proliferation of phase slips and hence to an insulator. Then, in the insulating phase with $K < 1$ the relation between the current I_s flowing through the wire and voltage V_s across the wire exhibits a Coulomb gap, which is rounded by quantum fluctuations, see Fig. 2.1. In turn, in the superfluid phase we obtain a vanishing resistance at zero drive with algebraic corrections. The characteristic response of the superconducting wire can be probed with a high conductance environment $K \gg \mu$ at large drive above the current I_{dec} where confined phase-slip pairs are separated, see Fig. 2.1.

This chapter is organized as follows: In Sec. 2.2, we present an extended discussion of the difference between a current driven setup and a voltage biased setup. We show, that given a general quantum device coupled to a classical environment, the current-voltage characteristic in the different setups derive from each other; especially, we focus on the well-known current-voltage characteristic of a Josephson junction. Furthermore, we discuss an experimentally realizable device allowing for a perfect current bias. Sec. 2.3 describes the derivation of the action for the ultrathin superconducting wire coupled to the environment. The mathematical method for studying this action is presented in Sec. 2.4. The method applied here is the instanton expansion of the partition function, which maps the system to a gas of interacting charged particles; each particle corresponds to a vortex/antivortex. The study of the interaction between a vortex-antivortex pair allows for the derivation of the phase diagram via a renormalization group analysis and is presented in Sec. 2.5. We first focus on the infinite system and describe the modifications induced by the coupling to the environment in a second step. The response of the system to a current drive is studied in Sec. 2.6 for the superconducting and the insulating phase. Our results are summarized and discussed in Sec. 2.7.

2.2 Voltage-biased vs. current-biased circuits

Probing a quantum mechanical system requires its coupling to the environment which provides a source of decoherence for the quantum dynamics. This coupling modifies the ground state and the measurement depends on the internal parameters of the quantum system and the external parameters describing the measurement setup. Here, we focus on small quantum devices probed via measurement of the current-voltage (I-V) characteristic; examples of such quantum devices are small capacitance Josephson junctions [23, 19, 25], single electron tunnel junctions [96, 19], single-Cooper-pair tunnel junctions [26], and ultrathin superconducting wires (discussed in this chapter). The general setup is shown in Fig. 2.2 and consists of the quantum device, a voltage source driving the quantum device and a parallel and serial electric circuit. The external measurement setup discussed here is a classical and linear environment, implying that the parallel and the serial electric circuits are fully described by their impedances $Z_\parallel$, and $Z_\perp$. Note, that the parallel impedance in general includes internal classical elements of the quantum device such as internal resistances or capacitances, and external elements, e. g., an additional shunt resistance. In this section we discuss the interplay between different environments and derive a generic setup. This setup consists of a perfect current source driving the device and an impedance $Z_\parallel$ parallel to the quantum device. The current-voltage characteristics for a general setup then derives from the current-voltage characteristic for a current driven system. First, we focus on a Josephson junction coupled to an ohmic environment, and discuss the interrelation between a current biased setup and a voltage biased setup. The situation of a thin superconducting wire is discussed in the rest of this chapter.

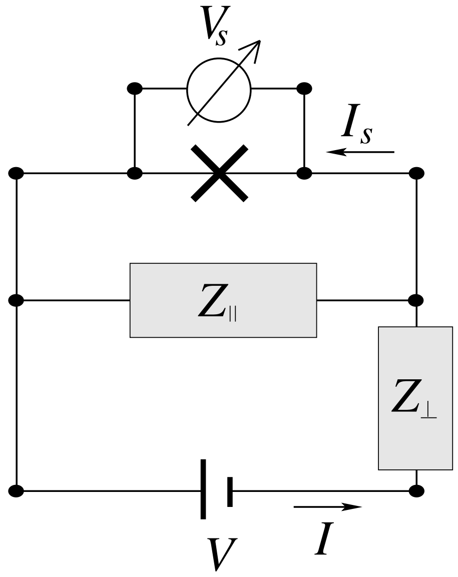

Figure 2.2: Generic setup of an environment: the quantum device (marked by a cross) is coupled to the environment with a parallel impedance $Z_\parallel$ and a serial impedance $Z_\perp$. In addition, a voltage source drives the setup with voltage V.

The relation between the current and voltage fluctuations at the contacts to the external environment influence the dynamics of the quantum device. In the following, we denote by $V_s(\omega)$ the voltage across the quantum device and by $I_s(\omega)$ the current flowing through the device. The current conservation provides the following constraint on these fluctuations

$$I_s(\omega) + \left[\frac{1}{Z_\parallel(\omega)} + \frac{1}{Z_\perp(\omega)}\right] V_s(\omega) = \frac{V}{Z_\perp(\omega)}. \tag{2.1}$$

The averaged voltage $V_s = \langle V_s(\omega)\rangle$ and current $I_s = \langle I_s(\omega)\rangle$ define the intrinsic current-voltage characteristic I_s-V_s of the quantum device. In addition, the quantum device and the environment can be charged with respect to each other and obey the charge conservation restriction

$$V_s^+ = Z^+(\omega) I_s^+(\omega) \tag{2.2}$$

with $V_s^+(\omega)$ the relative voltage between the quantum device and the environment, $I_s^+(\omega)$ the current charging the device, and $Z^+(\omega)$ the generalized relative capacitance. In the low frequency limit, the generalized capacitance $Z^+(\omega)$ vanishes as $Z^+(\omega) \propto \omega$ and this charge conservation relation affects the current-voltage characteristic only at high drives.

The above relations of current conservation (2.1) and charge conservation (2.2) fully determine the influence of the environment on the quantum device and play the role of boundary conditions for the internal quantum dynamics of the device. As a consequence, every environment producing the same boundary relations (2.1) and (2.2) produces the same intrinsic current-voltage characteristic I_s-V_s of the quantum device. The current-voltage characteristic $I - V$ of the full setup then derives from the relations

$$I = I_s + \frac{V_s}{Z_\parallel} \qquad\qquad V = \left(1 + \frac{Z_\perp}{Z_\parallel}\right) V_s + Z_\perp I_s \tag{2.3}$$

In order to simplify the following discussion, we assume that $Z^+(\omega)$ vanishes in the relevant low frequency regime; then the behavior of the system is determined by the current conservation (2.1) alone. Analyzing this relation, it follows that the right-hand side drives the system with the strength $F = V/Z_\perp$, while the voltage and current fluctuations are related via the total impedance of the electric circuit $Z_{\text{tot}} = [Z_\parallel^{-1} + Z_\perp^{-1}]^{-1}$; it is the total impedance Z_{tot} which determines the influence of the environment on the quantum device.

In the following, we discuss this behavior for the example of a Josephson junctions coupled to an ohmic environment, which has attracted a lot of interest over the past years [17, 23, 19, 97]. Such an ohmic environment naturally appears in the low frequency limit $Z_{\perp,\parallel} \to R_{\perp,\parallel}$ for $\omega \to 0$. The Josephson junction is characterized by the quantum variable φ, the phase difference across the junction. The Josephson relation and the Josephson coupling determine the voltage V_s across and the current I_s through the quantum device,

$$V_s(t) = \frac{\hbar}{2e}\partial_t\varphi(t), \qquad I_s(t) = \frac{2eE_J}{\hbar}\sin\left[\varphi(t)\right]. \tag{2.4}$$

It follows from the current conservation (2.1) that the intrinsic current voltage characteristic I_s–V_s only depends on the total resistance $R_{\text{tot}} = [R_\parallel^{-1} + R_\perp^{-1}]^{-1}$ which is conveniently expressed by the dimensionless parameter $K = R_Q/R_{\text{tot}}$ with the quantum resistance $R_Q = \pi\hbar/2e^2$. A current driven setup is obtained by a large serial resistance $R_\perp \to \infty$ with $I = V/R_\perp$ fixed; implying $K = R_Q/R_\parallel$. The action in imaginary time for the phase difference φ then maps to the action of a particle in a periodic potential with damping [98]

$$\frac{S}{\hbar} = \frac{K}{4\pi}\int\frac{d\omega}{2\pi}|\omega|\,|\varphi|^2 + \int d\tau\left[\frac{\hbar}{E_C}\left(\partial_\tau\varphi\right)^2 + \frac{E_J}{\hbar}\cos\left(\varphi\right) - \frac{I}{2e}\varphi\right]. \tag{2.5}$$

Here, E_C accounts for a parallel capacitance and provides a high frequency regularization of the theory. The intrinsic current voltage characteristic I_s–V_s derives from the response function $\langle\partial_t\varphi\rangle = X_I$,

$$\begin{aligned} V_s &= \frac{\hbar}{2e}\langle\partial_t\varphi\rangle = \frac{\hbar}{2e}X_I\left(K, \frac{\pi I}{e}\right), && (2.6)\\ I_s &= I - \frac{V_s}{R_\parallel}. && (2.7)\end{aligned}$$

Different approaches have been applied to determine the response function. For $K < 1$ perturbation theory in E_J converges [23, 97], while for $K > 1$ the instanton expansion converges and provides the response function [23, 99]. The exact response function derives from a mapping of the action (2.5) to the boundary sine Gordon model, see appendix D.

On the other hand, increasing the parallel resistance $R_\parallel \to \infty$ provides a voltage driven setup with $K = R_Q/R_\perp$. Then the voltage V drives the system and the measured response is the current I_s through the Josephson junction,

$$\begin{aligned} I_s &= \frac{2eE_J}{\hbar}\langle\sin(\varphi)\rangle = \frac{e}{\pi}X_V\left(K, \frac{2eV}{\hbar}\right), && (2.8)\\ V_s &= V - R_\perp I_s. && (2.9)\end{aligned}$$

Comparing both setups at equal K, the intrinsic current voltage characteristic I_s–V_s coincides as in both situations the boundary conditions are equivalent for drives satisfying the relation $V = R_Q I/K$. This implies a relation between the two response functions $X_I(K, \pi I/e)$ and $X_V(K, 2eV/\hbar)$

$$X_I(K, F) = \frac{F}{K} - \frac{1}{K} X_V(K, F/K). \tag{2.10}$$

Note, that this relation remains valid for an arbitrary quantum device; for a Josephson junction the knowledge of the exact response function for the current driven setup and the presence of the duality relation $X_I(K, F) = F/K - X_I(1/K, \alpha F)$ with α an appropriate K dependent factor (see appendix D) implies $X_V(K, F/K)/K = X_I(1/K, \alpha F)$.

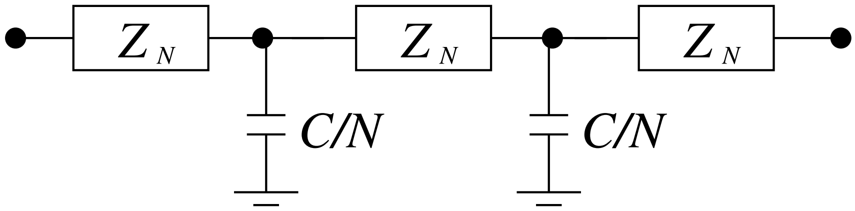

Figure 2.3: Model of the environment: Different sites are connected by a link with impedance $Z_N = (i\omega L + R)/N$. In addition, each site is capacitively coupled to the ground with capacitance C/N. C, L, R denote the total capacitance, inductance, and resistance of the device.

In an experiment, the control of the external impedances provides a fundamental problem. For example, current biasing a circuit requires that the serial impedance $Z_\perp(\omega)$ is large compared to the parallel shunt resistance $R_\parallel$ for all relevant frequencies, i.e., $Z_\perp(\omega) \gg R_\parallel$ for $\omega < 1/\kappa$ with κ the fundamental cut-off of the quantum device. An environment producing such a current biased setup is in general achieved by elements in the environment which are attached close to the quantum device and protect the quantum device from fluctuations of the measurement circuit. Using such a protecting of the quantum device, the observation of the Schmid transition in Josephson junctions was recently achieved [25]. Here, we discuss such an element in the environment which produces a protection of the quantum device and allows to control the external impedance. This element is modelled as a series of impedances $Z_N = i\omega\, L/N + R/N$ coupled to the ground via the capacitances C/N, see Fig. 2.3. Note, that C, L, and R represent the total capacitance, inductance and resistance of the device, while N accounts for the number of sites in the device ($N \to \infty$). Introducing the gauge potential ϕ_n on each site with $V_n = (\hbar/2e)\partial_t\phi_n$, the current $I_n = (V_{n+1} - V_n)/Z_N(\omega)$, and requiring current conservation, we obtain the equation

$$\frac{C\,\omega^2}{N}\phi_n = \frac{i\omega}{Z_N(\omega)}\left[\phi_{n+1} + \phi_{n-1} - 2\phi_n\right] \tag{2.11}$$

for the potential ϕ_n. The impedance of the device is then defined via $V_0 - V_N = Z(\omega)I_0$. Taking the limit $N \to \infty$ and solving for ϕ, we obtain

$$Z(\omega) = 2R\left(\frac{\omega_C}{\omega_L} + \frac{\omega_C}{i\,\omega}\right)^{1/2}\tanh\left[\frac{i\,\omega}{2\omega_C}\left(\frac{\omega_C}{\omega_L} + \frac{\omega_C}{i\,\omega}\right)^{1/2}\right] \tag{2.12}$$

with $\omega_C = 1/CR$ and $\omega_L = R/L$. For $R = 0$ the device exhibits sharp resonances, which become damped for a finite resistance R. For $\omega_C/\omega_L \ll 1$ these resonances disappear as the modes turn overdamped and the real part of the impedance smoothly interpolates between the two limiting values $Z(\omega \to 0) = R$ and $Z(\omega \to \infty) = 2(L/C)^{1/2}$ at the crossover frequency $(LC)^{-1/2}$, see Fig. 2.4.

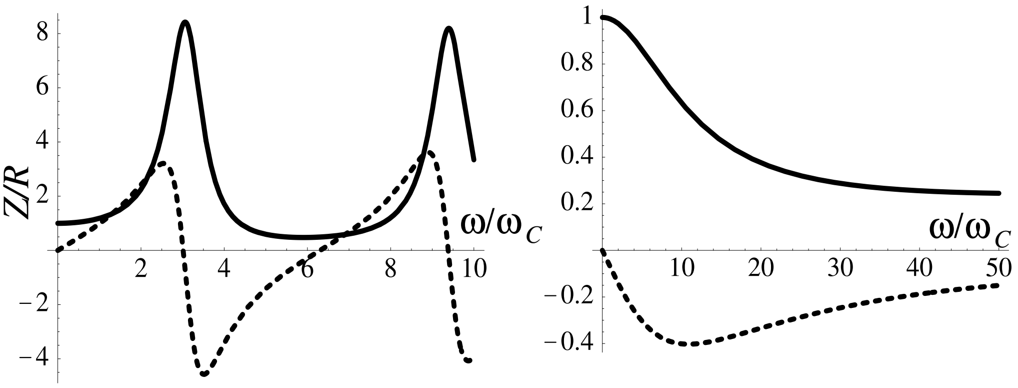

Figure 2.4: Left: The real (solid line) and imaginary (dashed line) part of the impedance Eq. 2.12 for $\omega_C/\omega_L = 1$. The impedance exhibits resonances which are damped due to the finite resistance R. Right: Impedance of the overdamped device with $\omega_C/\omega_L = 0.01$. The resonances have disappeared and the impedance interpolates smoothly between the limiting values $Z(\omega \to 0) = R$ and $Z(\omega \to \infty) = 2(L/C)^{1/2}$ at the crossover frequency $(LC)^{-1/2} = 10\omega_C$.

For a short thin film resistor with $R \approx 100\text{k}\Omega$ as used in Ref. [25], we expect a capacitance $C \sim l$ and $L = lm/e^2nS$ the kinetic inductance of the electrons, with $l \approx 1\mu$m the length of the device, $S \approx 1000\text{nm}^2$ its cross section and n the electronic density. Then, a high frequency impedance $2(L/C)^{1/2} \approx (4\pi\lambda_L^2/Sc^2) \sim 1/c$ is experimentally realistic. The impedance is in its overdamped limit with $\omega_C/\omega_L \ll 1$ and the crossover frequency becomes $(LC)^{-1/2} \sim 10^{14}$Hz. We conclude, that attaching the quantum system to current carrying leads via such a device provides a perfect current bias and control of the external impedances.

2.3 Superconducting wire coupled to the environment

In thin superconducting wires the Coulomb interaction produces a linear sound mode [32, 33] with sound velocity c_s. This is in contrast to bulk superconductors, where the Coulomb interaction shifts the frequency of collective density oscillations to the plasma frequency. We start the analysis of this sound mode with a discussion of thin superconducting wires with radius $r_0 = (S/\pi)^{1/2}$ smaller than the superconducting coherence length ξ and the London penetration length λ_L (S denotes the cross section of the wire). In the following, we focus on a system well below the mean field critical transition temperature T_{c0}; the effect of thermally excited quasi-particles is ignored. We introduce the electric and magnetic fields by the potentials V and A and describe the superconducting properties by the phase $\phi(x)$. Applying a mean-field description, the action in imaginary time of the superconducting wire of finite length L including the electromagnetic contributions of the surrounding media takes the form [31, 14]

$$\mathcal{S}_\text{S} = \int_0^{\hbar\beta} d\tau \int_{-L/2}^{L/2} dx \frac{1}{2}\left[C_w\Phi^2 + C_e V^2 + \frac{1}{L_e c^2}A^2 + \frac{m^2}{e^2 L_w}v_s^2\right]. \tag{2.13}$$

The terms $C_e V^2$ and $A^2(L_e c^2)^{-1}$ describe the electro- and magneto-static field energies in the environment of the wire, while the last term is the kinetic energy of the electrons with $v_s = (\hbar/2m)\left[\partial_x\phi - (2e/\hbar c)A\right]$, and the first term accounts for longitudinal screening with $\Phi = V - (\hbar/2e)\partial_\tau\phi$. The electromagnetic capacitance C_e and inductance L_e per unit length of the surrounding media and the kinetic capacitance C_w and inductance L_w of the superconducting wire are summarized below,

$$\begin{aligned}
C_w &= Se^2 N_0 &&\approx 3c^2 S/4\pi v_F^2 \lambda_L^2,\\
L_w &= \frac{m}{e^2 n_s S} &&\approx 4\pi\lambda_L^2/c^2 S,\\
C_e &= \frac{\epsilon}{\ln(d^2/S)} &&\approx \epsilon,\\
L_e &= \frac{\ln(d^2/S)}{c^2} &&\approx c^{-2}.
\end{aligned}$$

Here, n_s is the superconducting density, while N_0 denotes the density of states per spin, and ϵ is the dielectric constant of the surrounding medium placed a distance d away. Note, that for $d \gg \xi$ the capacity C_e becomes dispersive $C_e \sim [\ln 1/(kr_0)]^{-1}$ with k the wave vector of the mode. Integrating out the electromagnetic fields V and A, the low frequency action in imaginary time τ describing the *bosonic* fluctuations of the Cooper pairs in the superconducting wire takes the form [34, 14, 35]

$$\mathcal{S}_{\mathrm{S}} = \frac{\hbar\,\mu}{\pi c_s}\int_0^{\hbar\beta} d\tau \int_{-L/2}^{L/2} dx \frac{1}{2}\left[\,(\partial_\tau\phi)^2 + c_s^2\,(\partial_x\phi)^2\right], \tag{2.14}$$

with the first term accounting for the finite compression energy and the second term for the kinetic energy of the currents. In addition, we assume a high energy cut-off $\hbar/\kappa$ limiting the validity of the action (2.14). The sound velocity c_s and the dimensionless admittance μ of the wire become

$$c_s^2 = \frac{C_w^{-1} + C_e^{-1}}{L_w + L_e} \qquad \mu = \frac{\pi\,\hbar}{4e^2\, c_s(L_w + L_e)}\,,$$

while the electromagnetic fields are determined by the relations

$$V = \frac{1}{1 + C_e/C_w}\frac{\hbar}{2e}\partial_\tau\phi, \qquad A = \frac{c}{1 + L_w/L_e}\frac{\hbar}{2e}\partial_x\phi. \tag{2.15}$$

For generic parameters, we find $L_w \gg L_e$, i.e., the vector potential satisfies $A = 0$ and drops out, while $C_e < C_w$. Then, the dimensionless admittance μ and the sound velocity c_s are simply related to the 1D superfluid density $\rho_s = n_s S/2m^*$, and the Coulomb interaction between the Cooper pairs C_e, mediated via the surrounding media [14, 32]

$$\frac{\hbar\mu c_s}{2\pi} = \frac{\hbar^2\rho_s}{2}, \qquad \frac{\hbar\mu}{2\pi c_s} = \left(\frac{\hbar}{2e}\right)^2\frac{C_e}{2}. \tag{2.16}$$

Here, m^* denotes the mass of the Cooper pairs with n_s the electron density. Using the standard relations above, we can cast these expressions into the more simple form

$$\mu = \frac{\pi}{8}\sqrt{C_e}\,\alpha^{-1}\frac{r_0}{\lambda_L}, \qquad c_s = \frac{c}{2\sqrt{C_e}}\frac{r_0}{\lambda_L} \tag{2.17}$$

with $r_0 = \sqrt{S/\pi}$ the radius of the wire, λ_L the London penetration length ($\lambda_L^{-2} = 4\pi n_s e^2/mc^2$), and $\alpha = e^2/\hbar c$ the fine structure constant. Here, c_s is the plasmon velocity of the Mooij-Schön mode [32]. Going beyond the mean-field level, both fermionic [51, 52] and bosonic [72, 100] high energy fluctuations will renormalize the couplings μ and c_s in going to the low energy sector. Indeed, the high normal resistance of 1D superconducting wires indicates that the fermionic renormalization of T_{c0} plays an important role [50]; its disorder-induced suppression [51, 52] is in qualitative agreement with experiments on amorphous wires [36]. Here, we concentrate on the behavior below T_{c0} and assume such high frequency renormalization effects to be included in our choice of the effective phenomenological parameters μ and c_s.

Next, we consider the coupling between the superconducting wire and the environment. As discussed in Sec. 2.2, we are interested in the thermodynamic properties of the system and focus an a current driven setup with a parallel resistance $Z_\parallel = R$. The coupling between the superconducting wire and the environment involves the boundary fields $\phi_\pm(\tau) \equiv \phi_\pm(x,\tau)|_{x=L/2}$ where $\phi_\pm(x,\tau) = \phi(x,\tau) \pm \phi(-x,\tau)$: fluctuations in the phase difference ϕ_- generate a voltage across the wire inducing currents in the parallel shunts, while fluctuations in ϕ_+ account for charge accumulation. The action of the environment then becomes $\mathcal{S}_{\rm E} = \mathcal{S}_{\rm I} + \mathcal{S}_{\rm R}$, with

$$\mathcal{S}_{\rm I} = \int_0^{\hbar\beta} d\tau \frac{\hbar I}{2e}\phi_-, \tag{2.18}$$

$$\mathcal{S}_{\rm R} = \frac{\hbar K}{2\pi}\int \frac{d\omega}{4\pi}|\omega|\,|\phi_-(\omega)|^2 . \tag{2.19}$$

The first term describes an ideal current source driving the system with the current I, while the second term is the action of a parallel resistor with resistance R accounting for dissipation. Here, we have introduced the dimensionless conductance $K = R_Q/R$ of the shunt, with $R_Q = \pi\hbar/2e^2$ the quantum resistance. At finite temperature, the integral $\int d\omega/2\pi$ is replaced by a summation over Matsubara frequencies. Note, that the above environment does not account for an intrinsic dissipation in the superconducting wire, e.g., induced by quasi-particles.

Such an intrinsic dissipation is relevant in determining the parameters μ, c_s, and λ (the vortex fugacity, see below) [14]. The total low energy action of the system then combines the contributions of the superconducting wire and the environment,

$$\mathcal{S} = \mathcal{S}_{\mathrm{S}} + \mathcal{S}_{\mathrm{E}}, \tag{2.20}$$

with the high energy cut-off $\hbar/\kappa$. This cut-off derives from a microscopic analysis and is determined by the energy scales where additional terms in the action (2.20) become relevant. E.g., an upper bound for the validity of linear sound excitations within the superconducting wire is provided by the quasi-particle excitation energy Δ, i.e., $\hbar/\kappa < \Delta$.

2.4 Instanton Expansion

In 1D, the *bosonic* quantum fluctuations of the Cooper pairs are strongly increased. The statistical mechanics of the system 'superconducting wire plus environment' is determined by the partition function

$$\mathcal{Z} = \int D[\phi] \exp\left[-\mathcal{S}(\phi)/\hbar\right]. \tag{2.21}$$

Its main contributions arise from the combination of Gaussian and topological fluctuations, so called phase slips or instantons. Gaussian fluctuations destroy superconducting long-range order in the infinite system even at $T = 0$ as expressed by the logarithmically diverging phase correlator

$$\langle [\phi(x,\tau) - \phi(0,0)]^2 \rangle = \frac{1}{2\mu} \ln\left[\frac{c_s^2\tau^2 + x^2}{\tau^2}\right], \tag{2.22}$$

and only quasi off-diagonal long range order survives. This quasi long range order is sufficient to allow for a finite phase stiffness, i.e., a superconducting response. The latter then is destroyed by the proliferation of phase slips, the process we are going to analyze in more detail now.

The quantum phase slips are vortex like solutions in the x, τ-plane with finite winding around a core region of size $x_c < c_s\kappa$ and $\tau_c < \kappa$, where the superconducting gap $\Delta(x,\tau)$ drops to zero. Each vortex is characterized by its space-time position (x_i, τ_i) and winding number $\nu_i = \pm 1$. Outside this core region they are extrema of the action $\mathcal{S}$. Inside the superconducting wire, the action $\mathcal{S}_{\mathrm{S}}$ provides the equation

$$\left[c_s^2 \partial_x^2 + \partial_\tau^2\right] \phi\,(x,\tau) \;=\; 0. \tag{2.23}$$

The coupling to the environment described by the action $\mathcal{S}_E$ enforces the boundary conditions

$$K|\omega|\phi_- + \mu c_s[\partial_x\phi]_- = \frac{\pi I}{e}, \qquad [\partial_x\phi]_+ = 0, \tag{2.24}$$

at the superconductor–normal-metal interface. For simplification, we introduce the notation $[\partial_x\phi]_\pm(\tau) \equiv \partial_x\phi_\pm(x,\tau)|_{x=L/2}$. The first equation in (2.24) describes the current conservation as given by Kirchhoff's law with the supercurrent I_s and the dissipative current V_s/R in the shunt adding up to the total external current I, while the second equation accounts for charge neutrality; see the discussion in Sec. 2.2. Here, the supercurrent I_s and the voltage V_s across the wire takes the form

$$I_s = \frac{e\mu c_s}{\pi}\left[\partial_x\phi\right]_-, \qquad V_s = \frac{\hbar}{2e}|\omega|\phi_-. \tag{2.25}$$

Coming back to the partition function (2.21), the instanton expansion expresses the partition function as a series of contributions $\mathcal{Z}_n$ accounting for n vortex-antivortex–pairs. Note, that vortex solutions violating the winding number conservation $\sum_i \nu_i = 0$ contribute with zero weight and drop out. Furthermore, the partition function factorizes into Gaussian and topological parts, $\mathcal{Z} = \mathcal{Z}_{\mathrm{G}}\mathcal{Z}_{\mathrm{top}}$. Therefore, the contributions in $\mathcal{Z}_{\mathrm{G}}$ can not drive a quantum phase transition, as they only reduce the long-range order to quasi long-range order, and are neglected in the following study of the phase diagram. The action of an instanton solution with n vortex-antivortex–pairs splits into terms with pairwise interacting vortices

$$\mathcal{S}_n = \sum_{i\neq j} \nu_i G\left(x_i, \tau_i, x_j, \tau_j\right)\nu_j, \tag{2.26}$$

with $G\left(x_i, \tau_i, x_j, \tau_j\right) = \mathcal{S}_2/\hbar$ the action of a vortex-antivortex–pair. Then, the partition function $\mathcal{Z}_{\mathrm{top}}$ can be expanded in a series

$$\mathcal{Z}_{\mathrm{top}} = \sum_{n=0}^{\infty}\left(\frac{\lambda^n}{n!}\right)^2 \mathcal{Z}_n(G) \tag{2.27}$$

with

$$\mathcal{Z}_n = \int \frac{\prod_m^{2n} d\tau_m dx_m}{\left(c_s\kappa^2\right)^{2n}} \exp\left[\sum_{i\neq j} \nu_i G\left(x_i, \tau_i, x_j, \tau_j\right)\nu_j\right]. \tag{2.28}$$

This representation of the partition function is known as the instanton expansion and describes a classical gas of charged particles in two-dimensions with interaction G and charge neutrality $\sum_i \nu_i = 0$. The system is confined within the region

$|x| < L/2$ and $|\tau| < \hbar\beta/2$. The interaction G is determined by the action of the instanton solution for a vortex-antivortex–pair and depends strongly on the boundary conditions. In addition, each vortex-antivortex pair is weighted with the fugacity λ^2 accounting for the microscopic structure of the cores. Detailed mean-field estimates performed by Zaikin *et al.* [101] provide

$$\lambda = B \exp\left(-A\frac{R_Q}{R_\xi}\right) \tag{2.29}$$

with A a factor of order unity, $R_\xi = R_n\xi/L$ the normal resistance of the wire in a section of length ξ, and the preexponential factor $B \approx R_Q/R_\xi$. Here, R_n is the total resistance of the wire, ξ the superconducting coherence length, and L the length of the wire.

The validity of the instanton expansion (2.27) for the description of the ground state properties of the superconducting wire requires the assumption of a well defined mean-field superconducting ground state around which phase slips/instantons can be treated perturbatively. The condition of a well defined mean-field superconducting ground state is required for the derivation of the effective action (2.14), and a criterion for this condition is provided by the fermionic shift in the mean-field critical temperature. This reduction of the mean-field critical temperature due to the enhanced Coulomb repulsion in dirty wires can be written as [51, 50, 52]

$$T_{c0} \approx T_{c0}^{\mathrm{clean}} \exp\left[-b\frac{R_\xi}{4R_Q}\right] \tag{2.30}$$

with b again a factor of order unity, and T_{c0}^{clean} the mean-field critical temperature in absence of disorder. This result is valid for weak disorder with $R_\xi/R_Q \ll 1$ and describes a small shift in the critical temperature. It follows that for $R_\xi \ll R_Q$, the effective action (2.14) represents a good starting point, while for $R_\xi > R_Q$, the assumption of a well defined mean-field superconducting ground state becomes questionable. In addition to this *fermionic* breakdown, there is also a *bosonic* breakdown: topological quantum fluctuations (phase slips) are treated as a small perturbation around the superconducting ground state. This assumption is justified for small vortex fugacity $\lambda \ll 1$. Then, the vortices form a dilute gas in space x and imaginary time τ. Using the above estimate (2.29) for the vortex fugacity λ, shows that this condition is violated in the dirty limit with $R_\xi > R_Q$. In conclusion, we find that the *fermionic* breakdown (a mean-field superfluid ground state) and the *bosonic* breakdown (perturbative treatment of the phase slips) take place at roughly the same resistance $R_\xi = R_Q$. This is a strong indication, that both breakdowns have their origins in the same physical phenomenon. Nevertheless, we can not exclude that the two breakdowns are of different physical origin and up to date the behavior of the system in the crossover regime $R_\xi \approx R_Q$ has remained an open problem.

2.5 Zero temperature phase diagram

In the following, the ground state properties of the superconducting wire are analyzed within a real-space renormalization group approach of the instanton expansion (2.27). Within this approach, we integrate out vortex-antivortex–pairs on short scales in second order perturbation theory in the vortex fugacity λ. We find two different behaviors: (*i*) The vortex fugacity λ decreases on long time scales. Then, free vortices are quenched, the system exhibits quasi long range order, and the wire is superconducting. (*ii*) The vortex fugacity λ increases on large time scales and free vortices proliferate. Then, the phase correlator diverges linearly $\langle [\phi(\tau) - \phi(\tau')]^2 \rangle \sim |\tau - \tau'|$, and the system turns insulating.

2.5.1 Infinite system

The phase slip solution of Eq. (2.23) is well known for the infinite wire and takes the form

$$\phi(x, \tau) = \operatorname{Im} \ln \frac{x - x_1 + i c_s (\tau - \tau_1)}{x - x_2 + i c_s (\tau - \tau_2)}. \tag{2.31}$$

This solution is shown in Fig. 2.5; the solid lines represent the contours of fixed phase $\phi(x, \tau) = const$ and connect one vortex core with the anti-vortex core, i.e., the vortices screen each other. In turn, the dashed lines represent the current flow of the generalized current $\mathbf{j} = (\partial_x \phi, \partial_\tau \phi)$ in space x and imaginary time τ. Here, $j_x = \partial_x \phi$ accounts for the real current flowing in the 1D wire, while $j_\tau = \partial_\tau \phi$ describes charge accumulations within the wire and is proportional to an induced voltage. Current conservation demands, that the current lines are closed and encircle a vortex core with the winding number $\nu = \pm 1$; $\oint d\mathbf{l}\, \mathbf{j} = 2\pi\nu$. Inserting the solution (2.31) into the action (2.14) provides the dimensionless interaction G between vortex-antivortex pairs

$$G(\overline{x}, \overline{\tau}) = \mu \ln \frac{\overline{x}^2 / c_s^2 + \overline{\tau}^2}{\kappa^2}, \tag{2.32}$$

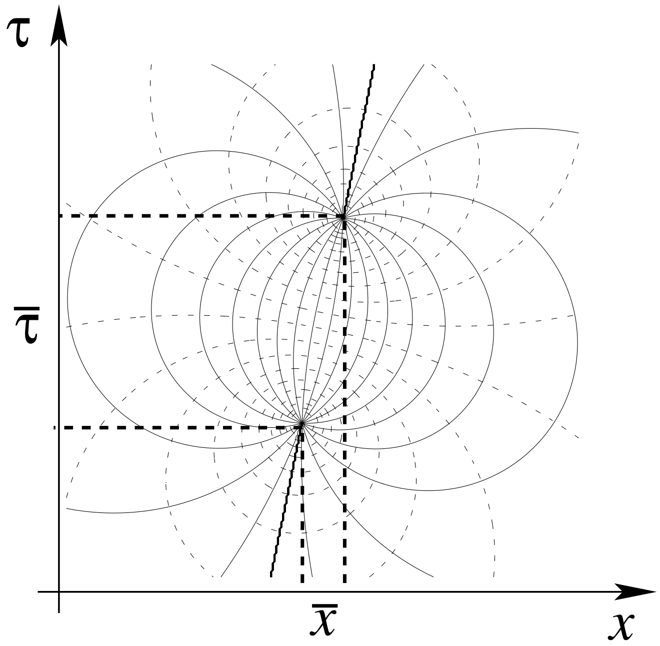

Figure 2.5: Phase slip solution $\phi(x, \tau)$ for a vortex-antivortex pair in the infinite system with vortex separation $\overline{\tau} = \tau_2 - \tau_1$ and $\overline{x} = x_2 - x_1$. The solid lines represent the contours of fixed phase $\phi(x, \tau) = \mathit{const}$ and connect one vortex core with the other vortex core, while the dashed lines represents the current flow of the generalized current $\mathbf{j} = (\partial_x \phi, \partial_\tau \phi)$ in space x and imaginary time τ.

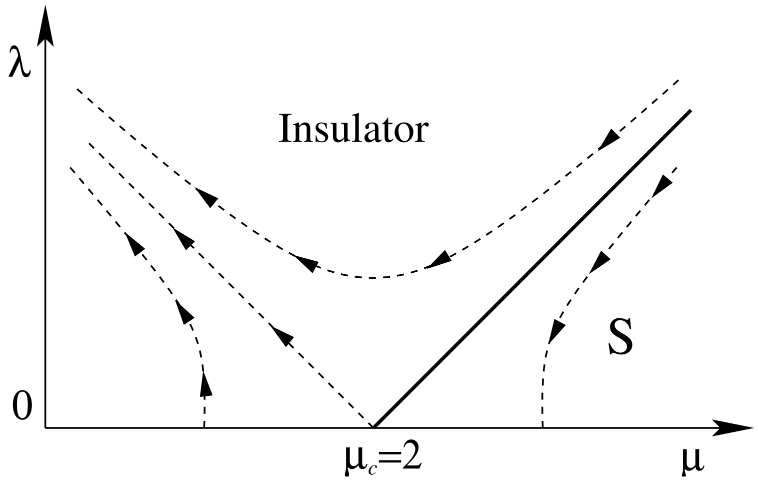

Figure 2.6: Kosterlitz-Thouless scaling flow: The solid line denotes the transition line separating the superconducting phase for $\mu > \mu_c = 2$ from the insulating phase for $\mu < \mu_c$. The line $(\mu, \lambda = 0)$ is a fix-point line, with stable fix-points for $\mu > \mu_c = 2$ and unstable fix-points for $\mu < \mu_c = 2$.

with $\overline{x} = x_1 - x_2$ and $\overline{\tau} = \tau_1 - \tau_2$. The interaction is logarithmic and corresponds to the interaction of charged particles in 2D.

Given this logarithmic interaction, the standard Kosterlitz–Thouless (KT) scaling analysis, where vortex-antivortex pairs are integrated out on the scale $\kappa < \overline{\tau}, \overline{x}/c_s \leq \kappa'$, provides the RG equation [7, 8]

$$\partial_l \mu = -4\pi^2 \mu^2 \lambda^2, \qquad \partial_l \lambda = (2 - \mu)\, \lambda, \tag{2.33}$$

with the scaling parameter $l = \ln \kappa/\kappa'$. The system undergoes a Berezinskii-Kosterlitz-Thouless (BKT) phase transition [7, 8, 102] at $\mu_c = 2$, see Fig. 2.6. For $\mu > \mu_c$, the vortex fugacity λ decreases under the renormalization group flow, implying that the number of free vortex-antivortex pairs is quenched and the wire is in the superconducting phase with quasi long-range order and a finite superfluid stiffness. In turn, for $\mu < \mu_c$ the vortex fugacity increases and there is a finite density $n_{\mathrm{V}} \sim \lambda^{1/(2-\mu)}/\kappa c_s$ of free vortices in the wire. In this strong coupling phase, the system exhibits a gap in the excitation spectrum. This gap can easily be understood in the following simplified picture: the free vortices destroy the phase coherence on the scale n_{V}^{-1} and the phase modes are quantized on this length scale providing the excitation energy $\hbar c_s/n_{\mathrm{V}}$. The opening of a gap in the strong coupling phase $\mu < \mu_c$ then pushes the wire into the insulating state. More quantitative ground state properties in this strong coupling phase can be derived from a mapping to the sine-Gordon model [103] (see Chapter 4 for a discussion of the sine-Gordon model).

2.5.2 Wires with finite length L

Next we focus on wires with finite length L. Then, the phase slips have to respect the boundary condition (2.24). Focusing on low frequencies, these boundary conditions reduce to

$$\mu c_s [\partial_x \phi]_- = I\pi/e. \tag{2.34}$$

The ansatz $\phi = \phi_{\mathrm{N}} + (\pi I x)/(2e\mu c_s)$ separates the transport current I from the current induced by the vortex-antivortex pair. Then, we have to solve (2.23) with the Neumann boundary conditions, $\partial_x \phi_{\mathrm{N}}(\pm L/2, \tau) = 0$, i.e., the currents induced by the phase slips cannot leave the superconducting wire, and charge accumulates at the boundaries and induces an voltage pulse. The solution $\phi_{\mathrm{N}}(x,\tau)$ easily derives from the $2L$-periodic solution ϕ_{P} using mirror vortices,

$$\phi_{\mathrm{N}}(x,\tau) = \phi_{\mathrm{P}}(x,\tau;2L) + \phi_{\mathrm{P}}(L-x,\tau;2L). \tag{2.35}$$

Here, the mirror vortices screen the vortices in the wire individually, see Fig. 2.7. In turn, the instanton solution with periodic boundary conditions $\phi(x,\tau)=\phi(x+2L,\tau)$ derives from the solution (2.31) in the infinite wire via the conformal transformation $w(z=x+i\tau)=\exp[2\pi i z/2L]$,

$$\phi_{\mathrm{P}}(x,\tau;2L)=\mathrm{Im}\ln\frac{\sin\frac{\pi}{2L}\left[(x-x_1)+ic_s(\tau-\tau_1)\right]}{\sin\frac{\pi}{2L}\left[(x-x_2)+ic_s(\tau-\tau_2)\right]}. \tag{2.36}$$

A plot of ϕ_{N} is shown in Fig. 2.8: the solid lines denote the contours of constant phase $\phi_{\mathrm{N}}(x,\tau)=\text{const.}$, while the dashed lines characterize the generalized currents $\mathbf{j}$ within the (x,τ) plane. At short distances between the vortex and the anti-vortex with $x_i\ll L$ and $\overline{\tau}\ll L/\pi c_s$, the solution reduces to the solution in the infinite system, and the vortices screen each other. With increasing distance $\overline{\tau}=|\tau_2-\tau_1|$ the mutual screening of the defect pair is replaced by the screening via image charges, cf. Fig. 2.8. Besides this bulk solution we need the boundary field $\phi_{\mathrm{N}-}(\tau)$ which derives directly from the solution $\phi_{\mathrm{N}}(x,\tau)$,

$$\phi_{\mathrm{N}-}(\tau)=\frac{\pi I L}{2e\mu c_s}+2\arctan\frac{\sinh\frac{\pi c_s}{L}(\tau-\tau_1)}{\cos\frac{\pi}{L}x_1}-2\arctan\frac{\sinh\frac{\pi c_s}{L}(\tau-\tau_2)}{\cos\frac{\pi}{L}x_2}, \tag{2.37}$$

and takes the form of a kink-antikink pair with width $\delta\tau_1\sim x_1/c_s$ and $\delta\tau_2\sim x_2/c_s$, respectively. Note, that this kink-antikink pair is a consequence of charge accumulation within the superconducting wire and induces via the relation $V_s=(\hbar/2e)|\omega|\phi_{\mathrm{N}-}$ a voltage pulse across the wire, see Eq. (2.25).

Inserting the solution ϕ_{N} into the action (2.14) provides us with the interaction G_{W} between the vortices arising within the superconducting wire. This interaction derives again from the interaction $G_{\mathrm{P}}(\overline{x},\overline{\tau},2L)$ between a vortex-antivortex pair with $2L$-periodic boundary conditions,

$$\begin{aligned}G_{\mathrm{W}}(x_1,x_2,\overline{\tau}) \;=\;& G_{\mathrm{P}}(\overline{x},\overline{\tau};2L)-G_{\mathrm{P}}(L-x_1-x_2,\overline{\tau};2L) \\ &+\frac{1}{2}\,G_{\mathrm{P}}(L-2x_1,0;2L)+\frac{1}{2}\,G_{\mathrm{P}}(L-2x_2,0;2L),\end{aligned} \tag{2.38}$$

and describes the pairwise interaction G_{P} between the vortex-antivortex pair with its mirror vortices. In turn, the action $G_{\mathrm{P}}(\overline{x},\overline{\tau},2L)$ for the instanton solution with $2L$-periodic boundary conditions derives from the solution (2.36) or again via conformal invariance from the action (2.32) in the infinite system,

$$G_{\mathrm{P}}(x,\tau;X)=\mu\ln\left[\left(\frac{X}{\pi c_s\kappa}\right)^2\left(\sinh^2\frac{\pi c_s\overline{\tau}}{X}+\sin^2\frac{\pi\overline{x}}{X}\right)\right]. \tag{2.39}$$

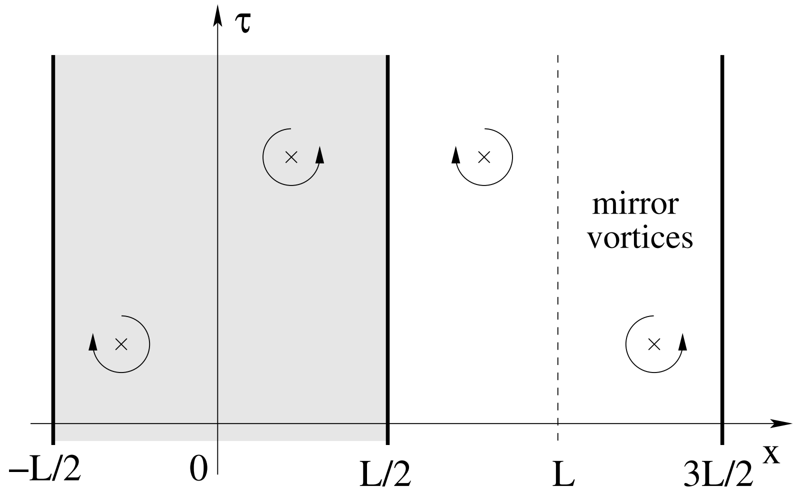

Figure 2.7: The solution of vortex-antivortex pair with Neumann boundary conditions $\partial\phi_\pm(\pm L/2,\tau)=0$ is obtained from the periodic solution via increasing the period by a factor 2 and adding two mirror vortices. The arrows indicate the vorticity of the vortices.

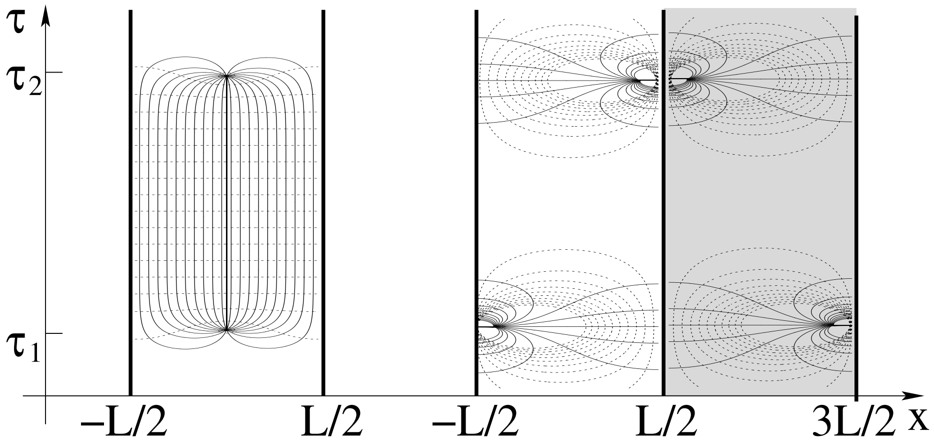

Figure 2.8: Phase slip solutions for periodic boundary conditions $\phi_{\rm P}$ (left) and Neumann boundary conditions $\phi_{\rm N}$ (right) at intervortex distance $L/\pi c_s < \overline{\tau} < \tau_{\rm B}$. Left: for $K \gg \mu$, defects are screened mutually, the 2π phase drop appears along the x-axis and drives a large current through the highly conducting shunt; the resulting string confines defect pairs. Right: with $\mu \gg K$, defects are screened individually by their mirror images, the 2π phase drop appears along the τ-axis and sets up displacement currents within the wire which cannot escape into the poorly conducting shunt, hence charge accumulates at the boundary resulting in a large voltage over the shunt; the defects are asymptotically free.

The interaction G_{W} at short distances between the vortices with $x_i \ll L$ and $\overline{\tau} \ll L/\pi c_s$ reduces to the logarithmic interaction characteristic of the infinite system, i.e., the vortex-antivortex pairs screen each other and the system does not dependent on the boundary conditions. At large vortex separations $\overline{\tau} > L/\pi c_s$ or vortices close to the boundary $|x_i| - L/2 < c_s\overline{\tau}$, the vortices are screened by their mirror images rather than mutually with a saturated G_{W} resulting in asymptotically free vortices. Furthermore, their action is minimized with $G_{\mathrm{W}} = 0$ for vortices within a thin boundary layer of width $\sim c_s\kappa$, i.e., $|x_i| - L/2 \leq c_s\kappa$. The weight of such boundary vortices then is determined by their interaction induced via the environment alone: Inserting the boundary field (2.37) into the action (2.19) we obtain the contribution

$$G_{\mathrm{E}}(x_1, x_2, \overline{\tau}) \approx K \ln \frac{\cos^2 \frac{\pi}{2L}(x_1 + x_2) + \left(\frac{\pi}{2L}\overline{\tau}\right)^2}{\cos \frac{\pi}{L}x_1 \, \cos \frac{\pi}{L}x_2} \tag{2.40}$$

which diverges logarithmically at long time scales, but with a weight determined by the dimensionless conductance K of the parallel shunt. In the end, the relevant contribution to the partition function arises from vortices nucleating at the boundary with an interaction $G \approx G_{\mathrm{E}} = K \ln(\overline{\tau}^2/\kappa^2)$ and the problem maps to a system of charged particles in one-dimension with logarithmic interaction and fugacity λ. The corresponding RG equations take the form [104]

$$\partial_l K = 0, \qquad \partial_l \lambda = (1 - K)\,\lambda. \tag{2.41}$$

In contrast to the infinite wire, the prefactor K of the logarithm is invariant under the RG flow and we obtain a quantum phase transition at $K = 1$ [23, 104], see Fig. 2.9. For $K > 1$, the vortex fugacity decreases and quenches the nucleation of vortices. Then, we obtain a superconducting phase with quasi long-range order and a finite superfluid stiffness. In turn, for $K < 1$ the vortices at the boundary proliferate and drive the system insulating.

The difference between the scaling equation (2.33) for the Kosterlitz-Thouless transition and the scaling equation (2.41) can easily been understood in the following simplified picture. The logarithmic interaction strength K (μ respectively) can be written as $K = q^2\eta$ with q the charge of the vortices and η the strength of the field mediating the interaction. Here, the charge is a topological quantity fixed at $q = 2\pi$ and thus remains unrenormalized. However, in the Kosterlitz-Thouless scaling equation, the creation of vortex-antivortex pairs polarizes the

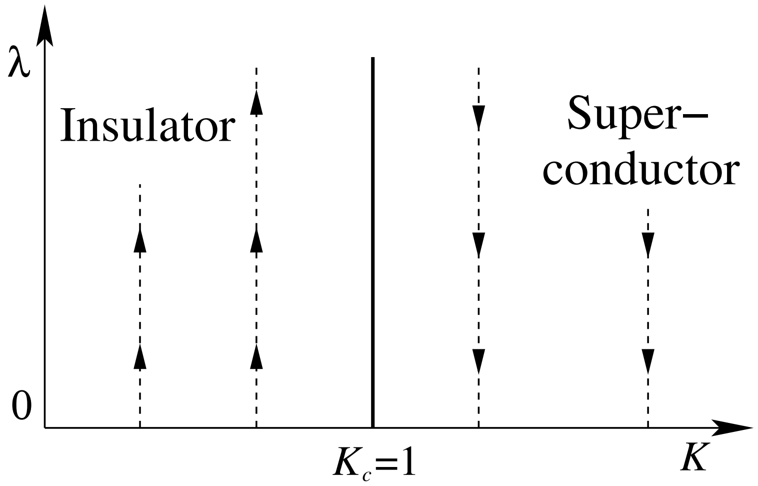

Figure 2.9: Renormalization group flow for a 1D gas of charged particles with logarithmic interaction of strength K and fugacity λ. The solid line denotes the transition line separating a superfluid phase for $K > 1$, where the fugacity decreases under the RG flow, from a insulating phase for $K < 1$, where the vortex fugacity increases. In contrast to the renormalization flow in the infinite system, K remains unrenormalized.

medium and screens the interaction: the strength η of the mediating field decreases. As a consequence, the strength μ of the logarithmic interaction becomes renormalized. In turn, for the Schmid transition, the interaction is mediated via a classical environment characterized by a classical strength η. Within this environment, quantum fluctuations are quenched and η is fixed. As a consequence, K is unrenormalized. For completeness, we also mention the Kondo model [105, 106]. In the Kondo model the interaction is mediated by a classical environment with a fixed η. However, the charge q is non-topological and is renormalized by quantum fluctuations. As a consequence, K is renormalized under the RG flow, thus providing the standard Kondo scaling flow [106].

In the analysis above we have determined the shape of the vortex-antivortex pair assuming Neumann boundary conditions, i.e., no currents can leave the wire, see Eq. (2.34). Inserting this approximate solution back into the action for the environment then has provided us with the interaction $G \approx G_{\mathrm{E}} = 2K \ln(\overline{\tau}/\kappa)$ between the defects. In order to check the consistency of this approximation we determine the correction $\delta\phi(x, \tau)$ due to the finite current $K|\omega|\phi_-$ flowing through the shunt (cf. 2.24) and insert the result back into the action S. The exact solution of the equations (2.23) and (2.24) is obtained with the ansatz

$$\begin{aligned} \phi_-(x,\tau) &= \phi_{\mathrm{N}-} + \delta\phi_- + (\pi I x)/(2e\mu c_s), & (2.42)\\ \phi_+(x,\tau) &= \phi_{\mathrm{N}+} & (2.43) \end{aligned}$$

The presence of vortices is captured by the term $\phi_{\mathrm{N}-}$, the solution of a vortex-antivortex pair with Neumann boundary conditions (2.35), leaving $\delta\phi_-$ as a solution of Eq. (2.23) without singularities. Its solution can be written as a function of the boundary field $\delta\phi_-(\omega)$ and takes the form

$$\delta\phi_-(x,\tau) = \delta\phi_-(\omega)\frac{\sinh\frac{x\omega}{c_s}}{\sinh\frac{L\omega}{2c_s}}. \tag{2.44}$$

Calculating the supercurrent $[\partial_x\delta\phi]_-(\tau) = \partial_x\delta\phi_-(x,\tau)|_{x=L/2}$ induced by this solution, provides a relation between the boundary values

$$\frac{\omega}{c_s}\delta\phi_-(\omega) = \tanh\frac{\omega L}{2c_s}[\partial_x\delta\phi]_-(\omega). \tag{2.45}$$

Inserting this relation back into (2.24) we obtain the correction

$$\delta\phi_- = -\frac{(K/\mu)\left|\tanh(\omega L/2c_s)\right|}{1+(K/\mu)\left|\tanh(\omega L/2c_s)\right|}\phi_{\mathrm{N}-}. \tag{2.46}$$

Finally, the correction $\delta\mathcal{S}$ to the action for Neumann boundary conditions is obtained by inserting the exact solution into (2.20) and takes the form

$$\frac{\delta\mathcal{S}}{\hbar} = -\frac{K}{4\pi}\int\frac{d\omega}{2\pi}\frac{|\omega|\left|\phi_{\mathrm{N}-}\right|^2}{1+(\mu/K)\left|\coth(\omega L/2c_s)\right|}. \tag{2.47}$$

Using the approximate solution for a kink-antikink pair $\phi_{\mathrm{N}-} \approx (4\pi/\omega)\sin(\omega\overline{\tau}/2)$ at distance $\overline{\tau}$, allows to estimate the correction $\delta\mathcal{S}$. The calculation of the integral (2.47) then shows that the correction remains small within the low frequency regime: for $\overline{\tau} > (1+K/\mu)L/\pi c_s$ we find a saturation

$$\delta\mathcal{S} \sim -[K/(1+\mu/K)]\ln[L(1+K/\mu)/\kappa c_s] \tag{2.48}$$

and this term is irrelevant in determining the low energy physics of the system. For a setup with $K \ll \mu$ the corrections remain small at higher frequencies with $\overline{\tau} < L/\pi c_s$,

$$\delta\mathcal{S} \approx -K\,(K/\mu)\ln\left(\overline{\tau}/\kappa\right). \tag{2.49}$$

This situation describes a poorly conducting shunt which refuses to pick up the large displacement currents in the wire, resulting in a voltage pulse and individually screened defects via mirror vortices, cf. Fig. 2.8.

However, in the opposite case with a highly conducting shunt protecting a 'poor' superconductor, $K \gg \mu$, the corrections turn out large: in the intermediate regime $L/\pi c_s < \overline{\tau} < \tau_{\mathrm{B}} \equiv KL/\pi\mu c_s$, we find

$$\delta S \approx -2K\ln(\overline{\tau}/\kappa) + 2\pi\mu c_s\overline{\tau}/L. \tag{2.50}$$

The first term then cancels the logarithmic interaction G_{E} induced by the environment, while the second term describes linearly confined vortex-antivortex pairs. It is then appropriate to change strategy: for $K \gg \mu$ the boundary condition (2.24) at high frequencies $\omega > 1/\tau_{\mathrm{B}}$ reduces to $\phi_- = 0$ and $[\partial_x\phi]_+ = 0$ for $I = 0$. Then, the phase field for the vortex-antivortex pair is given by the L-periodic solution ϕ_{P} with $\phi_{\mathrm{P}}(x,\tau) = \phi_{\mathrm{P}}(x+L,\tau)$, see (2.36). The interaction between the vortices is determined by

$$G_{\mathrm{P}}(x,\tau) = \mu\ln\left[\left(\frac{L}{\pi c_s\kappa}\right)^2\left(\sinh^2\frac{\pi c_s\overline{\tau}}{L} + \sin^2\frac{\pi\overline{x}}{L}\right)\right], \tag{2.51}$$

and indeed describes defect pairs linearly confined along the τ direction for distances $\overline{\tau} > L/\pi c_s$, cf. Fig. 2.8. Note that at smaller distances the defects interact logarithmically. At the same time, no voltage appears over the shunt resistor and the contribution from the environment vanishes, thus $G \approx G_{\mathrm{P}}$. In summary, the interaction for a highly conducting shunt with $K \gg \mu$ takes the form

$$G(\overline{x},\overline{\tau}) \approx \begin{cases} \mu\ln\left(\dfrac{\overline{\tau}^2 + \overline{x}^2/c_s^2}{\kappa^2}\right), & \overline{\tau}c_s, \overline{x} < L/\pi, \\[2ex] 2\pi\mu\dfrac{c_s\overline{\tau}}{L}, & L/\pi c_s < \overline{\tau} < \tau_{\mathrm{B}}, \\[2ex] K\ln\left(\dfrac{\overline{\tau}^2}{\kappa^2}\right), & \tau_{\mathrm{B}} < \tau. \end{cases} \tag{2.52}$$

Hence, the interaction between defects starts with a logarithmic behavior at small distances $\overline{\tau}c_s, \overline{x} < L/\pi$, proceeds with an intermediate regime of linear confinement, and terminates with the logarithmic low-frequency behavior determined by the environment for $\tau_{\mathrm{B}} < \tau$.

Given the three regimes of interaction above, the RG flow now involves three steps: Starting from high energies, we integrate over vortex-antivortex fluctuations with an interaction $G \approx G_{\mathrm{P}}$. The scaling for λ and μ follows from a similar calculation as presented by Kosterlitz [8] with small modifications accounting for the specific form of the interaction and the finite size of the system; the detailed calculation is presented in Appendix B. It follows that the renormalization group equations for μ and λ remain unchanged, see Eq. (2.33). The strength K is unaffected by the presence of vortex-antivortex fluctuations within the superconducting wire. The interaction then remains form invariant and the scaling equations for μ, λ, and K in the regime $\kappa < \tau < L/\pi c_s$ take the form

$$\partial_l \lambda = (2-\mu)\,\lambda, \qquad \partial_l \mu = -4\pi^2\mu^2\lambda^2, \qquad \partial_l K = 0, \tag{2.53}$$

providing us with the renormalized admittance $\mu(L/\pi c_s)$, the renormalized vortex fugacity $\lambda(L/\pi c_s)$, and an unrenormalized conductance K. The matching of the interaction is moved to the renormalized crossover scale $\tau_{\mathrm{B}} = KL/2\mu(L/\pi c_s)c_s$.

At the scale $L/\pi c_s$ the system turns one-dimensional. The interaction between vortex-antivortex pairs turns linear up to distances τ_{B}, implying that fluctuations of vortex-antivortex pairs are strongly suppressed. We relate the fugacities at scales $L/\pi c_s$ and τ_{B} via the activation energy necessary for creating a vortex-antivortex pair at distance τ_{B},

$$\lambda(\tau_{\mathrm{B}}) \sim \lambda(L/\pi c_s)\;\exp[-G_{\mathrm{P}}(\tau_{\mathrm{B}})] = \lambda(L/\pi c_s)\;\exp(-2K). \tag{2.54}$$

Finally, at even larger scales $\overline{\tau} > \tau_{\mathrm{B}}$, the interaction becomes again logarithmic with strength K and further scaling is defined by the RG equations (2.41), renormalizing further the vortex fugacity λ but leaving the conductance K invariant.

Hence, with the low-energy physics of the system entirely determined by the environment (i.e., by K), the renormalization process down to low energies still depends sensitively on the admittance ratio μ/K of the superconductor and the metallic shunt: for $K \ll \mu$ the interaction for the dominant phase slips is entirely determined by the environment characterized by its conductance K, while for $K \gg \mu$ the phase-slip pairs go through an intermediate regime of linear confinement involving the admittance μ of the superconducting wire; this difference impacts on the phase-slip fugacity and hence on the system's response at high drives, see below.

The overall phase diagram is sketched in Fig. 2.10: The quantum phase transition at $K = 1$ separates the superfluid phase for $K > 1$ from the insulating phase

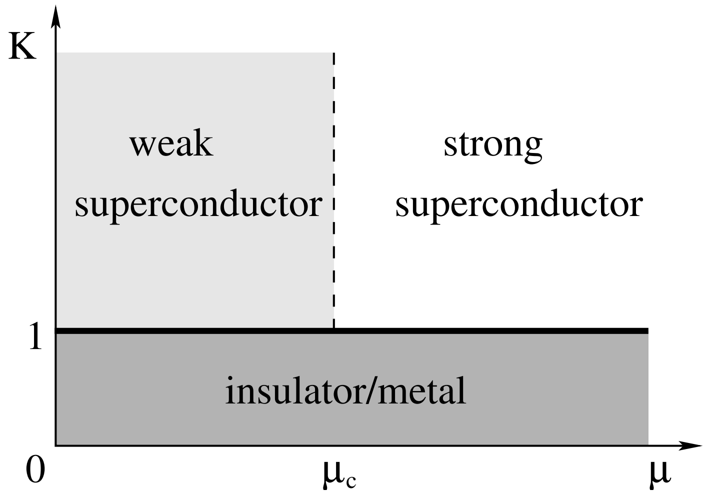

Figure 2.10: Phase diagram with superconducting and insulating phases separated by a quantum phase transition at $K = 1$. In addition we split the superconducting phase in a weak and a strong regime, separated by a smooth crossover at $\mu \approx 2$, the remainder of the SI quantum phase transition in the infinite wire.

at $K < 1$. In addition, we distinguish two different superconducting regimes at $K > 1$: for $\mu < \mu_c \approx 2$ the fugacity for the nucleation of small vortex-antivortex pairs separated by the distance $\overline{\tau} < L/\pi c_s$ is strongly increased as compared to the regime $\mu > \mu_c$. This crossover is the leftover from the SI quantum phase transition in the infinite wire and becomes significant at temperatures $T > \hbar c_s/L$ and high drives $\pi I/e > c_s/L$ where the corresponding small scales are probed.

An interesting solution is obtained for $K = \mu$ when the admittance of the superconducting wire matches up with the conductance of the parallel shunt: The centered (i.e., $x_i = 0$) solution (2.31) of the infinite wire satisfies the boundary conditions (2.24) and the interaction between centered vortex-pairs is determined by (2.32); corrections for $x_i \neq 0$ describe a repulsion away from the boundary. At short distances $\overline{x} < L$ and $\overline{\tau} < L/\pi c_s$ the interaction and the fugacity renormalize via the scaling equations (2.33); at large separation $\overline{\tau} > L/\pi c_s$ the scaling turns one-dimensional and is given by (2.41). While the interaction K remains unrenormalized, the flow of the fugacity λ signals a quantum phase transition at $K = 1$.

2.6 Current-Voltage characteristic

The interaction between vortex-antivortex pair always turns logarithmic on large scales $\overline{\tau} > \tau_{\mathrm{K}} \equiv \max(\kappa, \tau_{\mathrm{B}})$ with a prefactor $2K$ determined by the parallel shunt resistance. As a consequence, the low energy physics of the quantum wire reduces to that of a Josephson junction with a parallel shunt R; the partition function is equivalent to that of a particle in a periodic potential with damping $\eta = K/2\pi$ [23]. The current–voltage characteristics of resistively shunted Josephson junctions has been studied in great detail [23, 19]; in the following, we review the main results. The restricted validity of the logarithmic interaction with prefactor $2K$ limits this analysis to low temperatures $\hbar\beta > \tau_{\mathrm{K}}$ and low currents $I < eK/\tau_{\mathrm{K}}$. In addition, we derive the behavior of the current-voltage characteristic in the high frequency regime $\tau_{\mathrm{K}} < \overline{\tau} < \kappa$.

2.6.1 Superconducting phase

Within the superconducting phase $K > 1$, the current–voltage characteristic at low drives is calculated perturbatively in the vortex fugacity λ (here, $\lambda(\tau_{\mathrm{K}}) \to \lambda$ denotes the renormalized vortex fugacity at the scale τ_{K}),

$$V = \frac{\pi\hbar}{e}\left[\Gamma^{+}(I) - \Gamma^{-}(I)\right] \tag{2.55}$$

with $\Gamma^{\pm}$ the nucleation rate for vortex-antivortex pairs. The different signs correspond to different orientation of the vortex-antivortex pair along the τ-axes. The validity of Eq. (2.55) requires that the nucleation process is incoherent, i.e., the nucleation process is independent on the presence of other nucleated vortex-antivortex pairs. This assumption is well justified in the superconducting phase $K > 1$ [24]. The nucleation rates $\Gamma^{\pm}$ for the vortex-antivortex pairs take the form

$$\Gamma^{\pm} = \frac{\lambda^2}{\tau_{\mathrm{K}}^2}\int_{\tau_{\mathrm{K}}}^{\hbar\beta} d\overline{\tau}\exp\left[-K\ln\left(\frac{\hbar\beta}{\pi\tau_{\mathrm{K}}}\sin\frac{\pi\overline{\tau}}{\hbar\beta}\right)^2 \pm \frac{\pi}{e}I\,\overline{\tau}\right]. \tag{2.56}$$

The convergence of the $\overline{\tau}$-integral is obtained via the usual analytic continuation as described in Refs. [107, 108]; an explicit calculation is presented in Ref. [109]. Note, that the interaction $\sim K\ln\tau^2$ between a kink-antikink pair is modified to $\sim K\ln(\sin^2\pi\tau/\hbar\beta)$, respecting periodic boundary condition as required for imaginary time solutions at finite temperatures $T = 1/\beta$. The current–voltage characteristic takes the form

$$V = \frac{\pi\hbar\lambda^2}{e\tau_{\rm K}}\left(\frac{2\pi\tau_{\rm K}}{\hbar\beta}\right)^{2K-1}\sinh\left(\frac{\pi\hbar\beta I}{2e}\right)\frac{\left|\Gamma\left(K+i\hbar\beta I/2e\right)\right|^2}{\Gamma(2K)}. \tag{2.57}$$

The finite temperature introduces a energy scale T and comparing this scale to the driving force $\pi I/e$ provides us with two different characteristic regimes in the response,

$$V = \begin{cases} 2\pi^2\lambda^2 R_{\rm Q} I \dfrac{\Gamma(K)^2}{\Gamma(2K)}\left[\dfrac{2\pi T\tau_{\rm K}}{\hbar}\right]^{2K-2}, & \dfrac{I}{2Ke} \ll \dfrac{T}{\hbar}, \\ \dfrac{\hbar\pi^2\lambda^2}{e\tau_{\rm K}}\dfrac{1}{\Gamma(2K)}\left[\dfrac{\pi I\tau_{\rm K}}{e}\right]^{2K-1}, & \dfrac{T}{\hbar} \ll \dfrac{I}{2Ke}. \end{cases} \tag{2.58}$$

The algebraic characteristic with exponent $2K-1$ at zero temperature is turned into a linear response at finite temperatures and small drives, with an algebraic temperature dependence of the resistance. We conclude, that in one-dimensional wires superconductivity survives only at zero temperature and under the condition of a good protection by a high conductance shunt with $K > 1$; its signature is an algebraic response with an exponent $2K-1 > 1$.

For a highly resistive environment with $K \ll \mu$ this current voltage characteristic remains valid up to temperatures $T \approx \hbar/\kappa$ and currents $I \approx eK/\kappa$, as the dominant term arises via the nucleation of vortex-antivortex pairs at the boundary of the wire. Then the nonlinear current-voltage characteristic only probes, the environment instead of the superconducting wire.

In turn, for a high-conductance shunt $K \gg \mu$, the vortex-antivortex interaction is only logarithmic for intervortex separation $\overline{\tau} > \tau_{\rm B}$. In the following, we first focus on short intervortex separations with $\overline{\tau} < L/\pi c_s$, and treat the intermediate regime with $L/\pi c_s < \overline{\tau} < \tau_{\rm B}$ below. On short scales $\overline{\tau} < L/\pi c_s$ corresponding to high drives $I > I_{\rm dec} = 2e\mu c_s/L$ and temperatures $T > \hbar\pi c_s/L$, the interaction is modified to a logarithmic interaction with prefactor μ. In this regime, the finite size of the system plays a minor role and the decay rates are determined by the decay rates for the infinite system. Here, the finite temperature T introduces periodic boundary conditions in imaginary time τ with periodicity $\hbar\beta$. Then, the interaction derives from the action of the periodic solution (2.39) via replacing $\overline{x} \to c_s\overline{\tau}$, $\overline{\tau} \to \overline{x}/c_s$, and $X = c_s\hbar\beta$. The decay rates $\Gamma^{\pm}$ take the form

$$\Gamma^{\pm} = \frac{L\lambda^2}{\kappa^4 c_s^2}\int_{\tau_{\mathrm{K}}}^{\hbar\beta} d\overline{\tau}\int_{-\infty}^{\infty} dx \exp\left\{-\mu \ln\left[\left(\frac{\hbar\beta}{\pi\kappa}\right)^2\left(\sinh^2\frac{\pi c_s \overline{x}}{\hbar\beta} + \sin^2\frac{\pi\overline{\tau}}{\hbar\beta}\right)\right] \pm \frac{\pi}{e} I\,\overline{\tau}\right\}. \tag{2.59}$$

Note, that this exact interaction differs from the estimated interaction in Ref. [14] with only small corrections in the prefactor. The current-voltage characteristic becomes (see Appendix A)

$$V = \frac{2\pi\hbar y^2 L}{e\kappa^2 c_s}\left(\frac{2\pi\kappa}{\hbar\beta}\right)^{2\mu-2}\sinh\left(\frac{\hbar\beta I}{2e}\right)\frac{\left|\Gamma\left(\frac{\mu}{2} - i\frac{\hbar\beta I}{4e}\right)\right|^4}{\Gamma\left(\mu\right)^2}, \tag{2.60}$$

and reduces in the high temperature and low temperature limits to

$$V \sim \begin{cases} \lambda^2(\kappa) R_{\mathrm{Q}} I \dfrac{L}{c_s\kappa}\left[\dfrac{2\pi T\kappa}{\hbar}\right]^{2\mu-3}, & \dfrac{c_s}{L} < \dfrac{I}{2\mu e} \ll \dfrac{T}{\hbar}, \\ \dfrac{\hbar\lambda^2(\kappa)}{e\kappa}\dfrac{L}{c_s\kappa}\left[\dfrac{\pi I\kappa}{e\mu}\right]^{2\mu-2}, & \dfrac{\pi c_s}{L} < \dfrac{T}{\hbar} \ll \dfrac{I}{2\mu e}. \end{cases} \tag{2.61}$$

The current-voltage characteristic at low temperatures shows an algebraic behavior, but now the exponent is determined by the properties of the thin wire. We find that for a highly-conducting shunt with $\mu \ll K$, the current-voltage characteristic reveals the admittance μ of the thin wire in its algebraic behavior, either in the temperature dependence of the residual resistance at temperatures $T > \hbar\pi c_s/L$ or in the current dependence at high currents $I > I_{\mathrm{dec}}$.

In the intermediate regime with intervortex separations in the range $L/\pi c_s < \overline{\tau} < \tau_{\mathrm{B}}$ the interaction between the vortex-antivortex pair turns linear and describes confinement. This implies that for low currents $I \ll I_{\mathrm{dec}}$ the residual resistance decreases exponentially in the temperature range $\tau_{\mathrm{B}} > \hbar\beta > L/\pi c_s$, which is captured by the renormalization of the fugacity λ;

$$\frac{R(T)}{R(T = \hbar\pi c_s/L)} \sim \frac{\lambda(\hbar/T)}{\lambda(L/\pi c_s)} \approx \exp(-\mu\frac{\pi c_s\hbar}{TL}). \tag{2.62}$$

In turn, the behavior of the nonlinear I-V characteristic at low temperatures $T/\hbar \ll I/2\mu e$ is completely different. Then, the linear confinement of vortex-antivortex pairs provides the decoupling current $I_{\mathrm{dec}} = 2e\mu c_s/L$. First, we study the behavior at the decoupling current in the limit $K \to \infty$. Then, the interaction between a vortex-antivortex pair is determined by the periodic action (2.51) and

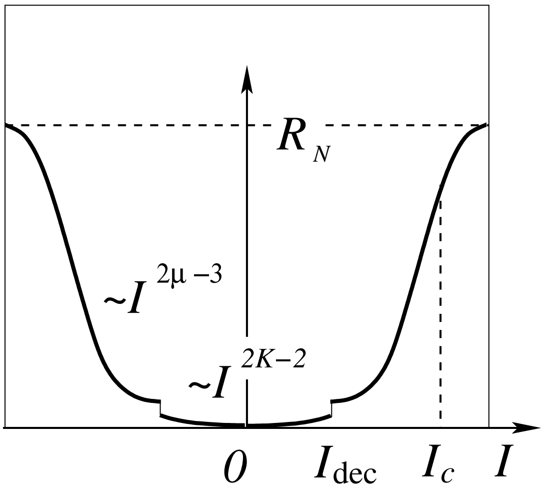

Figure 2.11: The current-voltage characteristic for the superconducting phase at $T = 0$. Below the depairing current I_c the formation of the Cooper pairs entails a sharp drop in the resistance (R_N denotes the total resistance of the system made from the normal wire and the parallel shunt R). The residual resistance at small drive is due to the quantum nucleation of phase slips. The algebraic current-voltage characteristic is dominated by the environment at small currents $I < I_{\text{dec}}$. A highly conducting shunt with $K \gg \mu$ allows to probe the quantum wire itself above the critical deconfinement current I_{dec}.

the quantum nucleation rate Γ^+ at zero temperature $T = 0$ is determined by the expression (Γ^- vanishes at zero temperature)

$$\Gamma^+ = \frac{L\lambda^2}{\kappa^4 c_s^2} \int d\bar{\tau} \int_{-L/2}^{L/2} dx \exp\left\{ -\mu \ln\left[\left(\frac{L}{\pi c_s \kappa}\right)^2 \left(\sinh^2 \frac{\pi c_s \bar{\tau}}{L} + \sin^2 \frac{\pi \bar{x}}{L} \right)\right] + \frac{\pi}{e} I\, \bar{\tau} \right\}. \tag{2.63}$$

It follows that at high currents $I > I_{\text{dex}}$ the nonlinear I-V characteristic takes the form $V \propto I^{2\mu-2}$ as discussed above, while approaching the decoupling current $I \to I_{\text{dec}}$ we obtain a finite voltage (see Appendix A)

$$V(I_{\text{dec}}) = \frac{\pi^2 \lambda^2 L}{\kappa^2 c_s} \left(\frac{2\pi c_s \kappa}{L}\right)^{2\mu-2}. \tag{2.64}$$

Below the decoupling current $I < I_{\text{dec}}$ it follows from Eq. 2.63, that the nucleation rates $\Gamma^\pm$ vanish identically as the linear confinement $\sim 2\pi\mu c_s \bar{\tau}/L$ exceeds the driving term $(\pi/e) I \bar{\tau}$. This shows that at the decoupling current I_{dec} a sharp step appears in the I-V characteristic. Adding a realistic environment with $K \gg \mu$

the nucleation rates for $I < I_{\text{dec}}$ are finite and provide an I-V characteristic given in Eq. (2.58). Nevertheless, the sharp step remains present as a consequence of the confinement.

A sketch of the I-V characteristic in the highly conducting regime $K \gg \mu$ is shown in Fig. 2.11. Below the depairing current I_c the formation of the Cooper pairs entails a sharp drop in the resistance. Here, R_N denotes the total resistance of the system made from the normal wire and the parallel shunt R. The residual resistance at small drive is due to the quantum nucleation of phase slips. The algebraic current-voltage characteristic is dominated by the environment at small currents $I < I_{\text{dec}}$. A highly conducting shunt with $K \gg \mu$ allows to probe the quantum wire itself above the critical deconfinement current I_{dec}

2.6.2 Insulating phase

The nucleation process of vortex-antivortex pairs in the superconducting phase describes the incoherent tunneling of the phase difference ϕ_- to the neighboring states $\phi_- \pm 2\pi$; this is in contrast to the insulating phase considered now. In the limit $K \to 0$ and $T = 0$, the same quantum nucleation accounts for coherent tunneling between neighboring states and leads to the formation of a Bloch band $\varepsilon(q)$ of width $W_0 = \hbar\lambda/\tau_{\text{K}}$, where q denotes the quasi-momentum associated with the boundary field ϕ_-. Applying a small driving current I, a voltage $2eV = \hbar\langle\dot{\phi}_-\rangle = \partial_q \varepsilon(q)$ is set up across the superconducting wire and all the current flows over the parallel shunt [19]. Then, the wire exhibits an insulating current-voltage characteristic, while the system combining the wire and its environment exhibits the linear response

$$V = RI. \tag{2.65}$$

This behavior remains valid for finite $K < 1$, but with a renormalized band width [19, 97, 25]

$$W \approx W_0 (W_0 \tau_{\text{K}}/\hbar)^{K/(1-K)}. \tag{2.66}$$

Corrections to the linear behavior derive from an analysis of the Josephson junction in the strong coupling limit [97, 23] and take the form (compare to the duality relation in Sec. 2.2)

$$V - IR \sim -\frac{\hbar\pi^2\lambda^2}{e\tau_{\text{K}}} \frac{1}{\Gamma(2K)} \left[\frac{\pi I \tau_{\text{K}}}{e}\right]^{2/K-1}. \tag{2.67}$$

It follows that with increasing currents the overall resistance decreases as the phase slips no longer block the wire and currents flow across both channels, i.e., the superconducting wire and the parallel shunt resistor. The current-voltage characteristic exhibits a zero bias resistance peak which is the signature of the insulating phase. The linear response regime applies to voltages smaller than $2eV_{\mathrm{W}} = \max(\partial_q \varepsilon) \sim W$ or, equivalently, currents $I < I_{\mathrm{W}} \equiv V_{\mathrm{W}}/R = eKW/(\pi\hbar)$.

In general, the crossover current I_{W} is small compared to the current scale Ke/τ_{K}, i.e., $I_{\mathrm{W}} \ll Ke/\tau_{\mathrm{K}}$, as the vortex fugacity is small $\lambda \ll 1$. Then, the resistance peak takes place in the regime with a logarithmic interaction $K \ln \overline{r}^2$ between the vortex-antivortex pairs, and the system behaves equivalent to the exactly solvable boundary sine-Gordon model (see appendix D). Then, the current-voltage characteristic derives from the response function of the boundary sine-Gordon model [110] $V = X_I(K, T, I)$ for $I < eK/\tau_{\mathrm{K}}$ and $T < \hbar/\tau_K$. Note, that for a small vortex fugacity λ, the zero bias resistance peak becomes narrow and a high experimental resolution is required for the observation of the insulating phase.

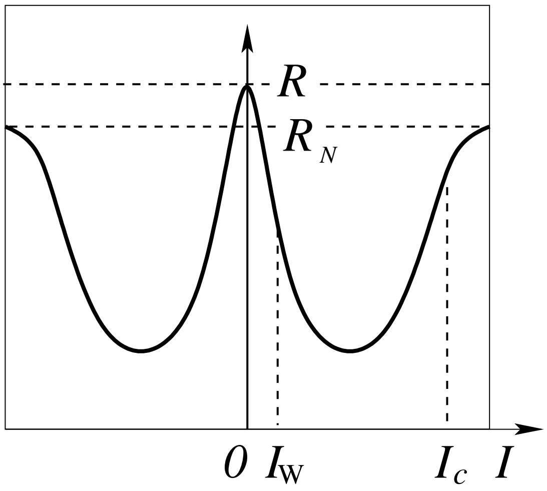

Figure 2.12: Sketch of the current-voltage characteristic for the insulating phase at $T = 0$. At low currents, the nucleation of phase slips blocks the current through the wire, and the system exhibits a linear resistance as the currents flow across the parallel shunt. At higher currents $I > I_{\mathrm{W}}$, the resistance decreases and the current-voltage characteristic exhibits a sharp zero-bias resistance peak; the signature of the insulating phase. Above the depairing current I_c the wire turns normal.

2.7 Conclusions

In one-dimensional disordered wires superconductivity is suppressed by two mechanisms: (i) high energy fluctuations of the *fermionic* electrons, and (ii) low energy fluctuations of the *bosonic* Cooper pairs.

Starting with the effects induced by the high energy fluctuations, disorder decreases the dynamical screening properties of the *fermionic* electrons and increases the effectiveness of the Coulomb interaction, which in turn reduces the mean-field critical temperature T_{c0}. For strong disorder this *fermionic* high energy physics quenches superconductivity giving way to an insulating ground state. Weak disorder provides a finite mean-field critical temperature T_{c0}, below which the formation of *bosonic* Cooper pairs takes places. The low energy action of the Cooper pairs is characterized by sound modes with sound velocity c_s, the dimensionless addmitance μ and the vortex fugacity λ. In thick wires, these parameters derive from the bulk superconducting parameters via a mean-field approach. However, dimensional reduction and disorder renormalize these parameters in thin wires. To our knowledge, a microscopic derivation for these parameters taking into account the renormalization via the *fermionic* high energy fluctuations is missing and is a challenging task for future work.

The bosonic fluctuations of Cooper pairs tends to destroy both order (the condensate) and stiffness (the superfluid density): at finite temperatures, topological fluctuations in the form of phase slips generate a residual ohmic resistance, thus destroying the superconducting phase. Hence, superconductivity can only survive at zero temperature. Infinite wires undergo a zero temperature superconductor–insulator (SI) quantum phase transition in the dimensionless admittance μ: for $\mu > \mu_c = 2$ the wire is superconducting, while for $\mu < \mu_c$ the ground state turns insulating.

In real experiments, the finite length L of the wire has to be taken into account: the quantum phase transition at μ_c then transforms into a crossover, see Fig. 2.1, with μ_c separating a 'strong' superconductor at $\mu > \mu_c$ from a 'weak' one at $\mu < \mu_c$; the latter is characterized by a largely increased fugacity for small vortex–anti-vortex pairs of size $\overline{\tau} < L/\pi c_s$, producing large voltages at current drives $I > I_{\mathrm{dec}}$. While the finiteness of the wire destroys the quantum phase transition in the wire parameter μ, the coupling to the environment through the wire's boundaries leads to the appearance of a new quantum phase transition in the parameter K, the dimensionless conductance characterizing the environment.

The quantum phase transition at $K = 1$ again separates a superconducting phase at $K > 1$ from an insulating one at $K < 1$. This resurrected SI quantum phase transition is different from the one in the infinite system; it is of the type inherent to finite systems coupled to a dissipative environment, e.g., the resistively shunted Josephson junction [23] or the dissipative two state system [24]. The internal dynamics of the system (as parametrized by the admittance μ and by the fugacity λ) now plays a minor role, while the external dissipative dynamics characterized by the dimensionless parameter K drives the quantum phase transition.

Experimentally, the superfluid- and insulating phases can be identified via their different nonlinear current–voltage characteristic. Most importantly, the thermodynamic state of the wire, superconducting or insulating, is always controlled by the environment as parametrized by the dimensionless conductance K; the latter then also determines the overall shape of the current–voltage characteristic. The internal parameters of the wire, its admittance μ and the vortex fugacity λ, play an essential role in determining the detailed shape of the current–voltage characteristic, as we are going to discuss now.

In order to probe the superconducting properties of the quantum wire we have to 'protect' it by a well conducting shunt with $K > 1$. Furthermore, in order to probe the wire itself, the shunt's conductance K has to be much larger than the wire's admittance μ; otherwise, the entire nonlinear current–voltage is dominated by the environment. Indeed, for $K \gg \mu$ the high current response above the critical deconfinement current I_{dec} directly probes the quantum wire, see (2.61), while the environment manifests itself only at low current densities, see (2.58). A finite temperature provides a residual resistance at very small drives via the thermal nucleation of phase slips; this residual resistance strongly depends on temperature, and is suppressed by a small vortex fugacity λ^2. A schematic drawing of the current–voltage characteristic is shown in Fig. 2.11.

The insulating phase is established at small values $K < 1$; the SI quantum phase transition has to be traced by the tuning of the environment (via the conductance K) rather than by a change in the wire's admittance μ; tuning μ merely provides a crossover in the wire's superconducting properties observable at large K. In the insulating phase the current transport across the wire is blocked by the proliferation of phase slips and the driving current flows across the parallel shunt resistance. As a result, the current–voltage characteristic develops a large voltage at small drives. Increasing the current beyond a characteristic value $I_{\mathrm{W}} \approx e\lambda^{1/(1-K)}/(\pi\overline{\tau}_{\mathrm{B}})$, the phase slips cannot block the entire current and a finite supercurrent flows through the wire, reducing the resistance of the system. Hence, the current–voltage response of the insulating phase is characterized by a zero-bias resistance peak, see Fig. 2.12, with the peak height scaling with the external shunt resistance R, while its width scales with I_{W}. The main feature allowing for the distinction between the superconducting and the insulating phase then is the appearance of this zero-bias resistance peak. Note that within the present analysis the vortex fugacity λ has been assumed to be small; increasing $\lambda \to 1$ drives the system towards strong coupling and the mean-field superconducting ground state is no longer an appropriate starting point. Hence within the present scheme, the observation (and consistent interpretation) of the characteristic resistance peak requires a sufficiently sensitive voltage- or current probe as $I_{\mathrm{W}} \propto \lambda^{1/(1-K)}$.

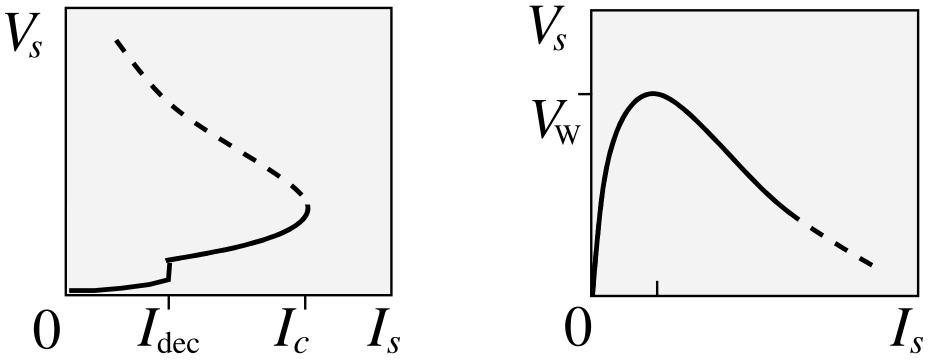

Figure 2.13: Relation between the current I_s and voltage V_s across the wire. The superconducting phase (right) is characterized by a vanishing linear resistance. The step at the decoupling current I_{dec} appears only in the limit $K \gg \mu$ as a consequence of the confinement of vortex-antivortex pairs. In the insulating phase (left), the system exhibits a Coulomb gap with a peak V_{W} smeared by quantum fluctuations.

All the results presented here, assumed a perfect current source with a parallel shunt resistor. The discussion in Sec. 2.2 has shown that the results for this shunted situation can be translated to the current-voltage characteristic of an arbitrary system. Of special interest is the relation between the current I_s and the voltage V_s across the junction, which derives from relation (2.3). A sketch of this intrinsic current-voltage characteristic is shown in Fig. 2.13. The superconducting phase is characterized by a vanishing linear resistance. The step at the decoupling current I_{dec} appears only in the limit $K \gg \mu$ as a consequence of the confinement of vortex-antivortex pairs. In the insulating phase, the system exhibits a Coulomb gap with a peak value V_{W} demonstrating the insulating behavior of the wire. Note, that the Coulomb gap is smeared by quantum fluctuations.

Finally, we turn to the recent experiments on ultrathin superconducting wires by Bezryadin *et al* [40] and by Lau *et al* [41]. These experiments were performed on a large number of amorphous MoGe wires with various cross sections $S \approx 40 - 100\,\text{nm}^2$ and lengths ranging from $L \approx 100\,\text{nm}$ to $L \approx 1\,\mu\text{m}$. They observe a systematic broadening of the superconducting transition at $T_{c0} \approx 5\,\text{K}$ with decreasing cross section S, and even a crossover to an insulating behavior of the wires. The authors in Ref. [40, 111] concluded, that this cross over is a manifestation of the superconductor to insulator quantum phase transition predicted by Zaikin *et al.* [14] appearing for a normal resistance $R_N = R_Q$. This first finding turned out to be erroneous as measurements performed on longer wires indicated that the crossover appears rather at $R_\xi \approx R_Q$ [41]; a proper explanation of the experimental results is still missing today. Here, we examine these experimental observations in terms of a phase slip driven superconductor to insulator quantum phase transition. We find that the sound velocity c_s is in the range $c_s \sim 10^6$ m/s implying that the energy scale $\hbar\pi c_s/L \sim 20\,\text{K}$ is even above the mean field superconducting transition temperature $T_{c0} \sim \hbar/\kappa$. As a consequence, these wires are extremely short in terms of bosonic fluctuations and the phase slip dynamics is dominated by the coupling to the environment, while the signature of the phase transition in the infinite system play a minor role. The experimental setup excludes the existence of a parallel shunt resistor. Then, the wire is voltage biased and the impedance of the current carrying lead plays an important role; see the discussion in Sec. 2.2. Therefore, the observation of a phase-slip driven quantum phase transition studied in this chapter requires special current carrying leads allowing for a nearly frequency independent impedance up to frequencies $1/\kappa$ [25, 26]. Unfortunately, such a high control of the environment has not been achieved in the experiments on ultrathin wires [40, 41], indicating that a different mechanism drives the observed crossover. We expect that this different mechanism is provided by the high resistivity of the wires with $R_\xi \approx R_Q$. Then, the vortex fugacity λ becomes large with $\lambda \sim 1$, and the instanton expansion turns invalid, while the fermionic renormalization becomes very important.

In conclusion, phase slips are a fluctuation induced perturbation of the mean-field superconducting ground state. A finite wire exhibits a quantum phase transition, where the competition between internal parameters of the wire and the external parameters of the environment entails a rich phase diagram. The insulating phase is characterized by a Coulomb gap. The current experimental techniques of fabricating ultrathin wires [40, 41] combined with a setup allowing for the implementation of a well defined environment [25, 26], puts the observation of a phase slip driven quantum phase transition in thin superconducting wires into experimental reach and defines a challenging task for future experiments.

Chapter 3

Superfluidity versus Bloch Oscillations in Confined Atomic Gases

3.1 Introduction

Bose-Einstein condensation [53, 54] and superfluidity [112] are basic characteristics of bosonic quantum gases and fluids. While the Bose-Einstein condensate (of density n_0) is a thermodynamic quantity characterizing off-diagonal-long-range *order*, the superfluid density n_s describes the *response* to a perturbation in the broken phase [6]. In real quantum liquids, such as bulk ^{4}He, condensation and superfluidity appear in unison, but in general one may be realized without the other. For example, noninteracting Bose gases in three dimensions form a condensate without superfluidity as the critical velocity vanishes. In 2D, a quantum liquid such as ^{4}He exhibits quasi-long-range order below the Kosterlitz-Thouless transition temperature T_{KT}. This quasi-long-range order is sufficient to establish a superfluid response, hence superfluidity appears without a true condensate. In one dimension superfluidity and quasi-long-range order may survive only at zero temperature.

First attempts to probe the (bulk) superfluid properties in condensed atom gases have been carried out recently [61]. The Bose-Einstein condensate is perturbed by a moving laser beam which creates excitations above a critical velocity, while below the critical velocity the motion appears free of dissipation. The results on the critical velocity are in rough agreement with expectations deriving from a weak coupling analysis based on the Gross-Pitaevskii theory [113, 114, 63, 115, 116, 64]. An interesting question then arises regarding the interplay of superfluidity and enhanced thermal/quantum fluctuations due to dimensional reduction. In this chapter we study the superfluid properties of (quasi) one-dimensional bosonic atom gases in traps with finite geometries, where quantum phase slips tend to destroy superfluidity. The results are compared to the thermodynamic limit of an infinitely long tube. While interesting on their own, these questions have attracted much attention recently, as novel atom chip technology [84, 117], magnetic traps with high aspect ratios [81], and optical 2D lattices [118, 69] allow for the experimental realization of strongly confined atom gases exhibiting large quantum fluctuations.

The destruction of dissipation free-flow in one dimensional superconductors and superfluids is triggered by the appearance of quantum phase slips as discussed by Zaikin *et al.* [14] and in chapter 2 for metal wires and by Kagan *et al.* [119, 34] for superfluid rings. The superfluid flow can be set up in different ways: first, the flow can be driven by a phase difference across the reservoirs. On the other hand, the motion of an impurity with velocity v in a superfluid also induces a local flow and offers a different experimental realization for studying transport. Here, we derive an effective low energy action describing the dynamics of the phase difference across a moving impurity. The quantum nucleation rate for phase slips determines the response: at finite temperatures the infinite system exhibits a linear response and hence is not superfluid, $\Delta\mu \propto v$ with $\Delta\mu$ the drop in the chemical potential across the impurity. This contrast with the ring geometry where interactions quench the phase slip nucleation below a critical velocity, thus establishing a superfluid response. In a finite tube the quantum phase slips proliferate and the new non-superfluid ground state exhibits Bloch oscillations in the chemical potential difference across the moving impurity, $\Delta\mu \propto \sin(2\pi n v t)$ with n the 1D atom density. The physical origin of these oscillations is found in the particle quantization: the moving impurity enhances the particle density in front, producing a chemical potential difference across the impurity, which in turn is released each time an atom tunnels through the impurity.

In Section 3.2, we discuss the different setups for driving a flow through an impurity: whether the flow is driven by a phase difference in the reservoirs or by a moving impurity with velocity v mainly differs in a Galilei transformation of the system. We then focus on the moving impurity in a superfluid and present the derivation of the effective action for the phase difference across the impurity

(Section 3.3) for the case of a weakly interacting Bose system. This derivation starts from the Gross-Pitaevskii equation and represents a consistent expansion in the low frequency limit. The response to the driving force induced by the motion of the impurity shows a quantum phase transition which is discussed in Section 3.4.1, while the calculation of the quantum nucleation rate is carried out in Section 3.4.2. Finally, we focus on realistic systems of finite size in the last section 3.5, and discuss the two opposing geometries separately. The results discussed in this chapter have been published in [120].

3.2 Experimental setups

Transport properties in charged superfluids are conveniently studied by current biasing the circuit via external electrical devices. In particular, using such experimental setups the quantum fluctuations of the superconducting wave function in a small Josephson junction device [22] and in thin superconducting wires have been examined [13, 40]. The corresponding theoretical description is based on a fixed phase difference between the superconducting leads driving the flow in the system [17, 14] and the quantum nucleation of phase slips leads to a non trivial current-voltage characteristic (a flow-pressure characteristic for uncharged superfluids, respectively). Similar results have been derived by studying the stability of a supercurrent in a ring for charged [34] and uncharged superfluid [119], where the phase difference across the reservoirs is replaced by the condition of periodicity across the ring, or the renormalization of the critical current of a Josephson junction in a flux driven superconducting ring [35].

Recently, a new type of experiments has been set up determining the superfluid flow of a weakly interacting Bose-Einstein condensate around an impurity [61]. In this setup the flow is induced by the motion of an impurity, e.g., a laser beam repelling the atoms from its focus. Galilei invariance then implies that this setup differs only by a Galilei transformation from the usual setup used in the analysis of superconducting systems. While these experiments have been performed in bulk superfluids, here we study quasi one-dimensional situations with a small transverse channel size, where the excitation energy for transverse modes is larger than the temperature and the characteristic energy scale of the longitudinal modes. The relevant design parameters of an experiment allowing for the observation of interesting quantum effects will be discussed in Section 3.6.

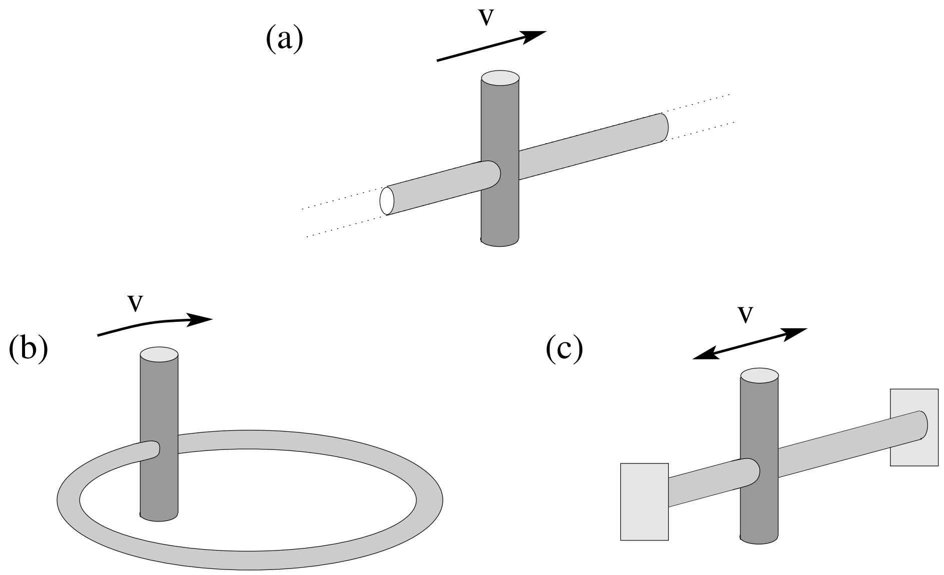

Figure 3.1: Superfluid in a small thin cylindrical trap with a moving impurity: (a) infinite wire,(b) ring structure with periodic boundary condition for the condensate wave function, (c) finite system of length L with closed ends.

The effect of phase slips is most conveniently studied in a superfluid ring with length L where the impurity is moving with uniform velocity v (see Fig. 3.1(b)). The creation of a phase slip leads to an additional winding of the superfluid phase describing an acceleration of the superfluid, which in turn is related to a suppression of the order parameter, i.e., particles leave the condensate. The finite length L together with the periodic boundary conditions provides us with a quantization of the velocity of the superfluid in units $2v_L = 2\pi\hbar/Lm$, i.e., a phase slip leads to an increase of the mean velocity by $2v_L$. As a consequence, the relative velocity v_{rel} between the superfluid and the uniformly moving impurity decreases by a rate which can be estimated as

$$\partial_t v_{\mathrm{rel}} = -2\,\Gamma(v_{\mathrm{rel}})\,v_L, \tag{3.1}$$

where Γ denotes the quantum nucleation rate for phase slips. When the relative velocity between the superfluid and the impurity is smaller than the critical velocity necessary for the nucleation of phase slips we reach an equilibrium state. Switching on the laser beam during a time Δt the amount of energy transferred to the superfluid is given by

$$\Delta E = \int_{\Delta t} dt \Gamma(v) E_{\mathrm{PS}}(v), \tag{3.2}$$

with $E_{\mathrm{PS}}(v)$ the energy transferred by a single phase slip event. Two methods for measuring this energy transfer have been applied in experiments on bulk superfluids: the determination of the heating of the condensate by measuring the thermal fraction [61, 62] and the direct observation of the flow field in the superfluid by *in situ* non-destructive imaging of the condensate [62].

Increasing the length of the superfluid ring, finite size effects become irrelevant and the behavior of the ring approaches that of an infinitely long wire. This situation is illustrated in Fig. 3.1(a). In contrast to the ring setup, the impurity never returns to its initial position. As a consequence, only parts of the superfluid are accelerated by a phase slip and waves traveling with a velocity close to the sound velocity carry away the energy transferred to the superfluid.

Closing the wire with impenetrable boundaries at a separation L (Fig. 3.1(c)), these sound waves are reflected and provide a homogeneous heating of the sample due to the nucleation of phase slips. In order to avoid contact with the boundaries the laser beam is oscillating, e.g., $v_0(t) = \omega R \cos \omega t$. Such a setup was used in experiments on bulk superfluids.[61] The oscillation of the impurity results in an undirected acceleration of the superfluid via phase slip nucleation, and the mean relative velocity between the superfluid and the impurity does not decrease. The total amount of energy transferred to the superfluid is again given by Eq. (3.2).

3.3 Effective Action

We start with the Gross-Pitaevskii Lagrangian describing the dynamics of the confined condensate wave function of the weakly interacting bosons [60]. With m the mass of the bosons, U the strength of the repulsion, and ρ_0 the condensate density, the Lagrangian in one dimension reads

$$\mathcal{L}_{GP} = i\hbar\, \overline{\psi} \partial_t \psi - \frac{\hbar^2}{2m} (\partial_x \overline{\psi})(\partial_x \psi) - \frac{U}{2} \left[\overline{\psi}\psi - \rho_0 \right]^2 \tag{3.3}$$

with ψ and $\overline{\psi} = \psi^*$ the bosonic field. The repulsive interaction U produces the healing length $\xi = \hbar/\sqrt{m\rho_0 U}$ and a finite compressibility κ related to the sound velocity $c_s = \sqrt{\kappa/m\rho_0} = \sqrt{\rho_0 U/m}$. Comparison of the length scale ξ with the scale given by the condensate density $1/\rho_0$ provides us with a dimensionless parameter $K = \pi\xi\rho_0$, the number of particles per healing volume measuring the relevance of fluctuations. The condition of weakly interacting bosons where a mean field description is valid translates into $K \gg 1$. The energy scale of the interaction is given by the chemical potential $\mu = \rho_0 U$. Below, we consider the case of an infinite superfluid and ignore the confining potential V_{ext} of the magnetic traps: realistic systems with finite geometries will be discussed in Section 3.5.

The impurity is described by a suppression of the chemical potential

$$\mathcal{L}_{\mathrm{int}} = -V(x - vt)\overline{\psi}\psi \tag{3.4}$$

with v the velocity of the impurity. Below, we will consider a short range interaction between the impurity and the superfluid, i.e., $V(x) = g\xi\delta(x)$, with impurity strength $g \gg \mu$ providing us with a small parameter μ/g. The time dependence of the impurity potential $V(x - vt)$ can be shifted to the wave function by applying the variable transformation $x \to x - vt$, $t \to t$ mapping the system into a frame with the impurity at rest. Note that this transformation differs from a Galilei transformation which acts on the condensate wave function via $\psi \to \psi \exp[i(xv - v^2t/2)/\xi c_s]$. The Lagrangian of the system in the impurity rest frame then reads

$$\begin{aligned}\mathcal{L} &= i\hbar\,\overline{\psi}\partial_t\psi - \frac{\hbar^2}{2m}(\partial_x\overline{\psi})(\partial_x\psi) - \frac{U}{2}\left[\overline{\psi}\psi - \rho_0\right]^2 \\ &\qquad\qquad + V(x)\overline{\psi}\psi - i\hbar v\overline{\psi}\partial_x\psi.\end{aligned} \tag{3.5}$$

The last term in (3.5) is driving a flow and derives from the variable transformation.

In order to study the quantum behavior of the superfluid we go over to the Euclidean action [121]

$$\mathcal{S} = \int_0^{\hbar\beta} d\tau \int dx \left[\hbar\,\overline{\psi}\partial_\tau\psi + \mathcal{H}\left[\overline{\psi},\psi\right]\right], \tag{3.6}$$

with τ the imaginary time, $\beta = 1/T$ the inverse temperature, and $\mathcal{H}\left[\overline{\psi},\psi\right]$ the Hamiltonian density,

$$\mathcal{H}\left[\overline{\psi},\psi\right] = \frac{\hbar^2}{2m}(\partial_x\overline{\psi})(\partial_x\psi) + \frac{U}{2}\left[\overline{\psi}\psi - \rho(x)\right]^2 - i\hbar v\overline{\psi}\partial_x\psi,$$

where $\rho(x) = \rho_0 - V(x)/U$. A saddle point solution extremizing the above action involves ψ and $\overline{\psi}$ as independent variables; this freedom allows for an analytic continuation of the action extending $\psi = \alpha + i\beta$ with $\alpha, \beta \in \mathbf{R}$ into the complex plane via $\psi = \alpha + i\beta$ with $\alpha, \beta \in \mathbf{C}$. Performing functional derivatives produces the equations

$$\begin{aligned} -\hbar\, \partial_\tau \psi &= -\frac{\hbar^2}{2m}\partial_x^2 \psi + U\left[\overline{\psi}\psi - \rho(x)\right]\psi - i\hbar v \partial_x \psi\,, && (3.7) \\ \hbar\, \partial_\tau \overline{\psi} &= -\frac{\hbar^2}{2m}\partial_x^2 \overline{\psi} + U\left[\overline{\psi}\psi - \rho(x)\right]\overline{\psi} + i\hbar v \partial_x \overline{\psi}\,. && (3.8) \end{aligned}$$

Note that with $\psi(\tau)$ and $\overline{\psi}(\tau)$ satisfying Eqs. (3.7) and (3.8) the configuration $\overline{\psi}^{\,*}(-\tau + a)$, $\psi^*(-\tau + a)$ is also a solution, with ψ^* the complex conjugate of ψ and $a \in \mathbf{R}$. Furthermore, for time independent solutions follows $\overline{\psi} = \psi^*$, while the finite temperature demands periodic boundary conditions for ψ and $\overline{\psi}$, i.e., $\psi(x, \tau + \hbar\beta) = \psi(x, \tau)$ and $\overline{\psi}(x, \tau + \hbar\beta) = \overline{\psi}(x, \tau)$.

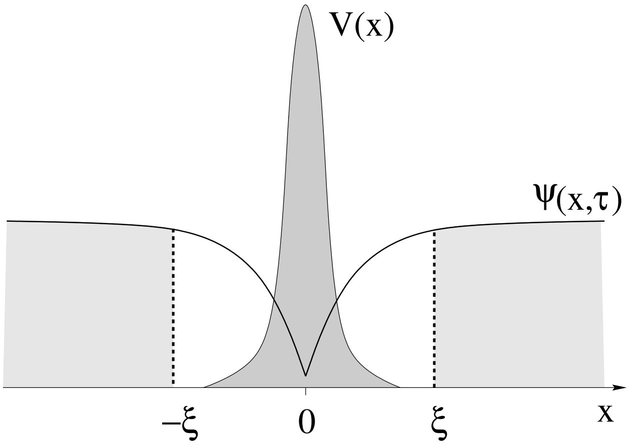

Figure 3.2: Form of the condensate wave function near the impurity: the repulsive interaction with the impurity potential $V(x)$ leads to a dip in the condensate wave function. For short range interactions the distortion of the wave function by the impurity decays exponentially on the scale ξ.

In the following we first derive an effective action for the phase difference $\vartheta(\tau) = \theta(\tau, \xi) - \theta(\tau, -\xi)$ and $\overline{\vartheta}(\tau) = \overline{\theta}(\tau, \xi) - \overline{\theta}(\tau, -\xi)$ across the impurity in the infinitely long system (see Fig. 3.1(a)) by integrating out all degrees of freedom except ϑ and $\overline{\vartheta}$, where the phase fields θ and $\overline{\theta}$ of the superfluid condensate are defined via

$$\psi = \sqrt{\rho_0}\,(1 + h)\, e^{i\,\theta}, \qquad \overline{\psi} = \sqrt{\rho_0}\left(1 + \overline{h}\right) e^{-i\,\overline{\theta}}. \tag{3.9}$$

Here, h and $\overline{h}$ account for variations in the modulus. The integration is split into two parts: first the region $[-\xi, \xi]$ containing the impurity and producing the action $\mathcal{S}_{\text{imp}}$, and second, the contribution of the superfluid leads in the regions $[-\infty, -\xi]$ and $[\xi, \infty]$ with the actions $\mathcal{S}_{R(L)}$ for the right (left) lead. The total action then reads

$$\mathcal{S} = \mathcal{S}_R + \mathcal{S}_L + \mathcal{S}_{\text{imp}}. \tag{3.10}$$

Note, that the phase fields θ and $\overline{\theta}$ are compact variables, i.e., two phases θ_1 and θ_2 with $\theta_2 - \theta_1 \in 2\pi\mathbf{Z}$ are indistinguishable and describe the same quantum mechanical state. Then, depending on the setup, the effective variable ϑ can be compact with $\vartheta \in [0, 2\pi)$ or extended with $\vartheta \in \mathbf{R}$. We will postpone the detailed discussion of this subtle issue and first present the derivation of the effective action.

3.3.1 Integrating out the impurity

We start with integrating out the region $[-\xi, \xi]$. The modulus of the wave function becomes small due to the repulsion of the condensate by the impurity and the nonlinear terms in the Gross-Pitaevskii equation (3.7) and (3.8) are relevant. The dynamics of the wave function is determined by the fast time scale $\tau_0 = \hbar/\mu$. On the other hand, we will see that the relevant time scale $\tau_c = \tau_0 g/\mu$ in the effective action for ϑ is determined by the strength g of the impurity and with $g \gg \mu$ the scale τ_c is much slower than τ_0. Therefore, we ignore the dynamics in (3.7) and (3.8), which implies $\overline{\psi} = \psi^*$, and solve the time independent equations with adiabatic boundary conditions.

Time independent solutions of Eq. (3.7) have been derived by Hakim [114]. The left and the right side of the dip in the wave function (see Fig. 3.2) are described by the dark soliton solutions

$$\psi(x)^{\pm} = \frac{(v/c_s + i\xi\lambda)^2 + \exp\left[\lambda\left(x \mp x_0\right)\right]}{1 + \exp\left[\lambda\left(x \mp x_0\right)\right]} e^{i\chi^{\pm}} \tag{3.11}$$

with $(v/c_s)^2 + (\xi\lambda)^2 = 1$. The wave function is continuous at $x = 0$, i.e., $\psi^+(0) = \psi^-(0)$, determining $\chi^{\pm}$, while the δ-function interaction enforces the matching condition

$$\frac{\xi}{2}\left[\partial_x\psi^+(0) - \partial_x\psi^-(0))\right] = \frac{g}{\mu}\psi(0) \tag{3.12}$$

determining x_0. In the relevant limit $g \gg \mu$, we find $g x_0/\mu\xi = 1 + \sqrt{1 - v^2/v_c^2}$ with $v_c = \mu c_s/g$. The perturbation induced by the impurity decays exponentially in the leads and the solution $\psi(x)$ reduces to a phase shift on the scale ξ, i.e., $\psi(\pm\infty) \to \sqrt{\rho_0}\exp(i\theta(\pm\xi))$.

Inserting the solution into the action (3.6) produces the effective action for the region $[-\xi,\xi]$ describing the corresponding phase difference $\vartheta = \theta(\xi) - \theta(-\xi)$. For a strong interaction parameter $g \gg \mu$ this action takes the form of the usual Josephson coupling term

$$\mathcal{S}_{\text{imp}} = \int d\tau \,\{E_J\,[1-\cos\vartheta(\tau)] - \hbar\rho_0 v \vartheta(\tau)\} \tag{3.13}$$

with the Josephson coupling energy $E_J = K\mu^2/g\pi$ and the mean field solution for the flow dependent phase shift across the impurity

$$v = v_c \sin\vartheta \tag{3.14}$$

with the critical velocity $v_c = c_s\mu/g$.

3.3.2 Integrating out the leads

Next, we focus on the contribution of the leads. The superflow in the leads is limited by the small critical velocity of the impurity, producing perturbations h, $\overline{h}$, $\partial_x\theta$, $\partial_x\overline{\theta}$, $\partial_\tau\theta$, and $\partial_\tau\overline{\theta}$ of order μ/g. Inserting the ansatz (3.9) into (3.8), the modulus and phase decouple to lowest order in μ/g, and the equations for the phases θ and $\overline{\theta}$ take the form

$$-\tau_0\,\partial_\tau\theta(x,\tau) + (\xi^2/2)\,\partial_x^2\theta(x,\tau) = \sin 2\left[\phi^-(x,\tau)\right], \tag{3.15}$$

$$\tau_0\,\partial_\tau\overline{\theta}(x,\tau) + (\xi^2/2)\,\partial_x^2\overline{\theta}(x,\tau) = \sin 2\left[\phi^-(x,\tau)\right], \tag{3.16}$$

with $\phi^\pm(x,\tau) = [\theta(x,\tau) \pm \overline{\theta}(x,\tau)]/2$. The left side defines a diffusion equation, while the right side describes a nonlinear coupling of the phases. The Eqs. (3.15) and (3.16) decouple for time independent solutions ($\overline{\psi} = \psi^*$ which implies $\phi^- = 0$) and a linearization in ϕ^- is justified for a slow time dependence. Applying a Fourier transformation then leads to

$$-\xi^2 k^2 \begin{pmatrix} \phi^+ \\ \phi^- \end{pmatrix} = \begin{bmatrix} 0 & 2i\omega\tau_0 \\ 2i\omega\tau_0 & 4 \end{bmatrix} \begin{pmatrix} \phi^+ \\ \phi^- \end{pmatrix}, \tag{3.17}$$

defining modes with a dispersion relation $-\omega^2/c_s^2 = k^2\,(1+\xi^2k^2/4)$ [122]. Next, we solve (3.17) for the phases in the right lead $x > \xi$ with the boundary conditions

$\phi^{\pm}(x \to \infty, \tau) = 0$ and $\phi^{+}(\xi, \omega) = p(\omega)$ and $\phi^{-}(\xi, \omega) = q(\omega)$,

$$\begin{aligned} \phi^{+}(x,\omega) &= \frac{1}{\lambda_- - \lambda_+}\Big\{ \left[\lambda_-\, p - 2i\omega\tau_0\, q\right] e^{-s_+(x/\xi-1)} \\ &\qquad - \left[\lambda_+\, p - 2i\omega\tau_0\, q\right] e^{-s_-(x/\xi-1)}\Big\}\ , \end{aligned} \tag{3.18}$$

$$\begin{aligned} \phi^{-}(x,\omega) &= \frac{\lambda_+\lambda_-}{\lambda_- - \lambda_+}\Big\{ \frac{\lambda_-\, p - 2i\omega\tau_0\, q}{2i\omega\tau_0\lambda_-} e^{-s_+(x/\xi-1)} \\ &\qquad - \frac{\lambda_+\, p - 2i\omega\tau_0\, q}{2i\omega\tau_0\lambda_+} e^{-s_-(x/\xi-1)}\Big\}\ , \end{aligned} \tag{3.19}$$

with $\lambda_{\pm} = 2(1 \pm \sqrt{1-\omega^2\tau_0^2})$ and $s_{\pm} = \sqrt{\lambda_{\pm}}$. Inserting the solution back into the effective action $\mathcal{S}_R$, Eq. (3.6), we concentrate on the first term (the second term involves the Hamiltonian $H = \int dx\mathcal{H}$ which is conserved under time evolution and therefore does not contribute). Linearizing in the small quantities h, $\partial_x\phi$, and $\partial_\tau\phi$, ($\overline{h}$, $\partial_\tau\theta$, $\partial_x\theta$, respectively), the variations h and $\overline{h}$ of the modulus drop out and the action is determined by the phase fields alone,

$$\mathcal{S}_R = \hbar\rho_0 \int_{-\infty}^{\infty} \frac{d\omega}{\pi} \int_{\xi}^{\infty} dx\, i\,\omega\, \phi^{+}(x,\omega)\, \phi^{-}(x,-\omega)\, . \tag{3.20}$$

(Note that at finite temperature the integration $\int_{-\infty}^{\infty} d\omega/2\pi$ is replaced by the corresponding summation over Matsubara frequencies: $1/(\hbar\beta)\sum_s$ with $\omega_s = 2\pi s/\hbar\beta$, $s \in \mathbf{Z}$). A straightforward calculation leads to the effective action for the phases $\phi^{+}(\xi,\tau) = p$ and $\phi^{-}(\xi,\tau) = q$ on the right side of the weak link

$$\mathcal{S}_R = \frac{\hbar K}{\pi}\int_0^{\infty} \frac{d\omega}{4\pi} \frac{\omega}{(1+\omega\tau_0)^{1/2}} \left[|p+iq|^2\, \frac{2+\omega\tau_0}{1+\omega\tau_0} - 2|q|^2\right]$$

with $K = \pi\rho_0\xi$ the number of particles per healing length. An expansion in $\omega\tau_0$ is equivalent to an expansion in v_c/c_s and we obtain to lowest order

$$\mathcal{S}_R = \frac{\hbar K}{\pi} \int_{-\infty}^{\infty} \frac{d\omega}{4\pi} \left[\, |\omega||p|^2 + 2i\omega p^* q\right]\ . \tag{3.21}$$

The first term is a Caldeira-Leggett type damping [17] for p with the kernel $Q(\omega) = K|\omega|$ and describes the flow of energy into the leads via sound waves. The second term accounts for accumulation of particles at the boundary and produces a 'charging' energy across the impurity.

3.3.3 Action for the phase difference

An analogous calculation with $\theta(-\xi,\tau)$ and $\overline{\theta}(-\xi,\tau)$ adds a similar effective action for the phase on the left side of the link. Adding up terms from the leads and the link, we obtain the total effective action for the phase differences $\vartheta(\tau) = \theta(\xi,\tau) - \theta(-\xi,\tau)$ and $\overline{\vartheta}(\tau) = \overline{\theta}(\xi,\tau) - \overline{\theta}(-\xi,\tau)$ across the weak link (minimization with respect to the 'center of mass' variable $\vartheta_{cm}(\tau) = \theta(\xi,\tau) + \theta(-\xi,\tau)$ gives $\vartheta_{cm} = 0$ and $\overline{\vartheta}_{cm} = 0$, respectively). Introducing the notation $\varphi^{\pm} = \left[\vartheta(\tau) \pm \overline{\vartheta}(\tau)\right]/2$ we obtain

$$\begin{aligned}\frac{\mathcal{S}}{\hbar} &= \frac{K}{2\pi}\int d\tau\Big[\int d\tau' \frac{[\varphi^+(\tau)-\varphi^+(\tau')]^2}{4\pi\,(\tau-\tau')^2} - \varphi^-(\tau)\partial_\tau\varphi^+(\tau)\Big] \\ &\quad + \int d\tau\left\{\frac{E_J}{\hbar}\left[1 - \frac{\varphi^-(\tau)^2}{2} - \cos\varphi^+(\tau)\right] - \rho_0 v\varphi^+(\tau)\right\}.\end{aligned}$$

Integrating out the phase $\varphi^- = -(\hbar K/2\pi E_J)\,\partial_\tau\varphi^+$ in $\mathcal{S}$ provides a mass term $\hbar\int d\tau\ (\hbar/E_C)(\partial_\tau\varphi^+)^2/2$ with $E_C = 4\pi^2 E_J/K^2$. Collecting terms and calling $\varphi^+ = \varphi$ our new variable, the effective action across the link then is equal to the action for a particle with mass $\hbar/E_C$ and damping $\eta = K/2\pi$ in a periodic potential and driven by the force $\rho_0 v$,

$$\begin{aligned}\frac{\mathcal{S}}{\hbar} &= \int d\tau\left\{\frac{K}{2\pi}\int d\tau' \frac{[\varphi(\tau)-\varphi(\tau')]^2}{4\pi\,(\tau-\tau')^2} + \frac{\hbar}{E_C}\frac{[\partial_\tau\varphi(\tau)]^2}{2}\right. \\ &\quad \left. + \frac{E_J}{\hbar}[1-\cos\varphi(\tau)] - \rho_0 v\varphi(\tau)\right\}. \qquad (3.22)\end{aligned}$$

The time scale τ_c determining the dynamics of this action becomes

$$\tau_c = \frac{K\hbar}{\pi}\frac{1}{E_J} = \frac{4\pi\hbar}{K}\frac{1}{E_C} = \frac{g}{\mu}\tau_0 \qquad (3.23)$$

and derives from comparing the different terms in the action $K/4\pi \sim \hbar/E_C\tau_c \sim E_J\tau_c/\hbar$. The quantity

$$\int_{-\infty}^{\infty} dx\partial_x\phi^+(x,\tau) = 2\pi k \qquad (3.24)$$

defines a winding number $k \in \mathbf{Z}$. A change of the phase from $\varphi \to \varphi + 2\pi n$ modifies the winding number according to $k \to k+n$ via the emission of sound waves into the leads. Therefore, two states with $\varphi_1 - \varphi_2 \in \mathbf{Z}$ are distinguishable and the phase φ is an extended variable with $\varphi \in \mathbf{R}$.

The action (3.22) is known to describe a resistively and capacitively shunted Josephson junction (RCSJ-model) [98] between two charged superconductors. The quality factor defined by $Q = \sqrt{E_J/(\eta^2 E_C)}$ separates two regimes: the junction is overdamped with the damping dominating over the inertia for $Q < 1$, while for $Q > 1$ we enter the underdamped regime with a hysteretic current-voltage characteristic [98]. In the uncharged situation considered here $Q = 1$ and the action is at the boundary between the overdamped and the underdamped regime. Then effects leading to hysteretic behavior become only relevant for velocities close to the critical velocity $v \sim v_c$ and are neglected in the following considerations.

3.4 Infinite Geometry

3.4.1 Thermodynamics

The action (3.22) appears in many contexts with the dimensionless parameter spreading over the entire range $K \in [0, \infty)$ [22, 23, 123]. Therefore, we drop the condition of weakly interacting bosons ($K \gg 1$) and study the thermodynamics of (3.22) for any value of K. The thermodynamics of the system is determined by the partition function $\mathcal{Z}$. First we calculate the partition function via a perturbative expansion in the Josephson coupling strength E_J. This maps the model to that of charged particles with logarithmic interaction in one-dimension, [23]

$$\mathcal{Z} = \sum_{n}^{\infty} \frac{E_J^{2n}}{2^{2n}\left(n!\right)^2} \int_0^{\hbar\beta} \prod_i^{2n} \frac{d\tau_i}{\hbar} \exp\left(\frac{1}{2} \sum_{i \neq j} \nu_i \nu_j G\left(\tau_i - \tau_j\right) \right), \tag{3.25}$$

with $\beta = 1/T$ the inverse temperature and the charge neutrality condition $\sum_i \nu_i = 0$ where $\nu_i = \pm 1$. The interaction between the particles is determined by the correlation function

$$G(\tau) = 2\left\langle \varphi(\tau)\varphi(0) \right\rangle = \frac{1}{K} \ln\left[\left(\frac{\hbar\beta}{\pi}\omega_c \right)^2 \sin^2\left(\frac{\pi\tau}{\hbar\beta} \right) \right], \tag{3.26}$$

where ω_c is a cut-off depending on the short distance behavior of the system. This expansion is convergent for $K < 1$.

On the other hand, we can also apply instanton techniques and expand the phase field in (3.22) in kink-antikink–pairs $\varphi(\tau) = \sum_i^n g_+(\tau - \tau_i^+) + g_-(\tau - \tau_i^-)$, where a single kink can be expressed by the trial function $g^\pm = \pm 2 \arctan(2\tau/\tau_c)$. Then the system also maps onto a gas of charged particles with logarithmic interaction (3.25), but the interaction between a kink-antikink pair is given by

$$G(\tau) = K \ln\left[\left(\frac{\hbar\beta}{\pi\tau_c} \right)^2 \sin^2\left(\frac{\pi\tau}{\hbar\beta} \right) \right] - \ln\frac{E_J \tau_c}{y\hbar}, \tag{3.27}$$

i.e., the interaction strength is reversed, $1/K \to K$. The single kink fugacity y is determined by fluctuations around the kink solution and by the short distance behavior of the system. The instanton expansion converges for $K > 1$. The above mappings imply some kind of duality between the weak ($K < 1$) and the strong ($K > 1$) coupling regimes. This duality will be further discussed in appendix D.

The system shows a quantum phase transition at $K = 1$ [23]. For $K < 1$ the ground state is described by a delocalized state for φ with a linear response and characterizes a normal flow across the impurity, i.e., quantum fluctuations destroy the phase coherence between the superfluid on the left and right side of the impurity. On the other hand, for $K > 1$ the phase φ is localized in a minimum of the potential allowing for a superfluid flow across the impurity. However, quantum fluctuations lead to a finite nucleation rate of phase slips describing a nonlinear response to an applied driving force v. We will calculate this nucleation rate in the next section via an instanton expansion.

For the above trial function $g_\pm$ the time dependence becomes fast near the center of the kink, and therefore the phase $\phi^-(x,\tau)$ becomes large. However, the region of large $\phi^-(x,\tau)$ is limited by ξ along x and by the width τ_c of the kink along the τ direction while the relevant behavior of the phase is determined by the region where the phase ϕ^- is small (Eq. (3.19) shows that the asymmetric part satisfies $v \sim \tau_0 \omega u$ for $|x| > \xi$ instead of $v \sim \tau_c \omega u$ and therefore is suppressed by v_s/c_s). Then, corrections from the region where the linearization in (3.15) and (3.16) is not justified can be included in the single kink fugacity y and merely lead to a renormalization of the prefactor for the quantum nucleation rate.

3.4.2 Quantum Nucleation of Phase Slips

For weakly interacting Bose-Einstein condensates we have the relation $K > 1$ and the nonlinear response can be calculated via instanton techniques. The instanton describes a saddle point solution of the action (3.22) and the quantum nucleation rate Γ takes the form [107] $\Gamma = A \exp(-S_{\mathrm{I}}/\hbar)$ with S_{I} the action of the instanton, while the prefactor is determined by the fluctuations around the classical saddle point solution. Approximating the instanton by a kink-antikink–pair separated by the distance $\overline{\tau}$ leads to the action

$$\frac{\mathcal{S}}{\hbar} = K \ln\left[\left(\frac{\hbar\beta}{\pi\tau_c}\right)^2 \sin^2\left(\frac{\pi\overline{\tau}}{\hbar\beta}\right)\right] - 2\pi\rho_0 v\overline{\tau}. \tag{3.28}$$

The first term describes the logarithmic attraction between a kink-antikink–pair as seen in the previous section, while the linear repulsion arises from driving the system via the motion of the impurity. For $T = 0$ the instanton is determined by the saddle point of the action (3.28) at $\overline{\tau} = K/(v\pi\rho_0)$ and neglecting fluctuations leads to the decay rate $\Gamma \sim \hbar(v/v_c)^{2K}/E_J$. However, fluctuations in the size $\overline{\tau}$ of the kink-antikink–pair are relevant and can be included by calculating the quantum nucleation rate via the relation [109]

$$\Gamma = \frac{y^2}{\tau_c^2}\int_{\tau_c}^{\hbar\beta} d\overline{\tau}\, \exp\left[-\frac{S(\overline{\tau})}{\hbar}\right], \tag{3.29}$$

where the convergence is obtained by an analytic continuation of the integration contour as described in Refs. [107]. The fugacity y is independent of the temperature T and the driving force v and is determined by the remaining fluctuations around the instanton solution.

At finite temperature, thermal fluctuations can also lead to the nucleation of a phase slip decelerating the superfluid with a rate denoted by Γ^- in contrast to the rate Γ^+ for phase slips accelerating the superfluid. The experimentally relevant quantity then is the difference of the two rates $\Gamma = \Gamma^+ - \Gamma^-$ describing the excess of phase slips accelerating the superfluid. The calculation of the integral (3.29) provides us with $\Gamma^+(v)$, while an analytic continuation to values $-v$ produces an expression for Γ^-. The quantum nucleation rate finally becomes [109]

$$\Gamma = \frac{y^2}{\tau_c}\left(\frac{2\pi\tau_c}{\hbar\beta}\right)^{2K-1} \sinh\left(\pi\rho_0\hbar\beta v\right)\frac{\left|\Gamma\left(K + i\rho_0 v\hbar\beta\right)\right|^2}{\Gamma(2K)}. \tag{3.30}$$

The finite temperature introduces an energy scale T and comparing this scale to the driving force $\hbar\rho_0 v$ we obtain two different regimes in the response function (3.30),

$$\Gamma = \begin{cases} \dfrac{2\pi^2 y^2}{\tau_c}\dfrac{\Gamma(K)^2}{\Gamma(2K)}\rho_0 v\tau_c\left(\dfrac{2\pi T\tau_c}{\hbar}\right)^{2K-2}, & \dfrac{\rho_0 v}{K} \ll \dfrac{T}{\hbar}, \\[2ex] \dfrac{\pi y^2}{\tau_c}\dfrac{1}{\Gamma(2K)}\left(2\pi\rho_0 v\tau_c\right)^{2K-1}, & \dfrac{\rho_0 v}{K} \gg \dfrac{T}{\hbar}. \end{cases} \tag{3.31}$$

At zero temperature the quantum nucleation is algebraic with an exponent $2K-1$, while a finite temperature and small driving forces lead to a linear quantum nucleation rate with an algebraic temperature dependence , see Fig. 3.3.

Finally, we calculate E_{PS}, the energy transferred to the superfluid by a single phase slip. We have previously noted that the quantity $H = \int dx\mathcal{H}$ is conserved

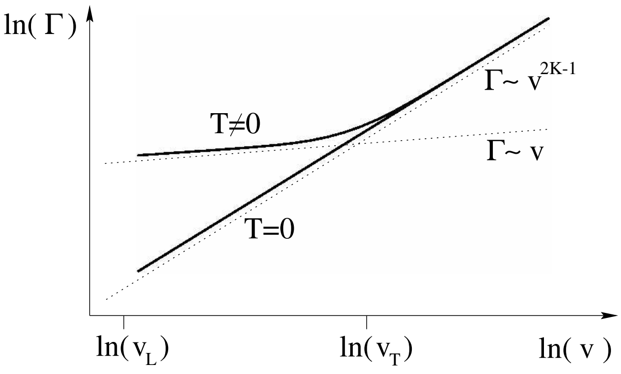

Figure 3.3: Quantum nucleation rate of phase slips: while for low temperatures $T/\hbar \ll \rho_0 v/K$ the nucleation rate is algebraic $\Gamma \sim v^{2K-1}$, a linear regime appears at high temperatures $T/\hbar \ll \rho_0 v/K$ with a crossover to an algebraic regime at the velocity $v_T = \pi T/mc_s$.

under time evolution. This integral of motion differs from the energy of the interacting Bose system only by the driving term and we obtain

$$E_{\rm PS} = \left[iv\hbar \int dx \overline{\psi} \partial_x \psi \right]_{\tau=0} = 2\pi\hbar\rho_0 v. \tag{3.32}$$

Note, that this energy coincides with the gain in potential energy $E_J(1-\cos\varphi) - \hbar\rho_0 v\varphi$ by a transition from $\varphi \to \varphi + 2\pi$. Then, the tunneling appears from one potential minimum to its neighboring one and the gain in potential energy is dissipated via sound waves into the leads.

The quantum nucleation rate Γ and the energy transfer $E_{\rm PS}$ of single phase slip to the superfluid are sufficient to calculate the total energy transfer to the superfluid via Eq. (3.2). Note, that a phase slip also leads to a finite chemical potential difference $\Delta\mu = 2\pi\hbar\Gamma$ between the superfluid on the left and the right side of the impurity. This relation can also be interpreted as an algebraic pressure-flow characteristic, in analogy to the nonlinear current-voltage response in charged superconductors [14].

3.5 Finite Geometries

For a finite system, the superfluid response strongly depends on the particular geometry. We consider two geometries: a ring and a finite tube. In both situations, the finite length L of the systems enters the phase slip dynamics via the boundary conditions: in the ring geometry the superfluid phase is single valued implying periodic boundary conditions, while in a tube the superflow vanishes at the boundary providing Neumann boundary conditions. As a consequence, the response of the two systems behaves very different at low drives: while in the ring quantum fluctuations are quenched and the superfluid flow is restored, the quantum fluctuations reduce the phase coherence across the impurity in the tube and the ground state is determined by a fixed 'quasinumber' $\mathcal{N}$ giving rise to 'Bloch oscillations'. At higher drives, the response depends on the relation between the characteristic frequencies: quantization of the linear modes c_s/L due to the finite size, the finite temperature $c_s/\xi_T = T/\hbar$, finite drive $\rho_0 v/K$ of the moving impurity, and the cut-off scale $1/\tau_c = c_s/\xi_c$.

3.5.1 Ring

We start with the superfluid ring containing a moving impurity (see Fig. 3.1(b)). This setup is characterized by periodic boundary conditions for the condensate wave function, i.e., $\psi(x,\tau) = \psi(x+L,\tau)$, leading to a quantization of the velocity of the superfluid in units of $2v_L = 2\pi\hbar/Lm = 2Kc_s/\rho_0 L$ and allows for the definition of a winding number k (see below). Integrating out the leads (see Section 3.3.2) replaces the Caldeira-Leggett damping kernel $K|\omega|$ in the effective action (3.21) by

$$Q(\omega) = K\omega \coth\frac{\omega L}{2c_s} = \begin{cases} 2Kc_s/L, & \omega < 2c_s/L, \\ \\ K|\omega|, & \omega > 2c_s/L. \end{cases} \tag{3.33}$$

Two effects modify the kernel: first, the existence of a winding number defines an extended quantum variable φ. Second, the compactness of the loop induces a self-interaction resulting in an additional static potential $(\hbar K c_s/2\pi L)\varphi^2$ which quenches the low frequency quantum fluctuations in the phase φ. Then the effective potential takes the form

$$V(\varphi) = E_J\left[1-\cos\varphi\right] + \frac{E_R}{2}\varphi^2 - \hbar\rho_0 v\varphi \tag{3.34}$$

with $E_R = \hbar\rho_0 v_L/\pi$. This static potential $E_R\varphi^2/2$ describes the kinetic energy of the flow in the ring and removes the degeneracy of the minima characterizing the undriven ($v = 0$) infinite ($L = \infty$) system, see Fig. 3.4. The minima φ_k of (3.34) are characterized by the winding number $k \in \mathbf{Z}$ with $\varphi_k \in [2\pi(k-1/2), 2\pi(k+$

1/2)). The precise values of the phases φ_k follow from minimizing (3.34) and satisfy

$$v_{\mathrm{rel}} = v_c \sin\varphi_k = v - \frac{v_L}{\pi}\varphi_k, \tag{3.35}$$

where the first term is the flow induced by the motion of the impurity, while the second term describes the flow of the superfluid in the leads. The relative velocity v_{rel} between the impurity and the superfluid is determined by the Josephson relation $v_{\mathrm{rel}} = v_c \sin\varphi$. In analogy with the infinitely long system the winding number k allows to distinguish two states of the phase with $\varphi_1 - \varphi_2 \in 2\pi\mathbf{Z}$ and the phase is an extended variable $\varphi \in \mathbf{R}$.

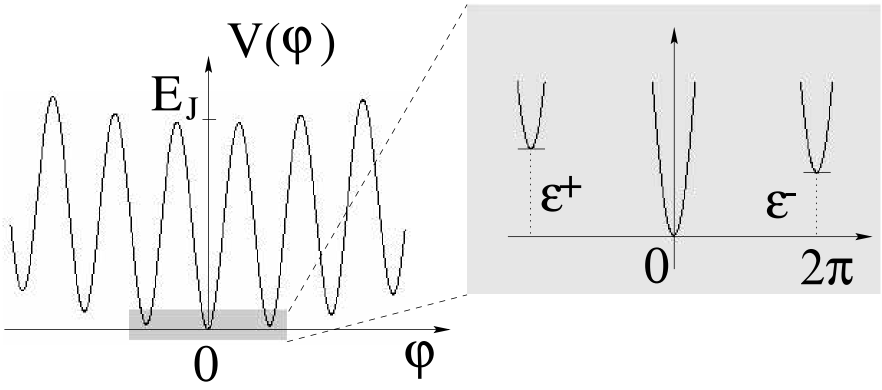

Figure 3.4: Effective potential $V(\varphi)$ in a ring: the additional quadratic term $E_R\varphi^2/2$ removes the degeneracy of the minima at zero drive. Shown here is the situation $v < v_L$ where the winding number $k = 0$ characterizes the absolute minimum. The neighboring minima are lifted in energy by $\epsilon^\pm = 2\pi^2 E_R \pm 2\pi\hbar\rho_0 v$.

The minimum φ_k with $|v - 2v_L k| < v_L$ is an absolute minimum describing a stable state. The properties of the system are then described by the appropriate density matrix for the equilibrium state. The response $X = \langle \partial_t \varphi \rangle$ to an applied driving force with $|v - 2v_L k| < v_L$ vanishes identically and is a thermodynamic quantity, while different velocities only describe different equilibrium states. The slowest time scale for equilibration is determined by transitions into nearby states $\varphi_{k\pm 1}$ due to thermal activated tunneling given by rates $\Gamma^\pm$. For $T = 0$, these rates vanish, while the rates $\Gamma^\pm$ at high temperatures $\xi_T < L$ are calculated below, see Eq. (3.39).

For short systems with $L < \xi_c$, the characteristic velocity v_L of the ring is larger than the critical velocity v_c of the impurity. Then there exists only one solution of equation (3.35) with the winding number determined by $|v-2v_Lk| < v_L$, and the system is always in a thermodynamic state. In the following, we restrict our considerations to large rings with $L > \xi_c$ and study the behavior at higher drives with $|v-2v_Lk| > v_L$. Then, the state φ_k is metastable. Transitions to the next minima $\varphi_{k\pm1}$ via quantum nucleation of phase slips with the rates $\Gamma^\pm$ (these rates will be calculated below) lead to an increase of the winding number k and drive the system towards equilibrium. In the case of strong drives $|v-2v_Lk| \gg v_L$, this equilibration shows a similar behavior of the phase as a finite response $X = \langle \partial_t \varphi \rangle = 2\pi(\Gamma^+ - \Gamma^-)$. Then we recover the physics of the infinitely long system.

On the other hand at moderate drives $v_L < |v-2v_Lk|$ the ring structure of the system is relevant and the rates $\Gamma^\pm$ describe the equilibration of the non-equilibrium state φ_k into the ground state. The quantum nucleation rates $\Gamma^\pm$ can be calculated via instanton techniques analogous to those used for the infinite wire. In the following we approximate $\varphi_k - \varphi_{k+1} \approx 2\pi$, and the relative velocity $v_{\text{rel}} \approx v - 2kv_L$.

At low temperatures, i.e., $\xi_T > L$, the real space periodic boundary conditions dominate over the imaginary time periodicity. The instanton expansion maps the system to charged particles with the interaction between a kink-antikink–pair determined by

$$\mathcal{S}/\hbar = K \ln\left[\left(\frac{L}{\pi c_s \tau_c}\right)^2 \sinh^2 \frac{\pi c_s \overline{\tau}}{L}\right] - 2\pi\rho_0 v_{\text{rel}} \overline{\tau}\,. \tag{3.36}$$

Comparing to the result in the infinite wire with periodic boundary conditions in imaginary time, Eq. (3.28), the low frequency cut-off $\hbar\beta$ is replaced by L/c_s and the *sine* goes over into the *hyperbolic sine*. At large distances $\overline{\tau} > L/c_s$, the first term in Eq. (3.36) describes a linear attraction and leads to the confinement of kink-antikink–pairs. For velocities $v_{\text{rel}} < v_L = \pi c_s \xi/L$ the linear repulsion due to the driving term is weaker than the attraction and no saddle point exists in (3.36); the quantum nucleation rate vanishes below the threshold velocity v_L in agreement with the above static analysis. On the other hand, high driving velocities $v_{\text{rel}} \gg v_L$ probe the short distance behavior of the interaction at the time scale $\overline{\tau} \sim K/\rho_0 v_{\text{rel}}$ where we recover the logarithmic attraction between a kink-antikink–pair. The quantum nucleation rate (3.29) with the interaction

(3.36) leads to

$$\Gamma^+ = \frac{\pi y^2}{\tau_c}\left(\frac{2\pi\xi_c}{L}\right)^{2K-1}\frac{1}{\Gamma(2K)}\frac{\Gamma\left[K\left(v_{\rm rel}/v_L+1\right)\right]}{\Gamma\left[1+K\left(v_{\rm rel}/v_L-1\right)\right]}. \tag{3.37}$$

Note that the rate Γ^+ denotes transitions to the state φ_{k+1} with lower energy, while the rate Γ^- describing transitions to the state φ_{k-1} with higher energy vanishes at $T = 0$ and is exponentially suppressed for finite temperatures $\Gamma^-/\Gamma^+ \sim \exp(-\xi_T/L)$. At high drives $v_{\rm rel}/v_L \gg 1$ the rate (3.37) reduces to the zero temperature result Eq. (3.31). At the threshold $v_{\rm rel} = v_L$ the nucleation rate is finite and becomes

$$\Gamma^+(v_L) = \frac{\pi y^2}{\tau_c}\left(\frac{2\pi\xi_c}{L}\right)^{2K-1}. \tag{3.38}$$

For lower drives, the nucleation is prohibited by energy conservation and only thermally activated tunneling is possible.

Turning to high temperatures, i.e., $\xi_T < L$, the Matsubara frequencies $\omega_s = 2\pi s/\hbar\beta$ with $s \in \mathbf{Z}$ probe the ohmic part $K|\omega|$ in the kernel (3.33) and the finite ring differs from the infinite system only by a static potential term for $s = 0$. Then the nucleation rate for a transition $\varphi_k \to \varphi_{k\pm1}$ is determined by a calculation similar to the one leading to (3.30) but with the driving force $\epsilon^\pm = \pm\hbar\rho_0 v$ renormalized by the additional term in the potential (3.34), i.e., $\epsilon^\pm = V(\varphi_{k\pm1}) - V(\varphi_k)$. The quantum nucleation rates become

$$\Gamma^\pm = \frac{y^2}{2\tau_c}\left(\frac{2\pi\tau_c}{\hbar\beta}\right)^{2K-1}\exp\left(\pi\beta\epsilon^\pm\right)\frac{\left|\Gamma\left(K+i\beta\epsilon^\pm\right)\right|^2}{\Gamma(2K)}. \tag{3.39}$$

For $v_{\rm rel} \gg v_L$, the driving term $\epsilon^\pm$ reduces to $\pm\hbar\rho_0 v$ and we recover the nucleation rates for the infinite system.

3.5.2 Tube

Next, we study a superfluid in a finite length tube and perturbed with a moving laser beam (see Fig. 3.1(c)). We approximate this setup by a circular tube of finite length L. The flow of the superfluid vanishes at the ends of the tube providing us with the boundary conditions $\partial_x\phi(-L/2,\tau) = \partial_x\phi(L/2,\tau) = 0$. The finite size produces a quantization of the modes in the leads which suppresses the spectral density and modifies the damping kernel $K|\omega|$ in (3.21) at low frequencies,

$$Q(\omega) = K\omega \tanh \frac{\omega L}{2c_s} = \begin{cases} K\dfrac{L}{2c_s}\,\omega^2, & \omega < 2c_s/L, \\ \\ K|\omega|, & \omega > 2c_s/L. \end{cases} \tag{3.40}$$

The low frequency action then reduces to that of a capacitively shunted Josephson junction,

$$\frac{\mathcal{S}}{\hbar} = \int d\tau \left\{ \frac{\hbar}{E_L}\frac{(\partial_\tau \varphi)^2}{2} + \frac{E_J}{\hbar}\left[1 - \cos\varphi\right] + \mathcal{L}_> \right\}, \tag{3.41}$$

with the 'charging' energy $E_L = 4\pi\hbar c_s/KL$. The additional term $\mathcal{L}_>$ accounts for high frequency contributions $\omega > 2c_s/L$ and includes kinetic and dissipative terms similar to (3.22). For long wires $L > \xi_c$ the mass term $(\hbar/E_C)\,\omega^2\varphi^2$ in $\mathcal{L}_>$ is small as compared to the charging term in (3.41), while such a term $\propto E_C^{-1}$ does not appear altogether in short wires with $L < \xi_c$.

The classical limit of the system describes a phase localized in one potential well characterizing a superfluid flow across the impurity. The dynamics of the phase φ follows from the real time Euler-Lagrange equation of the action (3.41). For short systems with $L < \xi_c$ the characteristic energy scale satisfies $\sqrt{E_J E_L}/\hbar = \sqrt{L/\xi_c}\,(2c_s/L) < 2c_s/L$ and we can neglect contributions from $\mathcal{L}_>$. Then the Euler-Lagrange equation takes the form

$$\frac{d^2}{dt^2}\varphi + \frac{E_J E_L}{\hbar^2}\sin\varphi = \frac{\rho_0 E_L}{\hbar} v. \tag{3.42}$$

This equation has been derived by Giovanazzi et al. [115] using a variational product Ansatz $\psi(x,t) = \psi(x)f(t)$ for the condensate wave functions in the leads. Such an adiabatic form describes a 'rigid' wave function and applies to the situation where the eigen-dynamics in the leads is quenched due to their small size $L < \xi_c$. On the other hand, for systems with $L > \xi_c$ excitations in the leads are important and give rise to dissipation via the radiation of sound waves producing an additional dissipative term $\propto \eta\, d\varphi/dt$ in (3.42).

Quantum fluctuations drastically change the classical behavior. Transitions through tunneling from one minimum of the potential $E_J\left[1 - \cos\varphi\right]$ to the next appear with a finite hopping amplitude W. For weakly interacting bosons with $E_J/E_L = K^2 L/4\pi^2\xi_c \gg 1$ a tight binding analysis is applicable: we denote by $|n\rangle$ the ground state for the phase φ with the potential $E_J\left[1 - \cos\varphi\right]$ replaced by its quadratic approximation $\sim E_J/2\ (\varphi - 2\pi n)^2$. The set $|n\rangle$ then describes localized phase states within the minima of the potential $E_J\,[1-\cos\varphi]$. In the tight binding approximation we neglect the influence of higher states and describe transitions from $|n\rangle$ to $|n\pm 1\rangle$ through the hopping amplitude W. The Hamiltonian for the action (3.41) then reduces to

$$\begin{aligned} H &= -\frac{W}{2}\sum_n \{|n\rangle\langle n+1| + |n+1\rangle\langle n|\} \\ &\qquad -2\pi\hbar\rho_0 v\sum_n n|n\rangle\langle n|, \end{aligned} \tag{3.43}$$

where the last term describes the driving force induced by the motion of the impurity (the operator φ takes the form $\varphi = 2\pi\sum_n n|n\rangle\langle n|$ in the site basis $|n\rangle$). This Hamiltonian is equivalent to that of an electron in a crystal driven by an electric field. At zero drive the energy eigenstates are arranged in a Bloch band, while a finite electric field leads to 'Bloch oscillations' [124]. Gauge invariance allows us to describe the electric force field $eE \cong \hbar\rho_0 v$ either by a static potential as in (3.43), or by a time dependent vector potential $eA/c = eEt \cong \rho_0 vt$ minimally coupled to the momentum. The corresponding unitary transformation

$$U = \exp\Big[-2\pi i\,(\rho_0 vt + \mathcal{N})\,n|n\rangle\langle n|\Big], \tag{3.44}$$

maps the Hamiltonian (3.43) to [124]

$$H = -\frac{W}{2}\sum_n \Big\{e^{2\pi\,i\,(\rho_0 vt+\mathcal{N})}|n\rangle\langle n+1| + e^{-2\pi\,i\,(\rho_0 vt+\mathcal{N})}|n+1\rangle\langle n|\Big\}. \tag{3.45}$$

The real number $\mathcal{N}$ is the 'quasinumber' and accounts for the gauge freedom. Its physical meaning will be discussed below.

The hopping amplitude W depends on the details of the damping term in $\mathcal{L}_>$. For systems where the characteristic frequency $\sqrt{E_J E_L}/\hbar$ is smaller than c_s/L, i.e., short tubes with $L < \xi_c$, we can drop $\mathcal{L}_>$ in determining the ground state properties of (3.41). The tunneling energy is determined within the instanton approximation and takes the form [107]

$$W \sim \frac{\hbar}{\tau_c}\frac{L}{\xi_c}\exp\left(-K\sqrt{L/\xi_c}\right). \tag{3.46}$$

For long tubes with $L > \xi_c$ the damping term in $\mathcal{L}_>$ is relevant, i.e., during the tunneling process involving the time scale τ_c the phase φ interacts with the sound waves in the leads resulting in a strong reduction of the tunnel energy as compared to the result (3.46). The instanton technique then provides us with a renormalized hopping amplitude [24]

$$W = \frac{\hbar y}{\tau_c}\left(\frac{\pi \xi_c}{2L}\right)^K, \tag{3.47}$$

which vanishes in the limit $L \to \infty$, in agreement with the results obtained for the infinite wire with ohmic dissipation.

Next, we have to discuss the compactness of the phase φ. At low temperatures and low driving forces the above hopping $\varphi \to \varphi \pm 2\pi$ takes place without exciting sound modes in the leads. We call such processes diagonal transitions. Then the two states φ and $\varphi + 2n\pi$ are indistinguishable, i.e., the phase φ is a compact variable defined on a circle $\varphi \in [0, 2\pi)$, (the states $|0\rangle$ and $|n\rangle$ are identical). Therefore the Hilbert space becomes one-dimensional and the Hamiltonian (3.45) simplifies to

$$H(t) = -W \cos\left[2\pi\left(\rho_0 v t + \mathcal{N}\right)\right] |0\rangle\langle 0|; \tag{3.48}$$

the state $|0\rangle$ evolves in time according to $|0\rangle(t) = \exp\left[-i\int dt H(t)\right]|0\rangle$.

At zero driving force, the tunneling of the phase implies that the phase coherence across the impurity, i.e., between the two superfluids on the left and right hand sides, is reduced. Then the 'quasi number' $\mathcal{N}$ on each side is fixed. Displacing the impurity by $\Delta L \ll L$ leads to a different particle density on the left and right side of the impurity, which is absorbed by the 'quasinumber' $\mathcal{N} = \rho_0 \Delta L$ introduced via the gauge freedom. The ground state energy takes the form

$$E(\mathcal{N}) = -W \cos(2\pi \mathcal{N}) \tag{3.49}$$

and describes a Bloch band in the 'quasinumber' $\mathcal{N}$, see Ref. [19] (the 'quasinumber' $\mathcal{N}$ then plays the role of the 'quasimomentum' k in a periodic crystal). Comparing to the classical Josephson effect, where a fixed phase Φ drives the supercurrent $j = j_c \sin\Phi$ through the Josephson junction, the fixed 'quasinumber' $\mathcal{N}$ drives the chemical potential difference $\Delta\mu = \partial_{\mathcal{N}} H(t) = 2\pi W \sin(2\pi\mathcal{N})$ between the two superfluids. Similarly, $\partial_t \Phi = \mu/\hbar \to \partial_t \mathcal{N}(t) = \rho_0 v$. At finite driving force $\rho_0 v$, the system exhibits 'Bloch oscillations' in the chemical potential $\Delta\mu = 2\pi W \sin\left[2\pi(\rho_0 v t + \mathcal{N})\right]$. These oscillations are due to the accumulation of particles in front of the impurity, the latter allowing only discrete particles to tunnel. Each 'Umklapp' process then describes a particle tunneling through the impurity.

Two mechanisms lead to the disappearance of ‘Bloch oscillations’: *First*, the tight binding approximation is not valid for driving forces $\rho_0 v$ or temperatures T larger than the band gap $\Delta = \sqrt{E_L E_J}$. Then transitions to higher bands, known as ‘Zener tunneling’ [125], become relevant for large drives and describe the accumulation of particles in front of the impurity, i.e., the absence of ‘Umklapp’ processes quenches the tunneling. The flow *across* the impurity then does not match the flow of particles *towards* the impurity, producing a steady increase in the chemical potential difference $\Delta\mu$. On the other hand for high temperatures $T > \Delta$ thermal fluctuations lead to transitions into higher bands and the tight binding analysis is not applicable. *Second*, the transitions $|n\rangle \rightarrow |n \pm 1\rangle$ can be divided in two classes: diagonal transitions without exciting sound modes in the leads leaving the phase compact at low temperature and low driving forces (see above), and nondiagonal transitions where the number of excited sound modes in the leads is changed and the initial and final state can be distinguished by counting the number of excited sound modes leading to a non-compact phase variable (the nomenclature is chosen in analogy to the physics of polarons [126]; the Hamiltonian (3.41) for the phase φ is equivalent to that of an electron in a periodic crystal coupled to a bath of harmonic oscillators). For processes involving frequencies larger than c_s/L, i.e., $\rho_0 v > c_s/L$ or $T/\hbar > c_s/L$ excitations of sound modes in the leads become relevant and the nondiagonal transitions compete with the diagonal transitions.

For short systems with $L < \xi_c$ the band gap is $\Delta = \sqrt{L/\xi_c}(2\hbar c_s/L) < 2\hbar c_s/L$, and the dominant mechanism for the disappearance of ‘Bloch oscillations’ are transitions into higher bands either due to large driving velocities $v > (2v_L/K)\sqrt{L/\xi_c}$ or high temperatures $T > T_L\sqrt{L/\xi_c}$ with $T_L = 2\hbar c_s/L$. On the other hand for long systems $L > \xi_c$, the presence of nondiagonal transitions is the relevant mechanism for the breakdown of the ‘Bloch oscillations’ and will be considered in the following in more detail.

At zero temperature but finite driving force v, the nondiagonal transitions become relevant for velocities $v > 2v_L/K$. Then we enter a complicated intermediate regime where the physics of Bloch states competes with finite scattering due to nondiagonal transitions. The situation simplifies for larger drives $v > 2v_L$: all processes are fast involving frequencies $\omega > c_s/L$ and the damping term in (3.41) dominates over the inertia — nondiagonal transitions dominate in this regime. We thus recover the physics of the infinitely long system: the transitions $|n\rangle \rightarrow |n| \pm 1\rangle$ are incoherent with a quantum nucleation rate determined by the instanton approach, and the states $|n\rangle$ and $|n \pm 1\rangle$ are distinguishable, i.e., the phase φ turn into an extended variable. If the velocity of the impurity is uniform during a phase slip process, i.e., $v\overline{\tau} = v_c\tau_c = \xi < R$ with R the amplitude of the laser oscillation, the instanton expansion with the damping kernel determined by Eq. (3.40) provides us with the interaction between a kink-antikink-pair

$$\mathcal{S}/\hbar = K \ln \left[\left(\frac{2L}{\pi c_s \tau_c} \right)^2 \tanh^2 \frac{\pi c_s \overline{\tau}}{2L} \right] - 2\pi \rho_0 v \overline{\tau} \,. \tag{3.50}$$

While at small distances the attraction is logarithmic, it vanishes at larger distances, i.e., the damping term in the action is suppressed and quantum fluctuations become stronger; the latter is the signature of the ground state with fixed ‘quasinumber’ $\mathcal{N}$. Large velocities $v > 2v_L$ of the driving impurity probe the logarithmic attraction via $\overline{\tau} \sim K/\rho_0 v < L/c_s$ and the quantum nucleation rate is determined by the result (3.30) for the infinitely long system.

On the other hand, at zero driving force $v = 0$ but finite temperature T the breakdown of ‘Bloch oscillations’ appears at the crossover temperature $T_L = 2\hbar c_s/L$. For $T < T_L$, corrections to the band width W due to the finite temperature are exponentially small $W(T) = W[1 - 4K \exp(-\pi\hbar c_s/LT)]$ at low temperatures [126], but strongly suppress the band width when approaching the crossover temperature. At high temperatures $T > T_L$ all processes are fast including the separation $\overline{\tau} = \hbar\beta/2$ between a kink-antikink pair, and we recover the physics of the infinitely long wire with the quantum nucleation rate determined by Eq. (3.30), the finite size of the system being irrelevant. A sketch of the boundaries in the $v - T$ diagram separating the Bloch type physics at small v, T from the intermediate and the incoherent tunneling regime is shown in Fig. 3.5.

3.6 Conclusions

The quantum nucleation of phase slips leads to a transfer of energy to the bosonic system at high drives $v > v_L$ but well below the mean field critical velocity $E_J/\hbar\rho_0$ of the impurity. Then the *macroscopic quantum tunneling* of the phase can be observed via the heating of the sample, in analogy to the experiment by Raman *et al.* [61] (note that our work predicts a dissipation-free low-drive response and the appearance of a critical velocity for both topologies, ring and tube). The quantum nucleation rate of phase slips vanishes exponentially in the dimensionless parameter K and, except for systems with small K, the time scale

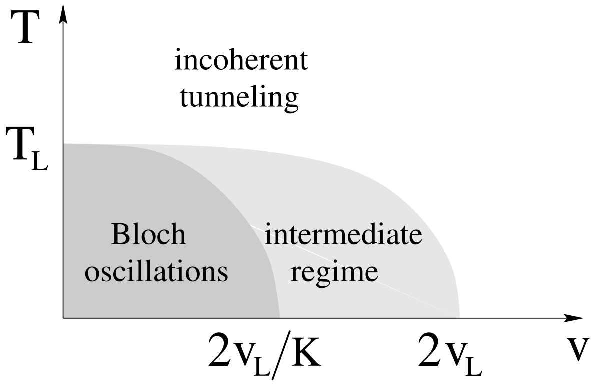

Figure 3.5: Response: for low driving forces $v < 2v_L/K$ and low temperatures $T < T_L$ the physics is determined by 'Bloch oscillations' with a band width W and a compact phase φ (dark region), while at high temperatures $T > T_L$ or high drives $v > 2v_L$ the response is characterized by incoherent tunneling with a rate Γ and an extended phase φ. For temperatures $T < T_L$ we have an intermediate regime for $2v_L/K < v < 2v_L$ where the 'Bloch oscillations' compete with the nondiagonal transitions (light region).

for the nucleation of a single phase slip can easily exceed the experimental time resulting in a superfluid behavior. On the other hand, the Bloch oscillations at low drives constitute a *macroscopic quantum coherence* phenomenon leading to density fluctuations within the leads. Using a second laser beam to probe the oscillating densities in the leads allows to measure these fluctuations, at least in principle. However, as each 'Umklapp' process involves only one particle tunneling through the impurity, these oscillations will be small, thus requiring a high sensitivity in the experiment.

In the following we will discuss the relevant parameters for trapped ^{87}Rb atoms. The system behaves one-dimensional if the energy scale for transverse excitations is larger than the energies driving the system, e.g., the driving force $\hbar\rho_0 v$ due to the motion of the impurity and the temperature T. The energy for transversal excitations is determined by the level spacing $\hbar\omega_\perp$ of the harmonic trap and provides us with the condition

$$T < \hbar\omega_\perp, \qquad \hbar\rho_0 v < \hbar\omega_\perp. \tag{3.51}$$

We start with Bose-Einstein condensates as described in the review by Dalfovo et al. [60] where the interaction is weak, i.e., $\overline{n}a^3 \ll 1$ with $\overline{n}$ the three dimensional density and a the scattering length of the bosons related to the interaction strength U via $U = 16\hbar^2 a/(mL_\perp^2)$ ($L_\perp$ is the transverse size of the system). Typical traps satisfy $L_\perp > \xi$ and the dimensionless parameter K measuring the relevance of quantum fluctuations can be written as

$$K = \frac{1}{8\sqrt{\pi}} \frac{1}{\sqrt{\overline{n}a^3}} \frac{L_\perp^2}{\xi^2}. \tag{3.52}$$

It follows that the condition of weakly interacting bosons $\overline{n}a^3 \ll 1$ leads to $K \gg 1$. Then quantum fluctuations are strongly suppressed and the system shows a superfluid response when driven with a moving impurity. These observation are in agreement with the estimation by Kagan et al. [119] where they obtained the stability of a superflow in a one dimensional ring for realistic parameters.

On the other hand new technologies [84] open up the possibility to fabricate traps with the transverse trapping frequency $\nu_\perp$ of the order $\nu_\perp \sim 10^5$ Hz and a length of the sample in the range $L_\parallel \sim 1$ mm. Then transversal excitations involve energies $E_\perp = 2\pi\hbar\nu_\perp \widehat{=} 5\ \mu$K. Here we give an example of the relevant parameters for ^{87}Rb atoms with a scattering length $a = 5.77$ nm.[60] We chose the one dimensional density $\rho_0^{-1} = 30$ nm and obtain the following parameters: transvere size of the trap $L_\perp = 24$ nm, healing length $\xi \sim L_\perp$, the dimensionless parameter $K = \pi\rho_0\xi = 2.6$, sound velocity $c_s = 31$ mm/s, and chemical potential $\mu \widehat{=} 5\ \mu$K. In this parameter range quantum fluctuations are relevant and the derivation of the effective action (3.22) is justified via the general approach presented in appendix D, where the mean field values for ξ, K, c_s are renormalized by fluctuations.

In conclusion, geometric confinement of the atom gas boosts the importance of fluctuations. The superfluid response strongly depends on the particular geometry: in a ring the phase difference across an impurity is well defined and the response remains superfluid below the critical velocity $v_L \propto 1/L$, while in a tube phase slips proliferate and driving the system induces ‘Bloch oscillations’ in the chemical potential across the impurity.

Chapter 4

Commensurate-Incommensurate Transition in Cold Atomic Gases

4.1 Introduction

Recently, subjecting an atomic Bose-Einstein condensate to an optical lattice, Greiner *et al.* [69] have succeeded in tuning the system through a quantum phase transition separating a superfluid (S) from a Mott insulating (MI) phase. The superfluid is phase coherent and exhibits a sound-like excitation spectrum. In addition, there are strong fluctuations in the occupation number at any particular lattice site [70]. In turn, the Mott-insulator is characterized by a density commensurate with the optical lattice, exhibits a gap in the excitation spectrum, and is incompressible. The 3D transition involves weakly interacting bosons and is well understood within the Bose-Hubbard description [47, 68]: the system turns insulating when the on-site interaction energy U becomes of the order of the hopping energy J. This strong coupling transition is a result of quenching the kinetic energy by a deep lattice potential.

Confining the atomic gas to one dimension (1D), the strong coupling limit can be reached *without* the optical lattice: in 1D, the ratio γ between the interaction- and kinetic energies per particle scales inversely with the density n and thus it is the *low*-density limit which is interacting strongly (Tonks gas) [74]. A new instability then appears in the strongly interacting 1D quantum gas at $\gamma \gg 1$: the superfluid ground state of the homogeneous system turns insulating in the presence of an arbitrarily weak optical lattice commensurate with the density of the bosons [127]. Here, the condition of a commensurate density means, that the optical lattice accommodates an integer number of atoms per site. The transition to the superfluid state then is exclusively triggered by changing the boson density away from the commensurate density, hence the S–MI transition turns into a transition of the incommensurate–commensurate type.

In this chapter, we analyze the superfluid to Mott insulator transition for bosons in 1D in the limit of weakly and strongly interacting gases. This goal is achieved by a mapping of the boson Hamiltonian to two classic problems. In the weakly interacting limit, we map the system to the Bose-Hubbard model [47, 128, 129, 130, 68], while in the strongly interacting limit, we map the boson Hamiltonian to the sine-Gordon model, which defines an exaclty solvable quantum field theory [131, 132, 133, 134, 135, 136, 137]. Below, we first summarize the main results providing us with the phase diagram, see Fig. 4.9. A weakly interacting atomic gas subject to an optical lattice is well described by the Bose-Hubbard model, which starts from a tight-binding model and takes the interaction between bosons into account perturbatively; the hopping amplitude $J(V)$ and the on-site interaction energy $U(V,\gamma)$ follow from the underlying parameters of the atomic gas, the dimensionless interaction parameter γ and the amplitude V of the optical lattice. The phase diagram of the Bose-Hubbard model is well known [47] and involves insulating Mott-lobes embedded in a superfluid phase, see Fig. 4.1. In 3D, the mean-field analysis for densities commensurate with the lattice provides the critical parameter $U/J|_{\mathrm{S-MI}} \approx 5.8\,z$, in good agreement with the experimental findings of Greiner *et al.* [69] (here, z denotes the number of nearest neighbors). Going to 1D, fluctuations become important and appreciably modify the mean-field result: numerical simulations [129, 130] place the transition at the critical value $U/J|_{\mathrm{S-MI}} = 2C \approx 3.84$. This result is easily transformed into the γ–V phase diagram of the weakly interacting atomic gas, once the relations $J(V)$ and $U(V,\gamma)$ to the Mott-Hubbard parameters are known.

Increasing the interaction strength γ, the critical amplitude V_c of the optical lattice triggering the S–MI transition decreases, see Fig. 4.9; the description of the atom gas in terms of the Bose-Hubbard model breaks down and we have to look for a new starting point. For a weak optical potential, a natural choice is the 1D Bose gas with δ-function interaction, which resides in the strong coupling regime at small densities n [74]; the presence of the optical lattice is taken into account perturbatively. The homogeneous 1D Bose gas with δ-function interaction has been solved exactly by Lieb and Liniger [72, 73]; the corresponding low-energy physics is properly described in terms of a Luttinger liquid with a parameter $K(\gamma)$

derived from the exact solution, see below. Adding the optical potential $\propto V$, we arrive at the sine-Gordon model; the critical value $K(\gamma, V) = 2(1 + V/4E_r)$ separating the Mott insulating phase from the superfluid one determines the phase line $V_c/E_r = (\gamma^{-1} - \gamma_c^{-1})/5.5$, with the critical value $\gamma_c \approx 3.5$. Combining the results of the Bose-Hubbard- and sine-Gordon models we can complete the phase diagram for the commensurable situation as shown in Fig. 4.9: most remarkable is the appearance of a critical interaction strength γ_c above which an arbitrary weak optical lattice is able to pin the system into a Mott insulator state. The presence of this instability is due to the closeness of the dilute 1D Bose liquid to Wigner-crystallization. Tuning the system away from commensurability with $Q \equiv 2\pi(n - 2/\lambda) \neq 0$ the Mott insulator survives up to a critical misfit $Q_c(V, \gamma)$. The corresponding physics is similar to that of the commensurate-incommensurate transition of adsorbates on a periodic substrate as studied by Pokrovsky and Talapov [138].

For a qualitative understanding of the transition in the strongly interacting 1D Bose gas, it is useful to consider the limit $\gamma \gg 1$, where the behavior is essentially that of an ideal Fermi gas [71]. A weak periodic potential $V(x) = V \sin^2(kx)$, with a lattice constant such that an integer number $i = 1, 2, \ldots$ of particles will fit into one unit cell, gives rise to a single-particle band structure in which the i lowest bands are completely filled. The ground state for noninteracting Fermions is then a trivial band insulator, separated from the excited states by an energy gap which scales like $(V/E_r)^i$ in the limit $V \ll E_r$. Similar to the Mott phase in the Bose-Hubbard model, the insulating state has a fixed integer density, commensurate with the lattice. It remains locked in a finite regime of the chemical potential, characterizing an incompressible state [47]. Clearly, for a weak periodic potential, the lowest energy gap with $i = 1$ is much larger than the higher-order ones. In this chapter, we will thus focus on the commensurate-incommensurate transition near integer filling $i = 1$, where the commensurate phase has maximal stability.

This chapter is organized as follows: In Sec. 4.2, we present the starting Hamiltonian accounting for a microscopic description of the bosons. Then, we study the weakly interacting limit in Sec. 4.3. We present the mapping to the Bose-Hubbard model and relate the model parameters U and J with the microscopic parameters γ and V. Knowledge of the phase diagram in the Bose-Hubbard model then allows to find the phase diagram in the microscopic parameters of the Bose gas. In Sec. 4.4 the mapping to the sine-Gordon model is introduced which represents a valid description of the boson hamiltonian for a weak optical lattice. The appearance of the new instability is discussed and the phase diagram is presented. Furthermore, the boson-fermion duality is presented in the limit $\gamma \rightarrow \infty$. These calculations assume a homogeneous situation; the influence of a trapping potential is presented in Sec. 4.5, where we discuss the resulting density profiles. Our results are summarized in Sec. 4.6, with a presentation of the combined phase diagram including the results from the weakly- and strongly interacting limits. We propose an experimentally realistic setup which allows for the detection of the Mott insulating phase in the strongly interacting limit under the influence of a weak optical lattice: the commensurate pinned state may be identified via its finite excitation gap, or alternatively, via the observation of the Bragg peaks in the static structure factor. The results presented in this chapter have been published in Ref. [127].

4.2 Boson Hamiltonian

We start from the microscopic description of the atomic gas. The interaction between the bosons is taken into account by the effective interaction $V(\mathbf{x}) = (4\pi a_s \hbar^2/m)\delta(\mathbf{x})$ [56] with a_s the scattering length. This pseudopotential approximation is valid in the dilute limit considered here. Then, the Hamiltonian becomes

$$H = \int d\mathbf{r} \left\{ \psi^+(\mathbf{r}) \left(-\frac{\hbar^2}{2m}\Delta + V(\mathbf{r}) \right) \psi(\mathbf{r}) + \frac{2\pi a_s \hbar^2}{m} \psi^+(\mathbf{r})\psi^+(\mathbf{r})\psi(\mathbf{r})\psi(\mathbf{r}) \right\} \quad (4.1)$$

with $\psi(\mathbf{r})$ the bosonic field operator and m the mass of the bosons. The external potential $V(\mathbf{r}) = V_{\text{trap}}(\mathbf{r}) + V_{\text{opt}}(\mathbf{r})$ accounts for a trapping potential and the optical lattice. The trapping potential is described by the harmonic potential $V_{\text{trap}}(\mathbf{r}) = (\omega_x x^2 + \omega_y y^2 + \omega_z z^2)/2$ with trapping frequencies $\omega_{x,y,z}$, while the periodic potential induced by a standing light wave with wave vector $k = 2\pi/\lambda$ takes the form $V_{\text{opt}}(\mathbf{r}) = V_x \sin^2(kx) + V_y \sin^2(ky) + V_z \sin^2(kz)$. The strength of the periodic lattice is proportional to the dynamic atomic polarizability times the laser intensity and is conveniently measured in terms of the recoil energy $E_r = \hbar^2 k^2/2m$. The fixed particle number provides an average particle density n in the trap center, which in turn is related to the chemical potential μ.

In the following, we are interested in a highly anisotropic periodic potential with $V_y = V_z \gg V_x = V$. The system consists of many parallel atom wires, where the hopping between different wires is quenched via to the large barrier of the optical lattice. In addition, transverse degrees of freedom in each wire are frozen if the transverse trapping frequency satisfies $\omega_\perp = \sqrt{4E_rV_z}/\hbar \gg \mu$. Each wire then establishes a one dimensional system and the Hamiltonian in a single wire takes the one-dimensional form

$$H = \int dx \left[\psi^+(x) \left(-\frac{\hbar^2}{2m}\Delta + V(x) \right) \psi(x) + \frac{g}{2}\, \psi^+(x)\psi^+(x)\psi(x)\psi(x) \right] \quad (4.2)$$

with $\psi(x)$ the bosonic field operator. The potential $V(x) = V\sin^2(kx) + \omega_x x^2/2$ accounts for the optical lattice with wave vector $k = 2\pi/\lambda$ and may also include a harmonic confining potential with trapping frequency ω_x. The strength g of the contact interaction is related to the 3D scattering length a_s and the transverse confining frequency $\omega_\perp = \sqrt{4E_rV_z}$ via $g = 2\hbar\omega_\perp a_s$ [75]. The strength of the interaction is conveniently expressed by the dimensionless parameter $\gamma = mg/\hbar^2 n$, which is the ratio between the interaction and the kinetic energy (here, n denotes the 1D density of the bosons). Note, that in 1D the strongly interacting limit with $\gamma \gg 1$ can be reached by decreasing the density. In this limit the system behaves like a gas of impenetrable bosons [71].

4.3 Weakly interacting bosons

4.3.1 Derivation of the Bose-Hubbard model

The energy eigenstates of the Hamiltonian (4.1) for a single atom in the homogeneous situation ($V_{\text{trap}} = 0$) are Bloch wave functions $u_{n,k}(x)$. Here, $k \in K$ denotes the Bloch wave vector with K the first Brioulline zone, while n characterizes the Bloch band. An appropriate superposition of Bloch states provides the Wannier functions $w_n(x - R)$,

$$w_n(x - R) = \int_K \frac{dk}{v_0}\, u_{n,k}(x) \exp(-ikR). \quad (4.3)$$

Here, v_0 denotes the volume of the first Brioulline zone K, while $R = j\lambda/2$ denotes the lattice vector of the site j with $\lambda/2$ the period of the opitcal lattice. The Wannier functions $w_n(x-R)$ form a complete set of orthogonal basis function, and offers an alternative description of a single particle in a periodic potential. As a consequence, the Bloch wave functions can be expressed in terms of the Wannier functions,

$$u_{n,k}(x) = \sum_R w_n(x - R) \exp(iRk). \quad (4.4)$$

Note, that the Wannier functions are localized functions, i.e., $w_n(x)$ vanish sufficiently fast for $|x| \to \infty$, and represent an ideal tool for discussing phenomena in which the spatial localization of states plays an important role.

Such a situation appears here, where the many body problem involves a contact interaction, see Eq. (4.1). We expand the bosonic field operator in terms of the Wannier functions $\psi^+(x) = \sum_{j,n} w_n(x - j\lambda/2) b^+_{j,n}$. The operator $b^+_{j,n}$ denotes the bosonic creation operator of the Wannier state $w_n(x - j\lambda/2)$, i.e., $b^+_{j,n}$ creates a localized state at the site j. The mapping to the Bose-Hubbard model then involves the following approximations: first, the analysis is reduced to the lowest vibrational modes with $n = 1$ and second, the hopping terms are restricted to nearest-neighbor hopping. These approximations can be justified for a strong optical lattice $V \gg E_r$ which quenches next-nearest neighbor hopping, and weak inter-particle interaction g. Then, the Hamilton (4.1) takes the Bose-Hubbard form ($b_j = b_{j,1}$)

$$H_{\text{BH}} = -J \sum_{\langle i,j \rangle} b_i^+ b_j + \frac{U}{2} \sum_i b_i^+ b_i^+ b_i b_i - \mu \sum_i b_i^+ b_i. \tag{4.5}$$

The summation $\langle i, j \rangle$ is restricted to nearest-neighbors. The last term accounts for a grand canonical description with fixed chemical potential μ. The hopping amplitude J and the interaction U derive from the Wannier functions

$$J = \int dx \, w_1^*(x) \left[-\frac{\hbar^2}{2m} \Delta + V_{\text{opt}} \right] w_1(x - \lambda/2), \tag{4.6}$$

$$U = g \int dx \, |w_1(x)|^4 . \tag{4.7}$$

A reliable estimate of the interaction strength is provided by approximating the Wannier function $w_1(\mathbf{r})$ by the wave function of the harmonic oscillator in each well. The oscillator frequency in each well is given by $\omega_{\text{well}} = \sqrt{4E_r V}/\hbar$, which implies the size of the localized wave function $a_{\text{well}} = \sqrt{\hbar/m\omega_{\text{well}}}$. The interaction strength U then becomes

$$U = \sqrt{2/\pi} \, \hbar\omega_\perp \frac{a_s}{a_{\text{well}}}. \tag{4.8}$$

Note, that the Wannier functions are expected to decay like $\sim \exp(-\text{const}|\mathbf{r}|)$, while the ground state wave function of the harmonic oscillator behaves as $\sim \exp(-|\mathbf{r}|^2/2a_{\text{well}}^2)$. These differences in the tail of the wave function define a minor correction in the interaction strength U; however, these tails are essential in determining the hopping amplitude J. Therefore, a different approach is necessary for an estimate of the hopping amplitude J. The condition of a strong optical lattice $V \gg E_r$ quenches next-nearest-neighbor hopping and the hopping amplitude J derives from the exactly known width of the lowest band in the 1D Mathieu equation [139],

$$4J = \frac{16}{\sqrt{\pi}} \sqrt{E_r V} \left(\frac{V}{E_r} \right)^{1/4} \exp \left(-2 \sqrt{\frac{V}{E_r}} \right). \tag{4.9}$$

The consistency in the derivation of the Bose-Hubbard model (4.1) requires a strong optical lattice $V \gg E_r$ which quenches next-nearest neighbor hopping. In addition the restriction to the lowest vibrational state in each well demands that the interaction energy U is small compared to the level separation $\hbar\omega_{\text{well}}$ of the states in each well

$$\frac{U n_{\text{site}}^2}{2} \ll \hbar\omega_{\text{well}} \tag{4.10}$$

with n_{site} the average particle number in each well. This condition ensures that the higher Bloch bands play a minor role in calculating the ground state properties. The strategy in the derivation of the Bose-Hubbard Hamiltonian is to treat the single particle problem in a periodic potential exactly, while the interaction between the particles is taken into account perturbatively.

4.3.2 Phase diagram for $\gamma \ll 1$

The phase diagram of the Bose-Hubbard model has been extensively studied in the past in any dimension [47, 128, 129, 130]. The system exhibits a quantum phase transition from a superfluid to a Mott insulator. The superfluid phase is characterized by phase coherence established by the formation of (quasi) off-diagonal long-range order and exhibits a sound like excitation spectrum. In addition, there are strong fluctuations in the particle occupation at any cite. This superfluid phase appears in the limit of weak on-site interaction $U \ll J$.

On the other hand, for vanishing hopping amplitude $J = 0$ each site is occupied by an integer number n_{site} of bosons which minimizes the on-site energy. Adding now a finite but small hopping $J \ll U$, the gain in kinetic energy is too small to overcome the potential barrier, and hopping is quenched. Then, the system exhibits insulating Mott lobes for $J \ll U$ embedded in a superfluid phase, see Fig. 4.1. This Mott insulating phase is characterized by the existence of an excitation gap for the creation of particle or hole excitations. The density n is fixed to the commensurable density $n = n_{\text{site}} 2/\lambda$ with $n_{\text{site}} \in \mathbf{N}$, and the compressibility $\partial_\mu n$ vanishes everywhere. At incommensurate densities with

$n_{\text{site}} \notin \mathbf{N}$, the system remains always in its superfluid phase as the extra particles can hop across the lattice.

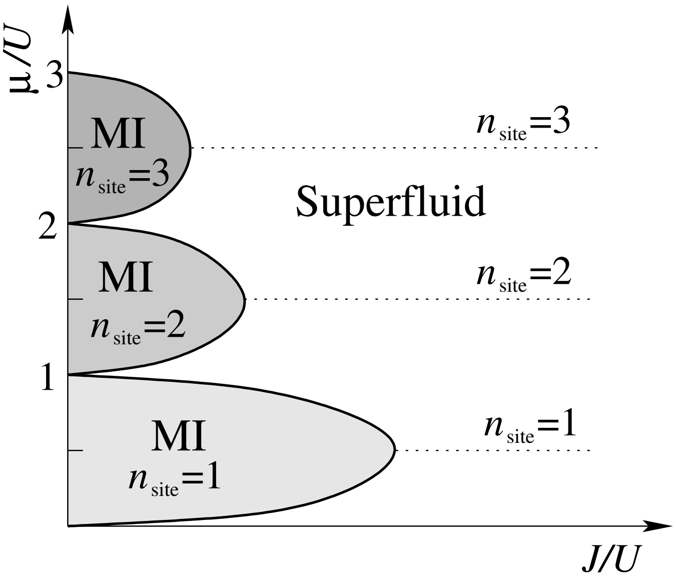

Figure 4.1: Sketch of the phase diagram for the Bose-Hubbard model. For small J/U the system exhibits insulating Mott lobes with integer filling $n_{\text{site}} = 1, 2, \ldots$ embedded in a superfluid phase. The dotted lines denote the contours of constant filling with $n_{\text{site}} = 1, 2, 3$.

At fixed commensurate density $n = n_{\text{site}} 2/\lambda$ with $n_{\text{site}} \in \mathbf{N}$ the transition from the superfluid to the Mott insulating phase appears at a critical value $U/J|_{\text{S-MI}}$. A mean field analysis [128] provides the critical value $U/J|_{\text{S-MI}} = z(n_{\text{site}} + \sqrt{n_{\text{site}} + 1})^2$ with z the number of nearest-neighbors. However, in low dimensional systems with $z = 2$ as considered here, fluctuations play an important role. The critical point is shifted to weaker interaction between the bosons, and a numerical calculation for $n_{\text{site}} = 1$ provides the critical value $U/J|_{\text{S-MI}} = 2C \approx 3.85$ [129, 130].

Going back to the starting Hamiltonian (4.2), we are interested in the phase diagram expressed in the experimentally accessible parameters: the strength of the optical lattice V, the dimensionless interaction parameter γ, and the density n. Then, the above results of the phase diagram for the Bose-Hubbard model allow to trace out the γ-V-n phase diagram of the original problem. Using the critical value $U/J|_{\text{S-MI}} = 2C$, and the above expressions for U (4.8) and J (4.9), the critical strength $V_c(\gamma)$ for commensurate density with $n_{\text{site}} = 1$ is obtained

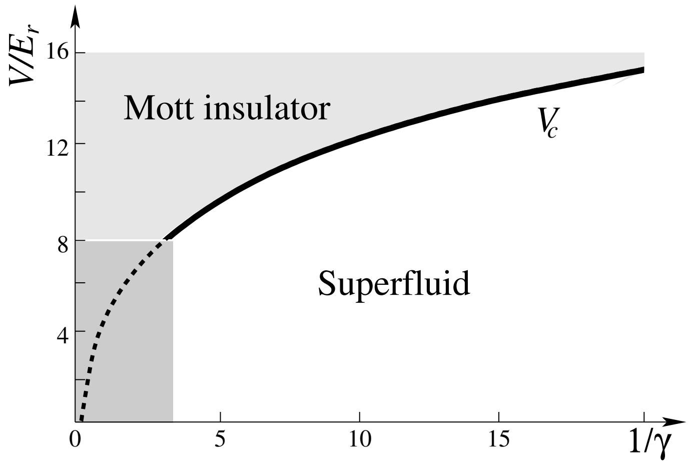

Figure 4.2: Phase diagram for large $V \gg E_r$ and small interactions $\gamma \ll 1$. In the dark region, the mapping to the Bose-Hubbard model breaks down, and a different approach in deriving the transition line is necessary.

from the implicit equation

$$4V/E_r = \ln^2[4\sqrt{2}\pi C\,(V/E_r)^{1/2}/\gamma]. \tag{4.11}$$

The γ-V phase diagram is shown in Fig. 4.2. Consistency of this derivation requires the validity of the mapping of the Hamiltonian (4.2) to the Bose-Hubbard model (4.5). As discussed in the derivation of the Bose-Hubbard model, the mapping is restricted to strong optical lattices $V \gg E_r$ and weak interaction U (see Eq. (4.10)); therefore Eq. (4.11) for the critical line $V_c(\gamma)$ in the γ-V phase diagram is applicable for $\gamma < 1$ and $V_c \gg E_r$.

4.4 Strongly interacting bosons

The critical line $V_c(\gamma)$ derived in the previous chapter decreases with increasing interaction γ. As a consequence, the mapping to the Bose-Hubbard model fails in the limit of strong interaction and a different approach in deriving the phase diagram γ-V-n is required. This alternative approach is obtained by mapping the starting Hamiltonian (4.2) to the sine-Gordon model.

4.4.1 Derivation of the sine-Gordon model

In the following, we focus on the limit of a weak optical lattice $V \ll E_r$. Then the above description of the atomic gas in terms of the Bose-Hubbard model breaks down, since the atoms now occupy several vibrational states in each well. In the limit where the optical lattice is only a small perturbation, the natural choice is to start from a hydrodynamic description of the homogeneous system (4.1). In this hydrodynamic approach, one expresses the bosonic field operator $\psi(x)$ in terms of the long-wavelength density- and phase- fields θ and ϕ [100],

$$\psi(x) \sim \sqrt{n + \partial_x \theta/\pi}\, \exp(i\phi). \tag{4.12}$$

These long-wavelength density and phase fields obey the standard commutation relation $[\phi(x), \partial_y \theta(y)] = i\pi\delta(x-y)$. The density operator $n(x)$ in this hydrodynamic approach is smeared over length scales $a \sim 1/\pi n$, and takes the form $n(x) \sim n + \partial_x\theta/\pi$. In the absence of an external potential $V(x)$, the Hamiltonian (4.1) reduces to the low energy quadratic form [100]

$$H_0 = \frac{\hbar}{2\pi} \int dx \left[v_J (\partial_x \phi)^2 + v_N (\partial_x \theta)^2 \right]. \tag{4.13}$$

Here, the first term accounts for the kinetic energy of the bosons with $v_J = \pi\hbar n/m$, while the second term derives from the interaction energy with $v_N = \partial_n \mu/\pi\hbar$ determined by the inverse compressibility. The sound velocity $v_s = \sqrt{v_J v_N}$ is consistent with the standard thermodynamic relation $m v_s^2 = n\partial_n\mu$. The Hamiltonian (4.13) with its linear spectrum $\omega = v_s k$ is valid only below a momentum cutoff $1/a \sim \pi n$ [72, 73]; the choice of the length scale a fixes the energy scale of H_0. The dimensionless parameter $K = \sqrt{v_J/v_N}$ determines the quasi off-diagonal long-range order of the bosonic field operator $\langle \psi^+(x)\psi(x')\rangle \sim |x-x'|^{-1/2K}$ for $|x-x'| \to \infty$. This quasi long-ranger order is sufficient to provide a superfluid response and the Hamiltonian (4.13) describes bosonic particles with a superfluid ground state at zero temperature. The effect of interactions arising from scales smaller than a is properly accounted for by a renormalization of the inverse compressibility $\partial_n\mu(\gamma)$ [100]. Note, that the stiffness v_J remains unrenormalized under high energy fluctuations due to the Galilei invariance of the homogeneous system. The renormalization flow of the inverse compressibility for a general interaction between the bosons is unknown. However, in the situation considered here with a contact interaction, the renormalized compressibility derives from the exact solution of the Hamiltonian (4.1) in the absence of a periodic potential by Lieb and Liniger [72]. The dimensionless parameter K is a monotonically decreasing function of γ. The limiting behavior of $K(\gamma)$ take the form

$$K(\gamma) = \begin{cases} \pi \left[\gamma - \dfrac{1}{2\pi}\gamma^{3/2}\right]^{-1/2}, & \gamma \ll 10, \\ \\ \left(1 + \dfrac{2}{\gamma}\right)^{2}, & \gamma \gg 10. \end{cases} \tag{4.14}$$

The first equation follows from the Bogoliubov approximation in 1D. Surprisingly, this result remains quantitatively correct for γ values up to 10 [72]. The second equation derives from the exact solution in the limit $\gamma \to \infty$. The relation $K(\gamma)$ is shown in Fig. 4.3 with the two limiting asymptotics.

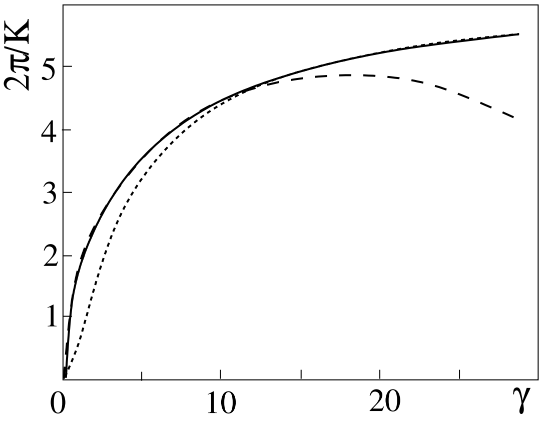

Figure 4.3: Relation between K and γ: the solid line is the numerical solution to the exact Bethe ansatz equation [72]. The dashed line represents the Bogoliubov approximation, which is is a good approximation for $\gamma < 10$, while the dotted line is the asymptotic solution for $\gamma \to \infty$, and represents a good approximation for $\gamma > 10$.

Adding now an optical lattice, it is necessary to go beyond the hydrodynamic approximation. The operator $\Theta(x) = \theta(x) + \pi n x$ increases monotonically by π each time x passes the location of a particle. Then a representation of the density operator $n(x)$ reflecting the discrete nature of the particle can be constructed from [100]

$$n(x) = \left[n + \frac{1}{\pi}\partial_x \theta(x)\right]\left\{\sum_s \delta\left[\frac{1}{\pi}\Theta(x) - s\right]\right\}, \tag{4.15}$$

or equivalently,

$$n(x) = \left[n + \frac{1}{\pi}\partial_x\theta\right]\left\{1 + 2\sum_{s=1}^{\infty}\cos\left[2s\,\theta(x) + 2\pi\,s\,nx\right]\right\}. \tag{4.16}$$

The first term describes the smeared density operator $n(x)$ in the long-wavelength approximation, while the second term accounts for the discrete nature of the particles. The periodic potential $V_{\text{opt}}(x)$ in Eq. (4.1) gives rise to the perturbation

$$H_{\text{V}} = \frac{V}{2}\int dx\, n(x)\cos\frac{4\pi x}{\lambda}. \tag{4.17}$$

Inserting the Fourier expansion (4.16) in (4.17) generates terms of the type appearing in the quantum (1+1)-dimensional sine-Gordon theory [131, 135]. In the following, we consider particle densities $n \approx 2/\lambda$ close to commensurability, i.e., about one boson per unit cell of the periodic lattice. We define the parameter $Q = 2\pi(n - 2/\lambda)$, which represents a suitable measure of the deviation from the commensurability condition $n = 2/\lambda$. Averaging over length scales smaller than $a \sim 1/\pi n$ and keeping the dominant term arising from the lowest harmonic in (4.16) with $s = 1$, the perturbation has the conventional sine-Gordon form [100, 47]

$$H_{\text{V}} = \frac{V\,n}{2}\int dx\,\cos\left[2\theta + Qx\right]. \tag{4.18}$$

The strength of the nonlinear $\cos 2\theta$- perturbation is conveniently expressed through the dimensionless parameter $u = \pi a^2 nV/2\hbar v_s$ which naturally involves the cutoff parameter a [136]. The twist Q vanishes at commensurability; away from commensurability, the finite twist Q is preferably incorporated into the free Hamiltonian (4.13) via the replacement $\partial_x\theta \to \partial_x\theta - Q/2$ and acts as a shift $\delta\mu = \hbar v_s Q/(2K)$ in the chemical potential for excitations.

The Hamiltonian $H_0 + H_{\text{V}}$ takes the form of the $(1+1)$-dimensional quantum sine-Gordon model and is the proper low-energy description of the Hamiltonian (4.1) for a weak optical lattice $u \ll 1$,

$$H = \frac{\hbar v_s}{\pi}\int dx\left\{\frac{1}{2}\left[K(\partial_x\phi)^2 + \frac{1}{K}(\partial_x\theta)^2\right] - \frac{Q}{2K}\,\partial_x\theta + \frac{u}{a^2}\cos\left(2\theta\right)\right\}. \tag{4.19}$$

The quantum sine-Gordon model has been discussed in the context of the commensurate-incommensurate transition of adsorbates on a periodic substrate [138, 140, 141]. It defines an exactly solvable quantum field theory and has been extensively studied in the past [131, 132, 133, 134, 135, 136, 137]. In the following, we make use of the results pertinent to the description of the phase diagram.

Note, that the quantum sine-Gordon model is equivalent to other exactly solvable theories such as the U(1)-Thirring model or the massive Thirring model [134]. These equivalences allow to interpret our bosonic theory in terms of interacting electrons. This equivalence between strongly interacting bosons and fermions in 1D was already noted by Girardeau [71]. Starting from the Hamiltonian (4.2) with $g \to \infty$, one can show that the ground state wave function of the bosons in a arbitrary potential coincides with the ground state wave function of non-interacting fermions up to an antisymmetric prefactor. The equivalence allows to deduce ground state properties of the bose system from the corresponding fermionic system. This equivalence between bosons and fermions is also conserved in the sine-Gordon model. At the special point $K = 1$, the sine-Gordon model maps to a system of massive free fermions.

4.4.2 Phase diagram for $\gamma \gg 1$

We start with the evolution of the system with changing interaction γ at commensurate density $Q = 0$ and keep the potential V fixed. A perturbative calculation (see Ref. [135] for a review) shows that the weak optical lattice described by H_{V} is irrelevant for $K > K_c = 2$ and hence is unable to pin the bosons. The ground-state properties then are determined by H_0 alone and the bosons exhibit quasi off-diagonal long-range order and remain superfluid with a linear excitation spectrum. Using the relation $K(\gamma)$ (see Eq. 4.14), the critical value $K_c = 2$ translates to $\gamma_c \approx 3.5$ in the γ-V phase diagram. In the strong coupling regime $K < K_c$, the perturbation H_{V} is relevant, and the atoms are locked to the lattice even for an arbitrary weak potential strength V. In this Mott insulating state, the excitation spectrum takes the form $E_q = \sqrt{(\hbar v_s q)^2 + \Delta^2}$ with a characteristic excitation gap Δ.

The dependence of the excitation gap Δ on the amplitude u of the optical lattice and the interaction K can be obtained from a recent nonperturbative renormalization group analysis of the quantum sine-Gordon model by Kehrein [136, 137]. For small values u and K away from $K_c = 2$ one finds (see Fig. 4.4)

$$\Delta = \frac{\hbar v_s}{2a}\left(\frac{u}{2-K}\right)^{1/(2-K)}, \tag{4.20}$$

while for K approaching $K_c = 2$ the gap vanishes exponentially

$$\Delta = \frac{\hbar v_s}{2a}\exp\left(-\frac{1}{2-K}\right). \tag{4.21}$$

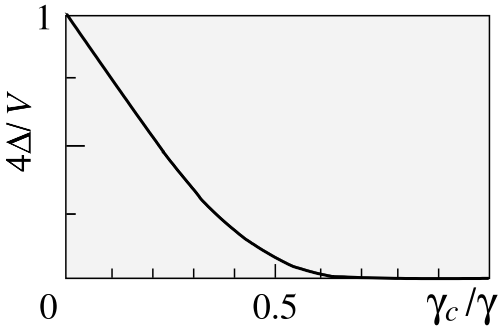

Figure 4.4: The size of the excitation gap Δ versus interaction strength γ for a fixed amplitude $V = E_r/2$. For $\gamma \to \infty$ the excitation gap assumes the free fermion limit $V/4$, while it vanishes exponentially for $\gamma \to \gamma_c$ with $\gamma_c \approx 3.5$.

In the strong coupling limit $K \to 1$ the gap reduces to the simple form $\Delta \to \hbar v_s u/2a$. Then the opening of the gap can easily be understood by exploiting the equivalence between strongly interacting bosons and free spinless fermions in 1D [71]. Free fermions in a periodic lattice with commensurate filling, i.e., one particle per unit cell, form a band insulator with a single particle band gap $2\Delta = V/2$ at the Fermi energy. Comparing this result with the above expression $2\Delta(K = 1) = \hbar v_s u/a$ fixes the cutoff at the value $1/a = \pi n$ at $K = 1$ and we obtain $u = KV/4E_r$. In the following, we ignore small corrections arising due to a possible modification in the cutoff away from $K = 1$. The expression (4.20) for the gap Δ then takes the form

$$\Delta = \frac{E_r}{K}\left[\frac{KV}{(2-K)4E_r}\right]^{1/(2-K)}. \tag{4.22}$$

From the equivalence of the Bose system with free fermions at $K = 1$, it follows that the single particle excitations obey Fermi statistics. This is a consequence of the strong interaction between the bosons. This property on the statistics of excitations is conserved in the Mott insulating phase away from $K = 1$. In addition, these interacting single particle excitations involve $1/K$ bosons [134].

The behavior of the phase transition line near the critical point $K_c = 2$ derives from a renormalization group analysis in second order perturbation theory in u. The renormalization group equations for K and u take the form [133, 137]

$$\frac{d(K^{-1})}{d\ln\Lambda} = -u^2, \qquad \frac{du}{\ln\Lambda} = (K-2)\,u \tag{4.23}$$

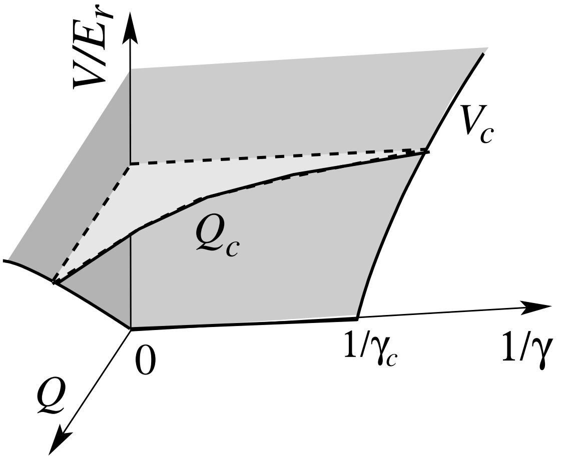

Figure 4.5: Schematic phase diagram illustrating the superfluid and Mott insulating (shaded region) phases versus parameters γ (interaction), V (optical potential), and Q (commensuration). Above the critical interaction strength $\gamma > \gamma_c$ an arbitrary weak commensurate optical lattice pins the bosons. For fixed interaction γ the transition is of the commensurate-incommensurate type, where the Mott insulating phase is stabilized for $Q < Q_c$.

with $\ln \Lambda$ the scaling parameter. Close to the critical point $K_c = 2$ these equations reduce to the standard Kosterlitz-Thouless scaling equations with the critical transition line

$$K_c(u) = 2\,(1 + u)\,. \tag{4.24}$$

Combining this result with (4.14), it is straightforward to determine the line $V_c(\gamma) \approx E_r(\gamma^{-1} - \gamma_c^{-1})/5.5$ in the γ-V phase diagram, see Fig. 4.5.

Next, we turn away from commensurability and concentrate on the stability of the Mott-insulator at fixed V and $\gamma > \gamma_c(V)$, but with a finite twist $Q \neq 0$. Then, for an arbitrary weak potential V, the transition is of the commensurate-incommensurate type as studied by Pokrovsky and Talapov [138]. The quantum sine-Gordon model describes the competition between the preferred average interparticle distance $1/n$ at given density due to the repulsive interaction and the period $\lambda/2$ imposed by the external potential. The atoms remain locked to the weak periodic potential as long as the shift $\delta\mu$ in the chemical potential induced by the twist Q remains smaller than the single-particle energy $K\Delta$ necessary for the addition of a boson; note that the above solitonic excitations involve $1/K$ bosons [134] and therefore the required energy for an additional boson is $K\Delta$.

This condition then translates into the critical twist

$$Q_c(\gamma, V) = 2K^2\Delta/\hbar v_s. \tag{4.25}$$

Beyond Q_c the system develops a finite density of excitations, which interpolate between minima of the external potential, thus relieving the frustration present at incommensurate densities $Q \neq 0$.

Combining the results from the Bose-Hubbard model and the sine-Gordon model allows to sketch the phase transition line separating the superfluid from the Mott insulating phase for all interactions γ. In Fig. 4.9 we plot the exact transition line in the two limits of small and large γ in the γ-V phase diagram.

4.5 Influence of a trapping potential

In order to analyze the consequences of the commensurate-incommensurate transition for cold atoms in a trap, we consider a 1D Bose gas in the presence of a weak longitudinal confining potential $V_{\text{trap}}(x) = m\omega_x^2 x^2/2$. We focus on the limit of a large trap with an associated oscillator length $l = (\hbar/m\omega_x)^{1/2}$ much larger than the inter-particle distance $1/n$. In this inhomogeneous situation, the density profile $n(x)$ may be obtained from the local density approximation [60, 76]

$$\mu\,[n(x)] + V_{\text{trap}}(x) = \mu[n(0)]. \tag{4.26}$$

Here, $\mu[n]$ denotes the relation between the chemical potential and the density of the homogenous system. The local density approximation assumes that at every position the system is in thermodynamic equilibrium and becomes exact in the thermodynamic limit of large particle number $N \to \infty$ and smooth trap potential with $\omega \to 0$. The central density $n(0)$ and the associated radius $R = (2\mu[n(0)]/m\omega_x^2)^{1/2}$ of the atomic cloud are determined by the normalization condition

$$N = \int_{-R}^{R} dx\, n(x) = 2R \int_0^{n(0)} dn \sqrt{1 - \frac{\mu[n]}{\mu[n(0)]}}. \tag{4.27}$$

In the absence of an optical lattice the density profile is a smooth function of the coupling γ. In the weak coupling limit $\gamma \to 0$, the chemical potential takes the mean field value $\mu = ng$ and the density profile reduces to the Thomas Fermi result

$$n(x) = \left(\frac{9N^2\hbar^2}{32mgl^4}\right)^{1/3} \left[1 - \frac{x^2}{R_{\text{TF}}^2}\right] \tag{4.28}$$

with $R_{\mathrm{TF}} = \left(3\hbar^2/2Nmgl\right)^{1/3} l$. In the opposite Tonks gas limit $\gamma \gg 1$, $\mu[n] \to \mu_{\mathrm{F}}[n] = (\hbar\pi n)^2/2m$ approaches the expression for the Fermi energy of an ideal Fermi gas with density n [76], resulting in the profile

$$n(x) = \frac{2N}{\pi R_{\mathrm{F}}}\sqrt{1-\left(\frac{x}{R_{\mathrm{F}}}\right)^2}. \tag{4.29}$$

Here, the radius of the atomic cloud is $R_{\mathrm{F}} = (2N)^{1/2} l$. Note, that the density profile approaches that of free fermions with a leading term independent on the interaction γ. This is again a consequence of the equivalence between strongly interacting bosons and free fermions.

Next we add an optical lattice and focus on the behavior of the density profile in the strong coupling limit $\gamma < \gamma_c$. Then the chemical potential $\mu[n]$ as a function of density n jumps by $\Delta\mu = 2K\Delta$ at the commensurate density $n = 2/\lambda$. This jump in the chemical potential is a consequence of the single-particle excitation gap in the Mott insulating phase and describes an incompressible state with vanishing compressibility $\partial_\mu n = 0$. Exploiting again the equivalence between strongly interacting bosons and free fermions, the chemical potential $\mu[n]$ is known explicitly at $K = 1$,

$$\mu[n] = \mu_{\mathrm{F}}[n] + \frac{\Delta\mu}{2} f\left(\frac{4KE_r}{\Delta\mu}\frac{\delta n}{n_c}\right) \tag{4.30}$$

with $\delta n = n - n_c$ ($n_c = 2/\lambda$) and

$$f(z) = \pm\left(1+z^2\right)^{1/2} - z. \tag{4.31}$$

Ignoring the residual interaction between the single-particle excitations appearing for $K > 1$, the expression (4.31) remains a valid approximation in the relevant regime $1 < K < 2$ [136].

Using this approximation, the density profiles are obtained from a integration of Eq. (4.27). The density profiles for different filling factors are shown in Fig. 4.6; we introduce the parameter $\alpha = K\Delta/2E_r$ measuring the single particle excitation gap. For a density in the trap center close to the commensurate density $n = 2/\lambda$, an incompressible Mott insulating regime appears with a flat density profile, surrounded by a superfluid region. The solid gray line in Fig. 4.6 shows the density profile in the absence of a periodic potential with chemical potential μ_0, while the dashed line is the resulting density profile with the same number of particles N as the optical lattice is turned on. Note, that chemical potential

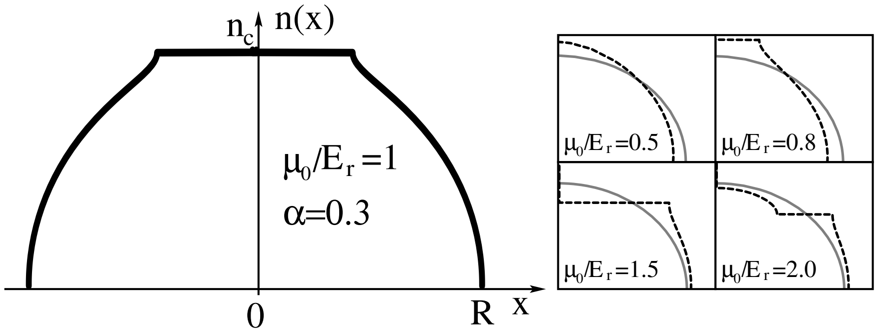

Figure 4.6: Density profiles for fixed $\alpha = 0.3$: the solid gray line denotes the density profile in the absence of a periodic potential for different chemical potentials $\mu_0/E_r = 0.5, 0.8, 1.0, 1.5, 2.0$, while the dashed line is the resulting density profile with the same number of particles N as the optical lattice is turned on. The Mott insulating regimes are characterized by a constant density and are surrounded by superfluid regimes. The size of the gap is expresed via $\alpha = K\Delta/2E_r$. Note, that the formation of the Mott insulating phase changes the radius of the atomic cloud.

$\mu_0 = \hbar\omega_x N$ is a suitable parameter measuring the total number of particles for a fixed trapping frequency ω_x. The Mott insulating regimes are characterized by a constant density and are surrounded by superfluid regimes. It follows that due to the formation of a Mott insulating regime, the size of the atomic cloud is modified and the chemical potential is shifted by $\mu - \mu_0$. This modification of the radius is due to the attraction of particles from the boundary into the Mott insulating regime with fixed density $n = 2/\lambda$, or repulsion of particles from the trap center to the boundaries; these two scenarios are in competition with each other. Then, depending on the number of particles in the trap, the size of the atomic cloud can decrease or increase. Note, that the chemical potential and the radius of the atomic cloud are related via $R = (2\mu[n(0)]/m\omega^2)^{1/2}$. The shift in the chemical potential $\mu - \mu_0$ as a function of the gap $\alpha = K\Delta/2E_r$ and the chemical potential of the unperturbed system is shown in Fig. 4.7. In addition, the fraction ΔN of particles participating in the Mott insulating phase is shown in Fig. 4.8. This fraction plays an important role in the experimental detection of the Mott insulating phase.

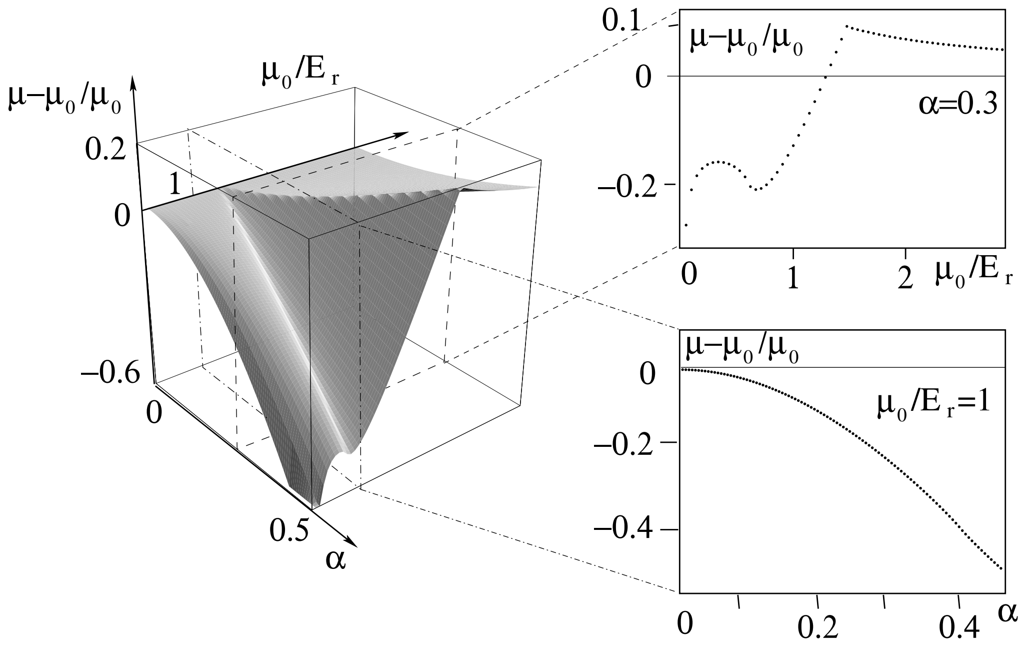

Figure 4.7: Variation of the chemical potential: switching on the periodic potential modifies the radius of the atomic cloud and shifts the chemical potential $\mu - \mu_0$. Depending on whether particles are attracted from the boundary into the Mott insulating phase, or repelled from the trap center to the boundary, the shift in the chemical potential is either negative, or positive.

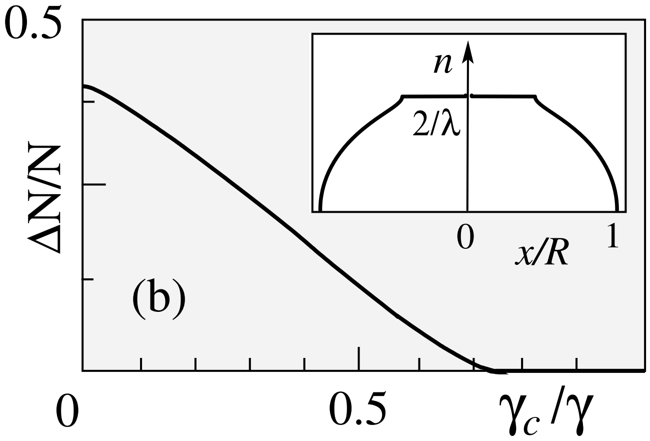

Figure 4.8: Fraction of particles ΔN participating in the Mott insulating state as a function of the interaction strength γ for fixed strength of the optical lattice $V = E_r/2$. The inset shows the density distribution $n(x)$ with the Mott phase characterized by a locked commensurate density in the trap center, surrounded by a superfluid region.

4.6 Discussion and conclusions

In this chapter, we have studied the superfluid to Mott insulator quantum phase transition of cold atoms in an optical lattice in a 1D system. The superfluid phase is characterized by phase coherence established by the formation of (quasi) off-diagonal long-range order and exhibits a sound like excitation spectrum. In turn, the Mott insulator exhibits an excitation gap for the creation of particle/hole excitations and the density n is commensurate with the optical lattice, implying that the compressibility $\partial_\mu n$ vanishes. For weak interactions $\gamma < 1$, a strong optical lattice with $V_c(\gamma) \gg E_r$ is required to drive the system into the Mott insulating state. Then, the Hamiltonian for interacting bosons can be mapped to the Bose-Hubbard model, and the properties of the superfluid to Mott insulator phase transition derive from the corresponding transition in the Bose-Hubbard model. The transition line $V_c(\gamma)$ for commensurate density $n = 2/\lambda$ is shown in Fig. 4.9. In contrast, for strong interactions $\gamma > 1$, a weak optical lattice $V \ll E_r$ is sufficient to pin the bosons. Then, the system maps to the sine-Gordon model and the superfluid to Mott insulator transition can be studied in terms of the strong and weak coupling phases of the sine-Gordon model. The critical potential strength $V_c(\gamma)$ derived from the sine-Gordon model is again shown in Fig. 4.9.

The system exhibits an instability above the critical interaction strength $\gamma_c \approx 3.5$, where an arbitrary weak optical lattice is sufficient to drive the system into the Mott insulating phase. The exact results on the critical transition line $V_c(\gamma)$ at commensurability $n = 2/\lambda$ obtained in the weakly and strongly interacting limits, allow to sketch the complete phase diagram by interpolating between these two limits.

In addition, for any interaction strength γ the transition from the Mott insulating state to the superfluid state can also be achieved by driving the density of the bosons away from commensurability. Then, the transition is of the commensurate-incommensurate type, where the periodicity of the optical lattice and the preferred density of the bosons induce a frustration in the system. Above the critical twist Q_c a finite density of excitations relieves this frustration. In contrast to the pinned bosons these excitations are free to move and set up a finite superfluid stiffness. A sketch of the phase diagram including the commensurate-incommensurate transition is shown in Fig. 4.5.

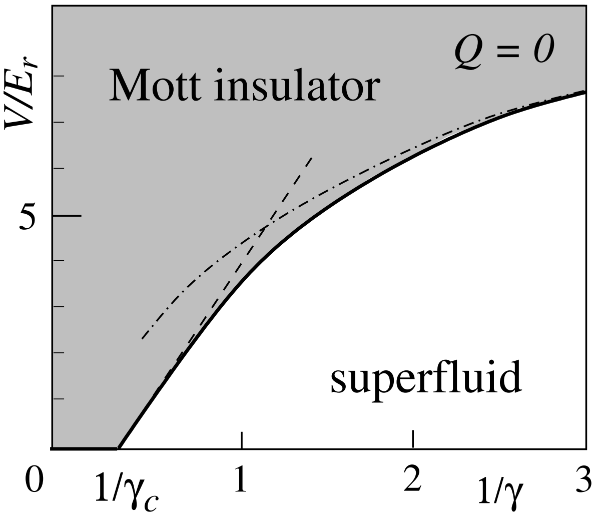

Figure 4.9: Critical amplitude V_c versus interaction $1/\gamma$ for the commensurate situation with $Q = 0$. Below $1/\gamma_c$, an arbitrary weak potential V drives the superfluid into the pinned insulating state. The dashed line denotes the asymptotic behavior near the critical point $1/\gamma_c$ as determined from the sine-Gordon model, while the dashed-dotted line derives from the Bose-Hubbard criterion $U/J|_{\mathrm{S-MI}} \approx 3.84$; the solid line interpolates between these two limits.

The experimental observation of the Mott insulating phase for any interaction

γ can be achieved by measuring the excitation gap through a phase gradient method as done previously for the Bose-Hubbard transition [69]. An alternative method would be to directly observe the increase in the long-range translational order in the Mott phase via Bragg diffraction [142, 143]. Furthermore, the change of the density profile and the resulting change in the size of the atomic cloud as shown in Fig. 4.7 offers an additional option for the observation of the Mott insulating state. In all cases, the experimentally available signal is determined by the fraction $\Delta N/N$ of particles participating in the Mott insulating phase. The latter can be further enhanced by generating an array of parallel 'atom wires' with the help of a strong 2D optical transverse lattice. Furthermore, such 2D optical transverse lattices are the most promising setup for generating one-dimensional traps with high transverse trapping frequencies. Using numbers similar to those in the recent experiment by Greiner *et al.* [69], it is possible to generate several thousand parallel 1D wires with a transverse confining frequency $\nu_\perp = 20$ kHz.

Next, we discuss an specific experimental setup which allows for the observation of the Mott insulating phase in the strongly interacting regime $\gamma > \gamma_c$ where an arbitrary weak optical lattice drives the system into the Mott insulating state. Using a 2D optical lattice to generate the one-dimensional 'atomic wires' as discussed above, a transverse confining frequency $\nu_\perp = 20$ kHz is chosen. A longitudinal harmonic trap with frequency $\nu = 40$ Hz then encloses $N \approx 50$ atoms in each 1D wire. In the absence of an optical lattice, the associated density $n(0)$ in the trap center takes the value $n(0) = 2\ \mu\mathrm{m}^{-1}$ under the assumption of large interaction $\gamma \gg 1$, i.e., the density profile takes the form Eq. 4.29. This density is commensurate with the lattice constant $\lambda/2 \approx 0.5\ \mu m$ of a typical optical lattice [69]. A weak periodic potential will then lead to an incompressible Mott state in the center of the cloud, provided the parameter $\gamma = 2a_s/n(0)l_\perp^2$ is larger than the critical value $\gamma_c \approx 3.5$. For ^{87}Rb with a scattering length $a_s \approx 5\, nm$, the resulting γ is equal to one, i.e., not quite in the required range. As noted by Petrov *et al.* [74], however, tunable and in particular larger values of γ may be realized either by changing a_s via a Feshbach resonance as present, e.g., in ^{85}Rb [57, 58, 59], or simply by increasing the transverse confinement frequency.

In conclusion we have shown that a commensurate Mott state can be realized in dilute 1D BEC's already with an arbitrary weak lattice potential, provided that the ratio γ between the interaction and kinetic energies is larger than a critical value $\gamma_c \approx 3.5$. This instability provides a new and experimentally accessible tool for the quantitative characterization of 1D atomic gases in the strongly correlated

‘Tonks gas’ limit. Also, the observation of a Mott state in a regime where the atoms are not confined to discrete lattice sites would give direct evidence for the granularity of matter in strongly interacting dilute gases [70].

Chapter 5

Supersolid versus Phase Separation in Atomic Bose-Fermi Mixtures

5.1 Introduction

Cooling atoms to the nK regime allows for the realization and study of new thermodynamic phase transitions and their associated phases, with an interesting synergy emerging between the fields of quantum atom optics and condensed matter physics. Recent trends are the study of the superfluid to Mott-insulator phase transition appearing in cold bosonic systems subject to an optical lattice [68, 69] and the striving for the realization of a BCS-type condensate in a fermionic system [93, 94, 95]. In this chapter, we investigate the possibility to realize a non-trivial supersolid phase in a mixed boson-fermion system sympathetically cooled into their corresponding quantum degenerate states [86, 87, 88, 89]. We identify a promising system where this novel phase can be observed and determine the relevant phase diagram.

Supersolids simultaneously exhibit two types of order which usually appear in competition to each other — these are the diagonal long-range order (DLRO) associated with the periodic density modulation in a crystal and the off-diagonal long-range order (ODLRO) associated with the phase order in the condensate [6]. Supersolids have been proposed to exist in the strongly interacting ^{4}He system [144, 145], where experimental results are still hotly debated [146, 147], and in various model systems describing interacting Bosons on a lattice and analyzed numerically [148, 149, 150, 151]. Here, we investigate the possibility to use a specifically tuned boson-fermion mixture to realize a supersolid phase in a controlled experiment.

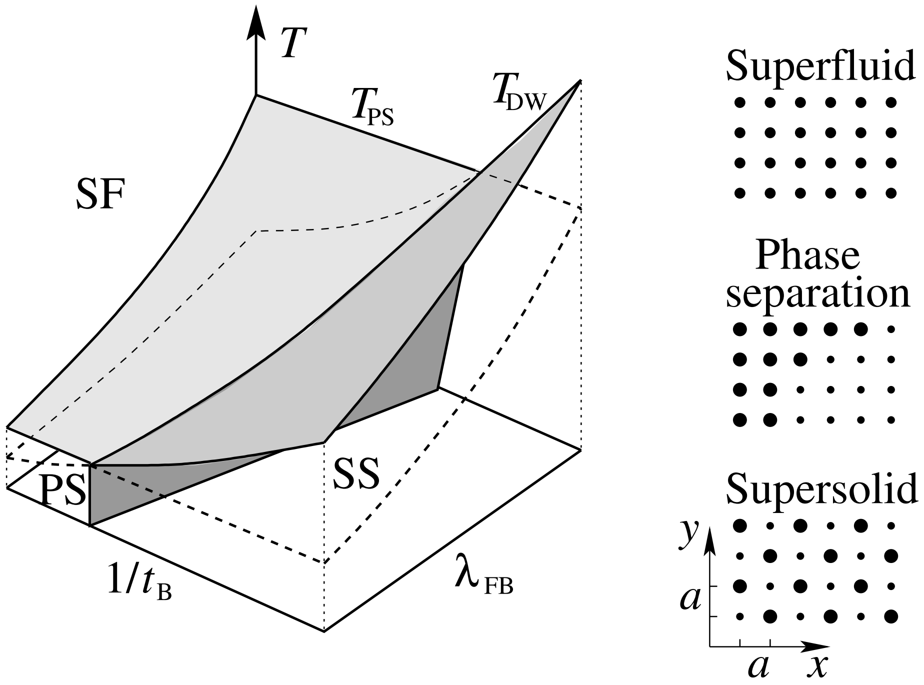

Figure 5.1: Left: Sketch of the λ_{FB}-$1/t_{\text{B}}$-T phase diagram. For $T_{\text{DW}} > T_{\text{PS}}$ the low temperature phase with $T < T_{\text{DW}}$ is a supersolid, while for $T_{\text{PS}} > T_{\text{DW}}$ the phase separated state supersedes the supersolid. Right: bosonic density $n_{\text{B}}(x, y)$ on each lattice site for the superfluid phase (SF), phase separated state (PS) with a domain wall, and supersolid (SS) phase.

The basic idea underlying our scheme is to share tasks between the fermions and the bosons: the fermions are tuned through a density wave instability establishing crystalline order (DLRO), while the condensate bosons provide the off-diagonal long-range order (ODLRO). The interaction with the fermions imprints an additional density modulation also in the bosonic density field, hence resulting in a supersolid phase. In order to trigger a density wave instability in the fermions, we confine the mixed boson-fermion system to two dimensions and subject it to an optical lattice, which provides perfect nesting properties of the Fermi surface at half-filling [152]. Note, that the resulting crystalline order relevant for the DLRO component in the supersolid is not due to the density modulation enforced by the optical lattice but is the superstructure triggered by the density wave instability.

The supersolid transition discussed here competes with phase separation in the boson system [90, 153]. Given the dimensionality and the lattice geometry of our system, the presence of van Hove singularities strongly enhances the tendency towards phase separation and produces new and interesting features in this transition: an arbitrary weak interaction between the bosons and the fermions is sufficient to drive the phase separation at low temperatures. However, proper tuning of the parameters allows to supersede this phase separation through the supersolid transition as shown in Fig. 5.1. We focus on the weak coupling between the bosons and the fermions. As a consequence, the transition temperatures T_{PS} and T_{DW} towards the phase separated state and the supersolid phase are small compared to the transition temperature T_{KT} establishing a bosonic condensate with off-diagonal long-range order. Furthermore, the weak coupling limit excludes a demixing of the repulsive fermion-boson system along the lines discussed in Ref. [91].

The Hamiltonian of an interacting Bose-Fermi mixture subjected to an optical lattice is presented in Sec. 5.2. For a strong optical lattice potential, we apply the tight-binding approximation to map the Hamiltonian to a Bose-Fermi mixture on a lattice with hopping and on-site interactions. Furthermore, integrating out the fermions allows to derive an effective boson Hamiltonian, exhibiting two instabilities. The first instability towards phase separation is examined in Sec. 5.3, and the phase separated phase is studied within the Thomas-Fermi description. The corresponding phase diagram is of the standard liquid-gas transition type. The second instability towards the formation of a fermionic density wave is presented in Sec. 5.4. The close relation between BCS superconductivity and the transition towards a density wave allows to derive a mean-field theory of the supersolid transition. We determine the properties of the supersolid phase within this mean-field theory and derive the phase diagram. Finally, the competition between the transition to a phase separated state and the supersolid transition determines the complete phase diagram of the Bose-Fermi mixture at weak coupling and is presented in Sec. 5.5. We also propose an experimental setup which allows for the observation of the supersolid phase.

5.2 Bose-Fermi mixtures

We start with interacting bosons and fermions in two dimensions. In analogy to the discussion in Sec. 4.2, such a 2D setup is achieved by a strong confining potential in transverse direction. Then, the Hamiltonian for interacting bosons and fermions subject to an optical lattice takes the form $H = H_{\mathrm{B}} + H_{\mathrm{F}} + H_{\mathrm{int}}$ with

$$\begin{aligned} H_{\mathrm{B}} &= \int d\mathbf{x}\ \psi_{\mathrm{B}}^{+}\left(-\frac{\hbar^2}{2m_{\mathrm{B}}}\triangle + V_{\mathrm{B}}(\mathbf{x})\right)\psi_{\mathrm{B}}, \\ H_{\mathrm{F}} &= \int d\mathbf{x}\ \psi_{\mathrm{F}}^{+}\left(-\frac{\hbar^2}{2m_{\mathrm{F}}}\triangle + V_{\mathrm{F}}(\mathbf{x})\right)\psi_{\mathrm{F}}, \\ H_{\mathrm{int}} &= \int d\mathbf{x}\left(g_{\mathrm{FB}}\psi_{\mathrm{B}}^{+}\psi_{\mathrm{B}}\psi_{\mathrm{F}}^{+}\psi_{\mathrm{F}} + \frac{1}{2}g_{\mathrm{B}}\psi_{\mathrm{B}}^{+}\psi_{\mathrm{B}}^{+}\psi_{\mathrm{B}}\psi_{\mathrm{B}}\right). \end{aligned} \tag{5.1}$$

Here, the interaction between the particles is taken into account within the pseudopotential approximation. We assume a repulsive interaction $g_{\mathrm{B}} = 4\pi a_s \hbar^2/m$ between the bosons with the scattering length $a_s > 0$, while the coupling $g_{\mathrm{FB}} = 2\pi a_{\mathrm{FB}}\hbar^2/\mu$ accounts for the interaction between the fermions and the bosons with μ the relative mass and a_{FB} the boson-fermion scattering length. Furthermore, we restrict the analysis to spinless fermions; such a spinless fermionic atomic gas is naturally achieved in an experiment via spin polarization. Then, the s-wave scattering length of the fermion-fermion interaction vanishes, while p-wave scattering is suppressed at low energies and is neglected in the following analysis. The optical lattice with wave length λ provides an $a = \lambda/2$-periodic potential for the bosons (α = B) and fermions (α = F) with $V_\alpha(\mathbf{x}) = V_\alpha \sin^2(\pi x/a) + V_\alpha \sin^2(\pi y/a) + V_{\mathrm{trap}}$, while the trapping potential V_{trap} includes the strong transverse confining $V_{\mathrm{trap}} = \omega_\alpha z^2/2$.

5.2.1 Hamiltonian within tight-binding approximation

In the following, we focus on strong optical lattices $V_\alpha > E_\alpha^r = 2\hbar^2\pi^2/\lambda^2 m_\alpha$ and weak interactions. Then, in analogy to the mapping to the Bose-Hubbard model presented in Sec. 4.3, we perform a mapping of the Hamiltonian for a Bose-Fermi mixture (5.1) to a simplified Hamiltonian within the tight-binding approximation. We restrict the analysis to the lowest Bloch band and introduce the Bloch wave functions v_k and w_k of the single particle problem in the 2D periodic potential. In turn, the Bloch wave functions $w_{\mathbf{k}}(\mathbf{x})$ and $v_{\mathbf{k}}(\mathbf{x})$ are related to the Wannier functions $\widetilde{w}(\mathbf{x}-\mathbf{R})$ and $\widetilde{v}(\mathbf{x}-\mathbf{R})$ according to Eq. 4.4

$$\begin{aligned}\widetilde{w}(\mathbf{x}-\mathbf{R}) &= \frac{1}{N}\sum_{\mathbf{k}\in K} w_{\mathbf{k}}(\mathbf{x})\exp\left(-i\mathbf{R}\mathbf{k}\right) &(5.2)\\ \widetilde{v}(\mathbf{x}-\mathbf{R}) &= \frac{1}{N}\sum_{\mathbf{k}\in K} v_{\mathbf{k}}(\mathbf{x})\exp\left(-i\mathbf{R}\mathbf{k}\right) &(5.3)\end{aligned}$$

with $\mathbf{R}$ a lattice vector and K the first Brillouin zone of the reciprocal lattice. Here, we have introduced the quantization volume $V = Na^2$ with N the number of unit cells. In the following, $n_{\mathrm{F,B}}$ denote the number of particles per unit cell. We express the bosonic and fermionic field operators $\psi_{\mathrm{B,F}}$ in terms of the Bloch wave functions $w_{\mathbf{k}}$ and $v_{\mathbf{k}}$, or equivalently, in terms of the Wannier functions $\widetilde{w}$ and $\widetilde{v}$

$$\begin{aligned}\psi_{\mathrm{B}}^{+}(\mathbf{x}) &= \frac{1}{\sqrt{N}}\sum_{\mathbf{k}\in K} b_{\mathbf{k}}^{+} w_{\mathbf{k}}(\mathbf{x}) = \sum_{\mathbf{R}} \widetilde{w}(\mathbf{x}-\mathbf{R})\, b_{\mathbf{R}}^{+}, &(5.4)\\ \psi_{\mathrm{F}}^{+}(\mathbf{x}) &= \frac{1}{\sqrt{N}}\sum_{\mathbf{k}\in K} c_{\mathbf{k}}^{+} v_{\mathbf{k}}(\mathbf{x}) = \sum_{\mathbf{R}} \widetilde{v}(\mathbf{x}-\mathbf{R})\, c_{\mathbf{R}}^{+}. &(5.5)\end{aligned}$$

Note, that the bosonic creation operator $b_{\mathbf{k}}^{+}$ of the Bloch wave state $w_{\mathbf{k}}$ is the Fourier transforme of the bosonic creation operator $b_{\mathbf{R}}^{+}$ for the Wannier state $\widetilde{w}(\mathbf{x}-\mathbf{R})$ with

$$b_{\mathbf{R}}^{+} = \frac{1}{\sqrt{N}}\sum_{k\in K} b_{\mathbf{k}}^{+}\exp(i\mathbf{k}\mathbf{R}), \tag{5.6}$$

and analogously for the fermionic creation operators $c_{\mathbf{k}}^{+}$ and $c_{\mathbf{R}}^{+}$. In our subsequent analysis it is convenient to use the operators $b_{\mathbf{k}}^{+}$ and $c_{\mathbf{k}}^{+}$. Inserting the expansion (5.5) into the Hamiltonian (5.1) and restricting the analysis to on-site interactions, the Hamiltonian of the Bose-Fermi mixture (5.1) reduces to

$$\begin{aligned}H = &\sum_{\mathbf{k}\in K}\epsilon_{\mathrm{B}}(\mathbf{k}) b_{\mathbf{k}}^{+} b_{\mathbf{k}} + \frac{U_{\mathrm{B}}}{2N}\sum_{\{\mathbf{k},\mathbf{k}',\mathbf{q},\mathbf{q}'\}} b_{\mathbf{k}}^{+} b_{\mathbf{q}}^{+} b_{\mathbf{k}'} b_{\mathbf{q}'}\\ &+\sum_{\mathbf{q}\in K}\epsilon_{\mathrm{F}}(\mathbf{q}) c_{\mathbf{q}}^{+} c_{\mathbf{q}} + \frac{U_{\mathrm{FB}}}{N}\sum_{\{\mathbf{k},\mathbf{k}',\mathbf{q},\mathbf{q}'\}} b_{\mathbf{k}}^{+} b_{\mathbf{k}'} c_{\mathbf{q}}^{+} c_{\mathbf{q}'}. \qquad (5.7)\end{aligned}$$

The summation $\{\mathbf{k},\mathbf{k}',\mathbf{q},\mathbf{q}'\}$ is restricted to $\mathbf{k},\mathbf{k}',\mathbf{q},\mathbf{q}'\in K$ and the momentum conservation $\mathbf{k}-\mathbf{k}'+\mathbf{q}-\mathbf{q}'=\mathbf{K}_m$ with $\mathbf{K}_m$ a vector in the reciprocal lattice; a scattering process involving such a vector $\mathbf{K}_m$ is in general denoted as an Umklapp processes. The interaction parameters become

$$\begin{aligned}U_{\mathrm{B}} &= g_{\mathrm{B}}\int d\mathbf{x}|\widetilde{w}(\mathbf{x})|^4 &(5.8)\\ U_{\mathrm{FB}} &= g_{\mathrm{FB}}\int d\mathbf{x}|\widetilde{w}(\mathbf{x})|^2|\widetilde{v}(\mathbf{x})|^2, &(5.9)\end{aligned}$$

while $\epsilon_{\mathrm{F}}(\mathbf{k})$ and $\epsilon_{\mathrm{B}}(\mathbf{k})$ denote the lowest energy band of the fermions and bosons, respectively. For a strong optical lattice only nearest neighbor hopping survives and the dispersion relations takes the form

$$\begin{aligned} \epsilon_{\mathrm{F}}(\mathbf{q}) &= -2J_{\mathrm{F}}\left[\cos\left(q_x\frac{\lambda}{2}\right)+\cos\left(q_y\frac{\lambda}{2}\right)\right], && (5.10)\\ \epsilon_{\mathrm{B}}(\mathbf{q}) &= 2J_{\mathrm{B}}\left[2-\cos\left(q_x\frac{\lambda}{2}\right)+\cos\left(q_y\frac{\lambda}{2}\right)\right] && (5.11)\end{aligned}$$

with J_{F} and J_{B} the hopping energies. Note, that we fix the bosonic energy at $\epsilon_{\mathrm{B}}(0) = 0$, while the fermionic energy vanishes at the Fermi energy for half-filling, i.e., the chemical potential μ vanishes for half filling at any temperature due to the particle-hole symmetry of the band structure. The Fermi surface at half-filling is shown in Fig. 5.2 and exhibits perfect nesting for $\mathbf{k}_{\mathrm{DW}}$ and van Hove singularities at $\mathbf{q} = (0, \pm\pi/a)$ and $\mathbf{q} = (\pm\pi/a, 0)$.

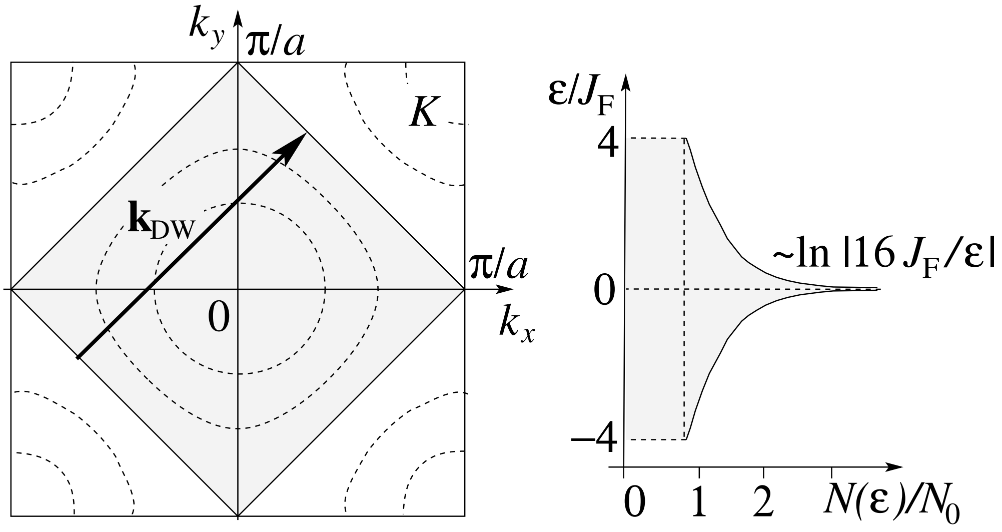
k_y
π/a
K
$\mathbf{k}_{\mathrm{DW}}$
π/a
0
k_x
$\varepsilon/J_{\mathrm{F}}$
4
0
−4
~ln |16 $J_{\mathrm{F}}/\varepsilon$|
0
1
2
$N(\varepsilon)/N_0$

Figure 5.2: Left: First Brioulline zone K and Fermi surface of 2D fermions in an optical lattice. The solid lines denote the Fermi surface at half-filling. Right: Density of states with logarithmic van Hove singularity $N(\epsilon) \sim N_0 \ln|16J_{\mathrm{F}}/\epsilon|$.

In analogy to the calculations in Sec. 4.3, a reliable estimate of the interaction strength is provided by approximating the Wannier function $\widetilde{w}(\mathbf{x})$ and $\widetilde{v}(\mathbf{x})$ by the wave function of the harmonic oscillator in each well. The oscillator frequency in each well is given by $\omega_{\text{well}} = \sqrt{4E_\alpha V_\alpha}/\hbar$ with $\alpha = \mathrm{B}, \mathrm{F}$, which implies the size of the localized wave function $a_{\text{well}} = \sqrt{\hbar/m\omega_{\text{well}}}$. The interaction strength U_{FB}

and $U_{\rm B}$ then become

$$\begin{aligned} U_{\rm B} &= 8\sqrt{\pi}\, E_{\rm B}\, \frac{a_{\rm B}}{\lambda} \left(\frac{V^z_{\rm B}}{E_{\rm B}}\right)^{1/4} \left(\frac{V_{\rm B}}{E_{\rm B}}\right)^{1/2}, & (5.12)\\ U_{\rm FB} &= 8\sqrt{\pi}\,\sqrt{E_{\rm B}E_{\rm F}}\, \frac{a_{\rm FB}}{\lambda} \left(\frac{V^z_{\rm F}}{E_{\rm F}}\frac{V^z_{\rm B}}{E_{\rm B}}\right)^{1/8} \left(\frac{V_{\rm F}}{E_{\rm F}}\frac{V_{\rm B}}{E_{\rm B}}\right)^{1/4},. & (5.13)\end{aligned}$$

while the hopping amplitude J_α derives from the exactly known width of the lowest band in the 1D Mathieu equation [139]

$$4J_\alpha = \frac{16}{\sqrt{\pi}}\sqrt{E_\alpha V_\alpha}\left(\frac{V_\alpha}{E_\alpha}\right)^{1/4} \exp\left(-2\sqrt{\frac{V_\alpha}{E_\alpha}}\right). \qquad (5.14)$$

The validity of the derivation of the Hamiltonian (5.7) requires that the interaction parameters $U_{\rm B}$ and $U_{\rm FB}$ are small compared to the energy gap $\sim \hbar\omega_{\rm well}$ to the next higher Bloch band, see Eq. (4.10).

5.2.2 Effective boson Hamiltonian

In order to study the stability of the ground state, it is convenient to derive an effective Hamiltonian for the bosons alone. Within this effective Hamiltonian, the influence of the fermions is taken into account by a modified interaction between the bosons. We start with linear response theory, where the boson density $n_{\rm B}(\mathbf{q})$ drives the fermionic system $\langle n_{\rm F}(\mathbf{q})\rangle = U_{\rm FB}\chi(T,\mathbf{q})n_{\rm B}(\mathbf{q})$ with $\chi(T,\mathbf{q})$ the response function of the fermions at temperature T. This perturbed fermionic density in turn acts as a drive for the bosons and is accounted for by the effective interaction between the bosons

$$H_{\rm int} = \frac{1}{2N}\sum_{\{\mathbf{k},\mathbf{k}',\mathbf{q},\mathbf{q}'\}} \left[U_{\rm B} + U^2_{\rm FB}\,\chi(T,\mathbf{q}-\mathbf{q}')\right] b^+_{\mathbf{k}} b_{\mathbf{k}'} b^+_{\mathbf{q}} b_{\mathbf{q}'}. \qquad (5.15)$$

The response function of the fermions is described by the Lindhard function

$$\chi(T,\mathbf{q}) = \int_K \frac{d\mathbf{k}}{v_0}\frac{f[\epsilon_{\rm F}(\mathbf{k})] - f[\epsilon_{\rm F}(\mathbf{k}+\mathbf{q})]}{\epsilon_{\rm F}(\mathbf{k}) - \epsilon_{\rm F}(\mathbf{k}+\mathbf{q}) + i\eta} \qquad (5.16)$$

with $v_0 = (2\pi/a)^2$ the volume of the first Brillouin zone. The temperature T enters via the Fermi distribution function $f(\epsilon) = 1/[1+\exp(\epsilon/T)]$. Note, that the chemical potential $\mu_{\rm F}$ of the fermions vanishes at half filling due to the particle-hole symmetry of the band structure. We focus on static instabilities of the ground state and neglect the frequency dependence of the response function. A rigorous derivation of the effective action including the time dependence is presented in Appendix C via a path integral approach. Using the fermionic dispersion relation (5.10), the Lindhard function exhibits two logarithmic singularities. These singularities give rise to instabilities in the system towards two new ground states: the singularity at $\mathbf{q} = 0$ induces an instability towards a phase separated state, while the singularity at $\mathbf{k}_{\mathrm{DW}}$ provides an instability towards density wave formation and generates a supersolid phase. In the following, we discuss these two instabilities in detail.

5.3 Phase separation

5.3.1 Instability at $q = 0$

The Lindhard function is always negative and induces an attraction between the bosons independent on the attractive/repulsive nature of the coupling U_{FB} between the bosons and fermions. The effective long distance scattering parameter for $\mathbf{q} \to 0$ takes the form

$$U_{\mathrm{eff}} = U_{\mathrm{B}} + U_{\mathrm{FB}}^2\, \chi(T, 0). \tag{5.17}$$

For a fermionic system with a regular density of states, the Lindhard function at $\mathbf{q} = 0$ and low temperatures reduces to $\chi(T \to 0, 0) = -N(0)$ with $N(0)$ the fermionic density of states. For fermions on a square lattice within a tight-binding approximation, the situation considered here, the density of states is irregular and exhibits a logarithmic van Hove singularity at $\epsilon = 0$

$$N(\epsilon) = N_0 K\left[\sqrt{1 - \frac{\epsilon^2}{16 J_{\mathrm{F}}^2}}\right] \sim N_0 \ln\left|\frac{16 J_{\mathrm{F}}}{\epsilon}\right|, \tag{5.18}$$

with $N_0 = 1/(2\pi^2 J_{\mathrm{F}})$, and $K[m]$ the complete elliptic integral of the first kind [154], see Fig. 5.2. As a consequence, the Lindhard function diverges logarithmically at half filling $n_{\mathrm{F}} = 1/2$ and $T \to 0$, and its asymptotic behavior takes the form

$$\chi(T \to 0, 0) = \int d\epsilon N(\epsilon) \frac{\partial f(\epsilon)}{\partial \epsilon} = -N_0 \ln \frac{16 c_1 J_{\mathrm{F}}}{T} \tag{5.19}$$

with $c_1 = 2\exp(C)/\pi \approx 1.13$ a numerical prefactor and $C \approx 0.577$ the Euler constant.

As a consequence of this logarithmic divergence of the Lindhard function for $T \to 0$, the effective scattering parameter U_{eff} always turns negative at low temperatures. Since, a thermodynamically stable superfluid condensate requires a positive effective interaction $U_{\text{eff}} > 0$ [155], the stable low temperature phase is no longer a superfluid condensate. We define a critical temperature T_{PS} via $U_{\text{eff}}(T_{\text{PS}}) = 0$. Using Eq. (5.17) and (5.19), we find the critical temperature

$$T_{\text{PS}} = 16 c_1 J_{\text{F}} \exp\left[-1/\lambda_{\text{FB}}\right] \tag{5.20}$$

with $\lambda_{\text{FB}} = (U_{\text{FB}}^2/U_{\text{B}})N_0$ the dimensionless coupling constant. Note, that weak coupling requires $\lambda_{\text{FB}} < 1$ and the critical temperature T_{PS} is well below the transition temperature T_{KT} of a superfluid condensate. Below the critical temperature T_{PS} the effective interaction U_{eff} turns negative providing a negative compressibility, and the superfluid condensate becomes unstable. The new ground state with fixed averaged density n_{B} and n_{F} exhibits phase separation with areas of increased and decreased local densities coexisting.

Note, that this transition towards phase separation exhibits two major differences as compared to the phase separation discussed in Ref. [90, 91]. First, the phase separation is an instability appearing at low temperatures for arbitrary small coupling U_{FB} between the bosons and fermions. Second, the increase/decrease in the bosonic density drives the fermionic density away from half-filling providing a regular $\chi(T, 0)$ which stabilizes a phase separated state.

5.3.2 Thomas-Fermi approximation

In the following, we study the phase separated state in more detail within the Thomas-Fermi theory. Within this theory, we introduce two densities $n_{\text{B}}(\mathbf{x})$ and $n_{\text{F}}(\mathbf{x})$, and assume that the system is in thermodynamic equilibrium at every position. We neglect the kinetic energy of the bosons, and the free energy $\mathcal{F}\left[n_{\text{B}}, n_{\text{F}}\right]$ of the system becomes

$$\begin{aligned}\mathcal{F}\left[n_{\text{B}}, n_{\text{F}}\right] &= \int \frac{d\mathbf{x}}{a^2} \Big\{ F_{\text{F}}\left[n_{\text{F}}(x)\right] + V_{\text{F}}(x) n_{\text{F}}(x) + V_{\text{B}}(x) n_{\text{B}}(x) \\ &\qquad + \frac{1}{2} U_{\text{B}} n_{\text{B}}(x) n_{\text{B}}(x) + U_{\text{FB}} n_{\text{B}}(x) n_{\text{F}}(x) \Big\}. \end{aligned} \tag{5.21}$$

Here, we include an external trapping potential V_{B} for the bosons and V_{F} for the fermions. Note, that we assume $T \ll T_{\text{KT}}$ which implies that the influence of thermally excited bosons is small and can be neglected. The local free energy $F_{\text{F}}[n_{\text{F}}]$ of the fermions at temperature T takes the form $(F = \Omega - \mu n)$

$$F_{\text{F}}[n_{\text{f}}] = -T \int d\epsilon N(\epsilon) \ln\left[1 + \exp\left(-\frac{\epsilon - \mu}{T}\right)\right] - \mu n_{\text{F}}. \tag{5.22}$$

The local chemical potential μ is determined by the condition that the fermionic free energy F_{F} is a minimum, i.e., $\partial_\mu F_{\mathrm{F}} = 0$, and implies the constraint

$$n_{\mathrm{F}} = \int d\epsilon N(\epsilon) f(\epsilon - \mu). \tag{5.23}$$

Furthermore, the total number of particles in the system is fixed which provides the constraints

$$N_{\mathrm{F}} = \int d\mathbf{x}\, n_{\mathrm{F}}(x), \qquad N_{\mathrm{B}} = \int d\mathbf{x}\, n_{\mathrm{B}}(x). \tag{5.24}$$

The ground state configuration at temperature T is then determined by the minima of the functional $\mathcal{F}[n_{\mathrm{B}}, n_{\mathrm{F}}]$ under the constraints (5.24). The ground state configuration satisfies

$$\begin{aligned} \mu\left[n_{\mathrm{F}}(\mathbf{x})\right] + V_{\mathrm{F}}(\mathbf{x}) + U_{\mathrm{FB}} n_{\mathrm{B}}(\mathbf{x}) &= \mu_{\mathrm{F}}, & (5.25)\\ U_{\mathrm{B}} n_{\mathrm{B}}(\mathbf{x}) + V_{\mathrm{B}}(\mathbf{x}) + U_{\mathrm{FB}} n_{\mathrm{F}}(\mathbf{x}) &= \mu_{\mathrm{B}}, & (5.26) \end{aligned}$$

where μ_{F} and μ_{B} are the Laplace multipliers introduced to fulfill the constraints. These parameters act as a global chemical potential for the system. Note, that here we used the relation $\partial_{n_{\mathrm{F}}} E_{\mathrm{F}}[n_{\mathrm{F}}] = \mu[n_{\mathrm{F}}]$.

In the following, we neglect the trapping potentials V_{F} and V_{B} and analyze the stability of the state with a homogeneous fermionic and bosonic density n_{F} and n_{B}. Such a homogeneous state state is a solution of Eq. (5.25) and (5.26) and this solution is a local minima of the functional (5.21), if the Hessian $\mathbf{H}$ is positive definite. Here, the Hessian takes the form

$$\mathbf{H} = \begin{pmatrix} \partial_{n_{\mathrm{F}}} \mu[n_{\mathrm{F}}] & U_{\mathrm{FB}} \\ U_{\mathrm{FB}} & U_B \end{pmatrix}. \tag{5.27}$$

The derivation $\partial_{n_{\mathrm{F}}} \mu[n_{\mathrm{F}}]$ is related to the response function $\chi(T, \mathbf{q})$ by the compressibility sum rule and takes the form

$$\partial_{n_{\mathrm{F}}} \mu[n_{\mathrm{F}}] = \left(\partial_{\mu_{\mathrm{F}}} n_{\mathrm{F}}\right)^{-1} = \left\{ \int d\epsilon N(\epsilon) \left[-\partial_\epsilon f(\epsilon - \mu)\right] \right\}^{-1} = -\left[\chi(T, 0)\right]^{-1}. \tag{5.28}$$

The condition that the Hessian is positive definite requires tr$\mathbf{H} > 0$ and det$\mathbf{H} > 0$, and implies the stability condition

$$\mathrm{Tr}\mathbf{H} = |\chi(T, 0)| + U_B > 0, \qquad \det\mathbf{H} = |\chi(T, 0)| U_B - U_{\mathrm{FB}}^2 > 0. \tag{5.29}$$

The first condition is satisfied satisfied for positive interaction $U_{\mathrm{B}} > 0$ between the bosons. For a regular density of states $N(\epsilon)$, the second stability condition at zero temperature $T = 0$ becomes

$$\frac{U_{\mathrm{FB}}^2}{U_{\mathrm{B}}}\, N(\varepsilon_F) = 1 \tag{5.30}$$

and coincides with the condition in Refs. [90, 91]; ε_F denotes the Fermi energy. However, for the system considered here with fermions in 2D on a square lattice, the density of states exhibits a van Hove singularity. Then, the second stability condition in (5.29) shows, that the solution $\overline{n}_{\mathrm{F}} = 1/2$ and $\overline{n}_{\mathrm{B}}$ describing fermions at half filling with arbitrary bosonic density, turns unstable at the critical temperature T_{PS}. The critical temperature as derived from (5.29) coincides with the critical temperature (5.20).

Next, we examine the solutions of Eq. (5.25) and (5.26) for fixed chemical potentials μ_{B} and μ_{F}. From Eq. (5.26), we obtain the bosonic density $n_{\mathrm{B}} = (\mu_{\mathrm{B}} - U_{\mathrm{FB}} n_{\mathrm{F}})/U_{\mathrm{B}}$ and inserting this density into Eq. (5.25), we obtain

$$\mu[n_{\mathrm{F}}] = \mu_{\mathrm{F}} - \frac{U_{\mathrm{FB}}}{U_{\mathrm{B}}}\mu_{\mathrm{B}} + \frac{U_{\mathrm{FB}}^2}{U_{\mathrm{B}}} n_{\mathrm{F}}. \tag{5.31}$$

Using (5.23) we obtain an implicit equation for n_{F}

$$n_{\mathrm{F}} = \int d\epsilon N(\epsilon)\, f\left(\epsilon - \mu_{\mathrm{F}} + \frac{U_{\mathrm{FB}}}{U_{\mathrm{B}}}\mu_{\mathrm{B}} - \frac{U_{\mathrm{FB}}^2}{U_{\mathrm{B}}} n_{\mathrm{F}}\right). \tag{5.32}$$

Of special interest are the values of the chemical potentials $\overline{\mu}_{\mathrm{F}}$ and $\overline{\mu}_{\mathrm{B}}$ for the solution $\overline{n}_{\mathrm{F}} = 1/2$ and $\overline{n}_{\mathrm{B}}$, which take the form $\overline{\mu}_{\mathrm{F}} = U_{\mathrm{FB}}\overline{n}_{\mathrm{B}}$ and $\overline{\mu}_{\mathrm{B}} = U_{\mathrm{FB}}\overline{n}_{\mathrm{F}} + U_{\mathrm{B}}\overline{n}_{\mathrm{B}}$. Inserting these chemical potentials into Eq. (5.32), we obtain

$$\delta n_{\mathrm{F}} = \int d\epsilon N(\epsilon) \left[f\left(\epsilon - \frac{U_{\mathrm{FB}}^2}{U_{\mathrm{B}}}\delta\overline{n}_{\mathrm{F}}\right) - f\left(\epsilon\right)\right] \tag{5.33}$$

with $\delta\overline{n}_{\mathrm{F}} = n_{\mathrm{F}} - \overline{n}_{\mathrm{F}}$ the deviations of the fermionic density from half filling. For $\delta n_{\mathrm{F}} \to 0$ this equation again provides the critical temperature T_{PS}. For high temperatures with $T > T_{\mathrm{PS}}$, Eq. (5.33) has only the stable solution $\delta n_{\mathrm{F}} = 0$, while for low temperatures $T < T_{\mathrm{PS}}$ this solution turns unstable and two additional solutions $\delta n_{\mathrm{F}} \neq 0$ appear. At zero temperature, we obtain for small λ_{FB}

$$\delta\overline{n}_{\mathrm{F}} = \frac{U_{\mathrm{FB}}^2}{U_{\mathrm{B}}} \int_0^{\delta n_{\mathrm{F}}} dn N\left(\frac{U_{\mathrm{FB}}^2}{U_{\mathrm{B}}} n\right) \sim \delta\overline{n}_{\mathrm{F}} \lambda_{\mathrm{FB}} \ln\left(\frac{16 c_2 J_{\mathrm{F}} U_{\mathrm{B}}}{U_{\mathrm{FB}}^2 |\delta\overline{n}_{\mathrm{F}}|}\right) \tag{5.34}$$

with $c_2 = \exp(1)$. Solving this equation, provides the shifts in the fermionic and bosonic densities

$$\begin{aligned} n_{\rm F} - \overline{n}_{\rm F} &= \delta\overline{n}_{\rm F} = \pm 16 c_2 \frac{U_{\rm B} J_{\rm F}}{U_{\rm FB}^2} \exp\left(-\frac{1}{\lambda_{\rm FB}}\right), \\ n_{\rm B} - \overline{n}_{\rm B} &= -\frac{U_{\rm FB}}{U_{\rm B}} \delta\overline{n}_{\rm F} = \mp 16 c_2 \frac{J_{\rm F}}{U_{\rm FB}} \exp\left(-\frac{1}{\lambda_{\rm FB}}\right). \end{aligned} \tag{5.35}$$

We obtain a BCS type relation between the density shift $\delta n_{\rm F}$ and the critical temperature $T_{\rm PS}$,

$$\frac{U_{\rm FB}^2}{U_{\rm B}} \frac{\delta\overline{n}_{\rm F}}{T_{\rm PS}} = c_2/c_1 \approx 2.40. \tag{5.36}$$

However, here, we obtain a different numerical factor as we cut the integration at zero temperature in a different way as in BCS theory. Inserting the solutions (5.35) into the free energy (5.21), provides the energy shift per unit cell at zero temperature

$$\frac{\Delta\mathcal{F}}{N} = -\frac{U_{\rm FB}^2}{2U_{\rm B}} \left(\delta\overline{n}_{\rm F}\right)^2. \tag{5.37}$$

5.3.3 Phase diagram

The solution discussed above allow now to sketch the phase diagram of the system. We find that at low temperature $T < T_{\rm PS}$, we can distinguish between a low-density 'gas' phase with $n_{\rm F} \leq 1/2 - \delta\overline{n}_{\rm F}$, and a high-density 'fluid' phase with $n_{\rm F} \geq 1/2 + \delta\overline{n}_{\rm F}$. Note, that the bosonic density derives via $n_{\rm B} = (\mu_{\rm B} - U_{\rm FB} n_{\rm F})/U_{\rm B}$. For repulsive interaction $U_{\rm FB} > 0$ the fermionic low-density phase exhibits a high bosonic density, while for attractive interaction $U_{\rm FB} < 0$ the fermionic low-density phase also implies a low bosonic density.

The phase transition is then of the standard liquid-gas transition type, see Fig. 5.3. The low-density 'gas' phase is separated by a first order phase transition from the high-density 'liquid' phase at the critical chemical potential

$$\overline{\mu}_{\rm F} = \frac{U_{\rm FB}}{U_{\rm B}} \overline{\mu}_{\rm B} - \frac{U_{\rm FB}^2}{2U_{\rm B}}. \tag{5.38}$$

A fixed averaged fermionic density between $1/2 - \delta\overline{n}_{\rm F} < n_{\rm F} < 1/2 + \delta\overline{n}_{\rm F}$ is only achieved by the coexistence of the low density 'gas' phase with the high density 'liquid' phase. This coexistence phase establishes phase separation between the low-density phase with $n_{\rm F} = 1/2 - \delta\overline{n}_{\rm F}$ and the high-density phase with $n_{\rm F} = 1/2 + \delta\overline{n}_{\rm F}$. The first order transition terminates in a critical endpoint at the temperature $T_{\rm PS}$ and density $n_{\rm F} = 1/2$. Varying the temperature along the isochore $n_{\rm F} = 1/2$, we obtain a second order phase transition between the homogeneous phase and the phase separated state, see Fig. 5.3. This transition appears for arbitrary weak coupling $U_{\rm FB}$ due to the enhanced fermionic density of states for 2D fermions. Note, that a first order instability towards phase separation preempting the second order transition at $T_{\rm PS}$ [91] is excluded in the weak coupling analysis considered here.

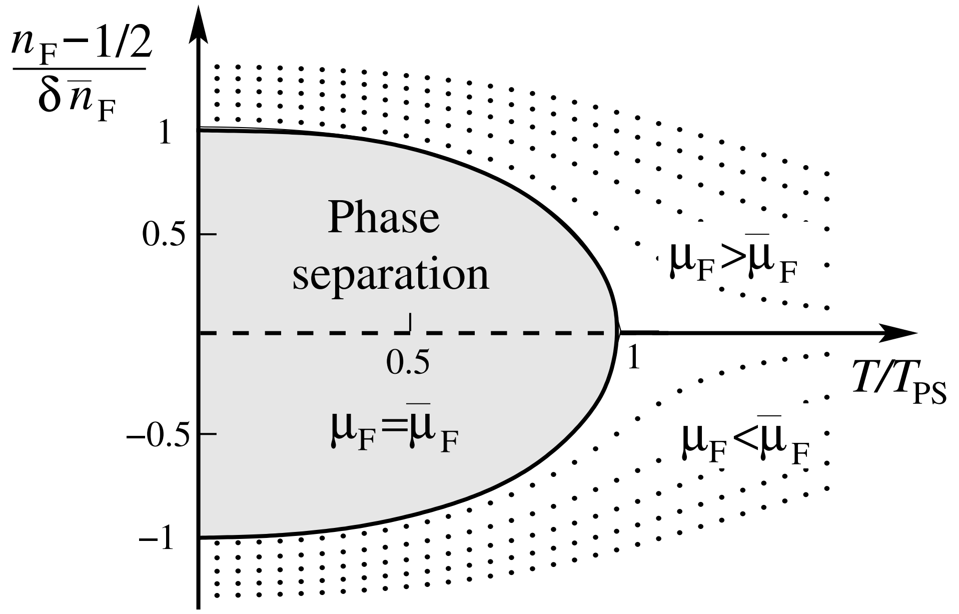

Figure 5.3: The $T - n_{\rm F}$ phase diagram of the transition towards phase separation. The grey region marks the coexistence phase of the low-density 'gas' and the high-density 'liquid' phase. The solid line denotes the line of fixed chemical potential $\overline{\mu}_{\rm F}$, while the dotted lines account for the lines at fixed chemical potentials $(\mu_{\rm F} - \overline{\mu}_{\rm F})/T_{\rm PS} = \pm 0.02, 0.06, 0.01, 0.14, 0.18$.

5.4 Supersolids

5.4.1 Instability at $\mathbf{k}_{\rm DW}$

The instability at $\mathbf{q} = 0$ towards phase separation is in competition with a second instability in the system triggered by the singularity in the Lindhard function at

$\mathbf{k}_{\mathrm{DW}}$. Using Eq. (5.16) and the symmetry $\epsilon_{\mathrm{F}}(\mathbf{q}+\mathbf{k}_{\mathrm{DW}}) = -\epsilon_{\mathrm{F}}(\mathbf{q})$ the Lindhard function at $\mathbf{k}_{\mathrm{DW}}$ and low temperatures behaves as

$$\chi(T, \mathbf{k}_{\mathrm{DW}}) = -\int d\epsilon N(\epsilon) \frac{\tanh\left(\frac{\epsilon}{2T}\right)}{2\,\epsilon} = -\frac{N_0}{2}\left[\ln\frac{16 c_1 J_{\mathrm{F}}}{T}\right]^2. \tag{5.39}$$

Note, that the constant $c_1 = 2\exp(C)/\pi \approx 1.13$ coincides with the constant in Eq. (5.19). Here, the combination of van Hove singularities and perfect nesting, see Fig. 5.2, produces the $[\ln T]^2$ behavior at the singularity, a phenomenon relevant for the enhancement of superconductivity in the presence of van Hove singularities [156].

We focus on temperatures below the superfluid transition temperature $T < T_{\mathrm{KT}}$. Then within Bogoliubov theory, the bosonic quasi-particle spectrum becomes

$$E_{\mathrm{B}}(\mathbf{q}) = \sqrt{\epsilon_{\mathrm{B}}^2(\mathbf{q}) + 2 n_{\mathrm{B}} \epsilon_{\mathrm{B}}(\mathbf{q})\left[U_{\mathrm{B}} + U_{\mathrm{FB}}^2\,\chi(T,\mathbf{q})\right]}. \tag{5.40}$$

The spectrum turns linear at small wave vectors $\mathbf{k} \to 0$ with the sound velocity

$$v_s = \sqrt{\frac{n_{\mathrm{B}}\left[U_{\mathrm{B}} + U_{\mathrm{FB}}^2\,\chi(T,0)\right]}{m}}. \tag{5.41}$$

Note, that the sound velocity turns imaginary (negative compressibility) at the critical temperature T_{PS}. In the following we focus on the second instability at $\mathbf{k}_{\mathrm{DW}}$. Then, with decreasing temperatures T, the quasi-particle energy at $\mathbf{k}_{\mathrm{DW}}$ decreases and even vanishes ($E_{\mathrm{B}}(\mathbf{k}_{\mathrm{DW}}) = 0$) at the critical temperature T_{DW}. Using Eq. (5.40) and (5.39), this critical temperature becomes

$$T_{\mathrm{DW}} = 16 c_1\, J_{\mathrm{F}} \exp\left[-\sqrt{\frac{2+t_{\mathrm{B}}}{\lambda_{\mathrm{FB}}}}\right] \tag{5.42}$$

with $t_{\mathrm{B}} = 8 J_{\mathrm{B}}/n_{\mathrm{B}} U_{\mathrm{B}}$ the ratio between the kinetic and the interaction energy of the bosons. The weak coupling analysis requires $t_{\mathrm{B}} > \lambda_{\mathrm{FB}}$. This dimensionless hopping t_{B} also appears as the parameter driving the superfluid to Mott insulator quantum phase transition for $t_{\mathrm{B}} < t_{\mathrm{SF-MI}} \approx 0.3$ [68]. Then the superfluid to Mott insulator transition provides an additonal competing phase for $t_{\mathrm{B}} \approx 0.3$.

Below the critical temperature T_{DW}, both zero energy modes b_0 and $b_{\mathbf{k}_{\mathrm{DW}}}$ become macroscopically occupied and provide two bosonic condensates. Furthermore, this macroscopic occupation of $b_{\mathbf{k}_{\mathrm{DW}}}$ also characterizes a fermionic density wave [152]. In turn, the interference of the bosonic condensates b_0 and $b_{\mathbf{k}_{\mathrm{DW}}}$ provide a bosonic density wave. In this new phase appearing for $T < T_{\mathrm{DW}}$, a (quasi) condensate characterized by an off-diagonal (quasi) long-range order with a finite superfluid stiffness and a density wave providing diagonal long-range order coexist and establish a supersolid phase.

5.4.2 Mean field theory

In the following, we study this supersolid phase appearing for temperatures below $T_{\rm DW}$ within a mean field theory. We introduce the mean fields

$$\langle b_0 \rangle = \sqrt{n_0 N}\exp(i\varphi_0) \qquad \langle b_{\mathbf{k}_{\rm DW}} \rangle = \frac{\Delta}{2U_{\rm FB}}\sqrt{\frac{N}{n_0}}\exp(i\varphi_{\rm DW}). \tag{5.43}$$

Here, n_0 denotes the order parameter of the bosonic condensate at $\mathbf{k} = 0$ with the phase φ_0, while Δ is the order parameter of the fermionic density wave with the phase $\varphi_{\rm DW}$. In addition, Δ also describes a second bosonic condensate at $\mathbf{k}_{\rm DW}$. Note, that within a lattice, the vector $\mathbf{k}_{\rm DW}$ denotes the corner point $(\pi/a, \pi/2)$ in the Brillouin zone. This corner point represents a special point with higher symmetry; all corner points differ from each other by a reciprocal lattice vector. As a consequence, we have only one mean field $\Delta\exp(i\varphi_{\rm DW})$ describing the fermionic density wave. In the following, we focus on low temperatures with $T \ll T_{\rm KT}$ allowing us to neglect thermal excitations of bosonic quasi-particles. The bosonic density operator takes the form

$$n_{\rm B}(\mathbf{q}) = \sum_{\mathbf{k},\mathbf{k}'\in K,m} b^{+}_{\mathbf{k}} b_{\mathbf{k}'} \;\; \delta_{\mathbf{K}_m,\mathbf{k}-\mathbf{k}'+\mathbf{q}}. \tag{5.44}$$

Then, the interference between the two bosonic condensates induces a bosonic density wave with

$$\begin{aligned} n_{\rm B}(0) &= n_0 + \frac{\Delta^2}{4n_0U_{\rm FB}^2} = n_{\rm B} && (5.45)\\ n_{\rm B}(\mathbf{k}_{\rm DW}) &= \langle b_0^{+}\rangle\langle b_{\mathbf{k}_{\rm DW}}\rangle + \langle b^{+}_{\mathbf{k}_{\rm DW}}\rangle\langle b_0\rangle = \frac{\Delta\cos\theta}{U_{\rm FB}} && (5.46)\end{aligned}$$

From the first equation, we obtain the constraint $n_{\rm B} = n_0 + \Delta^2/(4n_0U_{\rm FB}^2)$ with $n_{\rm B}$ the averaged particle density. Furthermore, the bosonic density in real space takes the form (to be evaluated at lattice sites)

$$n_{\rm B}(x, y) = n_{\rm B} + \frac{\Delta\cos\theta}{U_{\rm FB}}\left[\cos\frac{\pi x}{a}\cos\frac{\pi y}{a}\right] \tag{5.47}$$

with $\theta = \varphi_0 - \varphi_{\rm DW}$. This bosonic density wave appears via the interference of the two condensates $\langle b_0\rangle$ and $\langle b_{\mathbf{k}_{\rm DW}}\rangle$. Inserting the mean field $\langle b_0\rangle$ and $\langle b_{\mathbf{k}_{\rm DW}}\rangle$ into the Hamiltonian (5.7) and neglecting terms independent on Δ, we obtain

$$\frac{H}{N} = 2J_{\rm B}\frac{\Delta^2}{n_{\rm B}U_{\rm FB}^2} + \frac{U_{\rm B}\Delta^2\cos^2\theta}{2U_{\rm FB}^2} + \frac{H_{\rm F}}{N} + o(\Delta^4). \tag{5.48}$$

The first and second terms describe the increase in the kinetic and interaction energies of the bosons, while $H_{\rm F}$ accounts for the nesting of fermions with $\mathbf{q} \in K$ and $\mathbf{q}' = \mathbf{q} - \mathbf{k}_{\rm DW} + \mathbf{K}_m$ (the reciprocal lattice vector $\mathbf{K}_m$ ensures the constraint $\mathbf{q}' \in K$)

$$H_{\rm F} = \frac{1}{2}\sum_{\mathbf{q}\in K}\left(c_{\mathbf{q}}^{+}\,,\;\; c_{\mathbf{q}'}^{+}\right)\left(\begin{array}{cc} \epsilon_{\rm F}(\mathbf{q}) & \Delta\cos\theta \\ \Delta\cos\theta & -\epsilon_{\rm F}(\mathbf{q})\end{array}\right)\left(\begin{array}{c} c_{\mathbf{q}} \\ c_{\mathbf{q}'}\end{array}\right). \tag{5.49}$$

Diagonalizing this Hamiltonian, we obtain the fermionic quasi-particle excitation spectrum $\tilde{\epsilon}_{\rm F}(\mathbf{k}) = \pm[\epsilon_{\rm F}^2(\mathbf{k}) + \cos^2\theta\Delta^2]^{1/2}$. The fermionic excitation spectrum opens up a gap Δ at the Fermi energy for half filling; the energy of the states $\epsilon < 0$ decreases via the mixing of the fermionic wave functions $c_{\mathbf{q}}$ with $c_{\mathbf{q}'}$. The thermodynamic potential $\Omega(T,\Delta,\theta)$ becomes

$$\frac{\Omega(T,\Delta,\theta)}{N} = 2J_{\rm B}\frac{\Delta^2}{n_{\rm B}U_{\rm FB}^2} + \frac{U_{\rm B}\Delta^2\cos^2\theta}{2U_{\rm FB}^2} - T\int\frac{d\mathbf{k}}{v_0}\ln\left[1+\exp\left(-\frac{\tilde{\epsilon}_{\rm F}}{T}\right)\right]. \tag{5.50}$$

Minimizing this potential $\Omega(T,\Delta,\theta)$ at fixed temperature provides the constraint $\theta = s\pi$ with s an integer, and the self-consistency relation ($\partial_\Delta\Omega = 0$)

$$\frac{1}{\lambda_{\rm FB}}(2+t_{\rm B}) = \frac{1}{N_0}\int_K\frac{d\mathbf{k}}{v_0}\frac{\tanh\left[\tilde{\epsilon}_{\rm F}(\mathbf{k})/2T\right]}{\tilde{\epsilon}_{\rm F}(\mathbf{k})}\,. \tag{5.51}$$

The critical temperature, characterizing the onset of a fermionic density wave, derives for $\Delta = 0$, and provides the same critical temperature $T_{\rm DW}$ as obtained from the instability criterion (5.42). The opening of the excitation gap Δ modifies the fermionic density of states $N_\Delta(\epsilon) = N(\sqrt{\epsilon^2-\Delta^2})|\epsilon|/\sqrt{\epsilon^2+\Delta^2}$. Then, the gap Δ at $T = 0$ becomes

$$\Delta(0) = 32J_{\rm F}\exp\left[-\sqrt{\frac{2+t_{\rm B}}{\lambda_{\rm FB}}}\right]. \tag{5.52}$$

We obtain the standard BCS relation $2\Delta(0)/T_{\rm DW} = 2\pi/\exp(C) \approx 3.58$ between the gap at $T = 0$ and the transition temperature. The condensation energy $E_{\rm C}$ per unit cell at zero temperature becomes

$$E_{\rm C} = \left[\sqrt{\frac{1}{\lambda_{\rm FB}}(2+t_{\rm B})} + \frac{1}{2}\right]\frac{\Delta^2 N_0}{4}. \tag{5.53}$$

In contrast to standard BCS theory, here the condensation energy involves the large parameter $(2+t_{\rm B})/\lambda_{\rm FB}$ in the prefactor, and strongly enhances the condensation energy. The fermionic density modulation in the ground state becomes (to be evaluated on lattice sites)

$$n_{\rm F}(x,y) = n_{\rm F} + \Delta\ \cos\theta\, N_0\, \frac{2+t_{\rm B}}{\lambda_{\rm FB}} \left[\cos\frac{\pi x}{a}\cos\frac{\pi y}{a}\right]. \tag{5.54}$$

Finally, we calculate the superfluid stiffness of the bosons. Following the definition of superfluid stiffness in Ref. [145], we calculate the shift of the ground state energy due to twisted boundary conditions for the bosons with $\Delta\phi = L|\Delta\mathbf{k}|$ the phase shift by moving a particle through the system of length L ($|\Delta\mathbf{k}| < 2\pi/L$). Such a twisted boundary condition induces a continuous flow of bosonic particles through the system, and induces a shift of the ground state energy of the Bose-Fermi mixture. This energy shifts appears as a combination of increased kinetic energy of the bosons condensed in the lowest energy state and a reduction of the condensation energy of the density wave. Within mean field theory, the kinetic energy shift of the bosons takes the form

$$\frac{\Delta\Omega_{\rm B}(\Delta\mathbf{k})}{N} = n_{\rm B}\epsilon_{\rm B}(\Delta\mathbf{k}) + \frac{\Delta^2}{4n_{\rm B}U_{\rm FB}^2}\left[\epsilon_{\rm B}(\mathbf{k}_{\rm DW}+\Delta\mathbf{k}) - \epsilon_{\rm B}(\Delta\mathbf{k})\right]. \tag{5.55}$$

The coupling with the fermions induces a shift of the fermionic gap Δ. We introduce the parameter $t_{\rm B}(\Delta\mathbf{k}) = t_{\rm B} + \Delta t_{\rm B}(\Delta\mathbf{k})$

$$\Delta t_{\rm B} = \frac{\epsilon_{\rm B}(\mathbf{k}_{\rm DW}+\Delta\mathbf{k}) - \epsilon_{\rm B}(\mathbf{k}_{\rm DW}) - \epsilon_{\rm B}(\Delta\mathbf{k})}{n_{\rm B}U_{\rm B}}, \tag{5.56}$$

which accounts for the shift in the bosonic hopping energy and provides via (5.52) and (5.53) the shift in the condensation energy of the supersolid phase (only leading order correction in $\Delta t_{\rm B}$)

$$\frac{\Delta\Omega(\Delta\mathbf{k})}{N} = -E_{\rm C} + n_{\rm B}\epsilon_{\rm B}(\Delta\mathbf{k}) + \frac{\Delta^2}{4U_{\rm FB}^2 n_{\rm B}}\ \left[\epsilon_{\rm B}(\mathbf{k}_{\rm DW}+\Delta\mathbf{k}) - \epsilon_{\rm B}(\mathbf{k}_{\rm DW}) - \epsilon_{\rm B}(\Delta\mathbf{k})\right]. \tag{5.57}$$

Using the dispersion relation (5.11) and performing the second derivative with respect to $\Delta\mathbf{k}$ provides the superfluid stiffness

$$\rho_s = \frac{n_{\rm B}}{m^*}\left(1 - \frac{\Delta^2}{2U_{\rm FB}^2 n_{\rm B}^2}\right) \tag{5.58}$$

with $m^* = 2\hbar^2/(J_{\rm B}\lambda^2)$ the effective band mass. We conclude that the formation and pinning of the charge density wave by the optical lattice leads to a reduction in the superfluid stiffness.

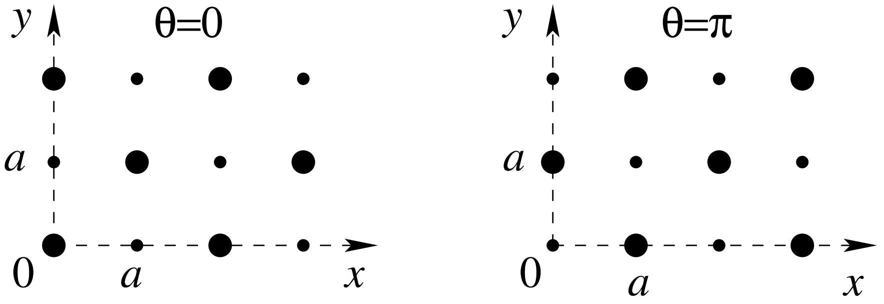

Figure 5.4: Fermionic density distribution $n_{\mathrm{F}}(x,y)$ of the two degenerated ground states of the supersolid phase. The ground state with $\theta = 0$ (right) and the state with $\theta = \pi$ (left) differ by a translation to the nearest neighbor site.

The mean field value of $\langle b_0 \rangle = \sqrt{n_0 N} \exp[i\varphi_0]$ describes the off-diagonal (quasi) long-range order and breaks the continuous $U(1)$ symmetry of the system. The excitation spectrum exhibits a linear dispersion around $q = 0$ and at finite temperature only quasi long-range order survives due to fluctuations. This (quasi) long-range order is sufficient to provide a finite superfluid stiffness below the Kosterlitz-Thouless transition temperature T_{KT} [145]. In addition, the coupling between the fermions and the bosons produces a fermionic density wave instability characterized by the mean field $\Delta \exp(i\varphi_{\mathrm{DW}})$, see Eq. (5.54). In turn, this fermionic density wave induces a bosonic condensate $\langle b_{\mathbf{k}_{\mathrm{DW}}} \rangle$ and a bosonic density wave via the interference between the two condensates, see Eq. (5.47). Then the new phase establishes a supersolid characterized by the coexistence of off-diagonal and diagonal long-range order. The phase φ_{DW} of the fermionic density wave is locked to the phase φ_0 of the condensate via the constraint $\varphi_0 - \varphi_{\mathrm{DW}} = \theta = s\pi$ and describe two degenerated ground states, see Fig. 5.4. Note, that this transition breaks the discrete translation symmetry and establishes diagonal long-range order. The fermionic excitation spectrum becomes gapped with $\tilde{\epsilon}_{\mathrm{F}}(\mathbf{k}) = \pm\sqrt{\epsilon_{\mathrm{F}}(\mathbf{k})^2 + \Delta^2}$. In addition, the bosonic excitation spectrum is also gapped around $\mathbf{q} = \mathbf{k}_{\mathrm{DW}}$.

Varying the chemical potential of the fermions, the supersolid phase is stabilized by the opening of the fermionic excitation gap for $\Delta\mu < \Delta$. This allows to sketch the T-$\Delta\mu$ phase diagram of the supersolid phase, see Fig. 5.5. For a fermionic density at half-filling $n_{\mathrm{F}} = 1/2$, the transition from the superfluid to the supersolid is a second order phase transition at the critical temperature T_{DW}. In turn, for temperatures $T < T_{\mathrm{DW}}$ the superfluid to supersolid transition is tuned

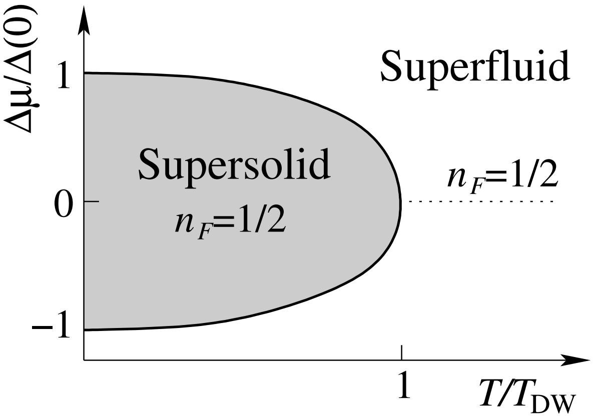

Figure 5.5: Sketch of the phase diagram for the superfluid to supersolid transition. For a fixed fermionic density $n_{\rm F} = 1/2$, a second order transition takes place at the critical temperature $T_{\rm DW}$. Within the supersolid phase, the fermionic excitation spectrum opens up a gap, and the fermionic density is fixed at half-filling.

by the chemical potential. Within the supersolid phase, the fermions are incompressible and exhibit a fixed density $n_{\rm F} = 1/2$. The opening of a gap protects the supersolid phase from small variations in the chemical potential induced by an additional trapping potential. This protection is important in an experimental realization of the supersolid phase: it is sufficient to prepare the initial state with a fermionic density in the trap center close to half-filling. Then the supersolid phase appears in the trap center over a large region and fixes the fermionic density at half-filling within this region. Such a behavior is in close analogy to the superfluid to Mott insulator transition, see previous chapter. Furthermore, the opening of the gap also protects the supersolid state from small modifications in the band structure arising from next-nearest neighbor hopping, and justifies our starting Hamiltonian (5.7) neglecting such terms.

5.5 Phase diagram and conclusions

The competition between the instabilities towards phase separation and the instability towards a supersolid phase provides the complete phase diagram of the Bose-Fermi mixture for weak coupling, see Fig. 5.1. For $T_{\rm DW} > T_{\rm PS}$ the supersolid phase supersedes phase separation. Then, at the critical temperature $T_{\rm DW}$, we enter the supersolid phase and a gap opens in the fermionic excitation spectrum characterizing an incompressible Fermi gas. This fermionic gap removes the instability towards phase separation. Furthermore, the comparison of the condensation energies (5.37) and (5.53) shows that a first order transition to the phase separated state is excluded. Then, the system remains supersolid for all temperatures $T < T_{\mathrm{DW}}$. In turn, for $T_{\mathrm{PS}} > T_{\mathrm{DW}}$ phase separation wins over density wave formation. Then, below the transition temperature T_{PS}, we enter the phase separated state which drives the fermionic density away from half-filling. The nesting with $\mathbf{k}_{\mathrm{DW}}$ is quenched and the instability towards density wave formation disappears. Now, the comparison between the condensation energies (5.37) and (5.53) shows, that for $(T_{\mathrm{PS}} - T_{\mathrm{DW}})/T_{\mathrm{PS}} \ll 1$ we can drive a first order transition towards the supersolid phase by lowering the temperature. The projection of the critical line $T_{\mathrm{PS}} = T_{\mathrm{DW}}$ onto the λ_{FB}-t_{B} plane satisfies

$$\frac{1}{t_{\mathrm{B}}} = \frac{\lambda_{\mathrm{FB}}}{1 - 2\lambda_{\mathrm{FB}}}. \tag{5.59}$$

For decreasing coupling λ_{FB} the supersolid phase supersedes the instability towards phase separation, while increasing the hopping t_{B} drives the system into the phase separated state. Using the result (5.59) beyond the weak coupling limit indicates, that for a coupling strength with $\lambda_{\mathrm{FB}} > 1/2$, the transition towards the supersolid phase is forbidden.

Next, we estimate the experimental parameters for an atomic mixture of fermionic ^{40}K and bosonic ^{87}Rb with scattering lengths $a_{\mathrm{B}} = 5.77\,\mathrm{nm}$ and $a_{\mathrm{FB}} \approx 15\,\mathrm{nm}$ [89]. The 2D setup is achieved by applying an anisotropic 3D optical lattice ($\lambda = 830$ nm and $V_{\mathrm{F}}/V_{\mathrm{B}} \approx 3/7$) with $V_{\mathrm{F}}^z \gg V_{\mathrm{F}}$ and $V_{\mathrm{B}}^z \gg V_{\mathrm{B}}$ which quenches inter-plane hopping. Note, that here $V_{\mathrm{F,B}}$ and $V_{\mathrm{F,B}}^z$ are expressed in terms of the recoil energies $E_{\mathrm{F,B}}^r = 2\pi^2\hbar^2/\lambda^2 m_{\mathrm{F,B}}$. The hopping amplitudes J_{F} and J_{B} for the lowest band derive from the well-known 1D Mathieu equation,

$$\frac{J_{\mathrm{F,B}}}{E_{\mathrm{F,B}}^r} = \frac{4}{\sqrt{\pi}} V_{\mathrm{F,B}}^{3/4} \exp\left(-2\sqrt{V_{\mathrm{F,B}}}\right), \tag{5.60}$$

while the interactions U_{FB} and U_{B} are given as [68]

$$\frac{U_{\mathrm{FB}}}{E_{\mathrm{F}}^r} = 8\sqrt{\pi}\frac{1 + m_{\mathrm{F}}/m_{\mathrm{B}}}{\left(1 + \sqrt{V_{\mathrm{F}}/V_{\mathrm{B}}}\right)^{3/2}} \frac{a_{\mathrm{FB}}}{\lambda\gamma} \left(V_{\mathrm{F}}^z\right)^{1/4} V_{\mathrm{F}}^{1/2} \tag{5.61}$$

$$\frac{U_{\mathrm{B}}}{E_{\mathrm{B}}^r} = 4\sqrt{2\pi}\,\frac{a_{\mathrm{B}}}{\lambda\gamma} \left(V_{\mathrm{B}}^z\right)^{1/4} V_{\mathrm{B}}^{1/2} \tag{5.62}$$

Using a finite angle between the laser beams producing the standing light waves, we allow the change the relative size of the in- and out-of-plane lattice constants

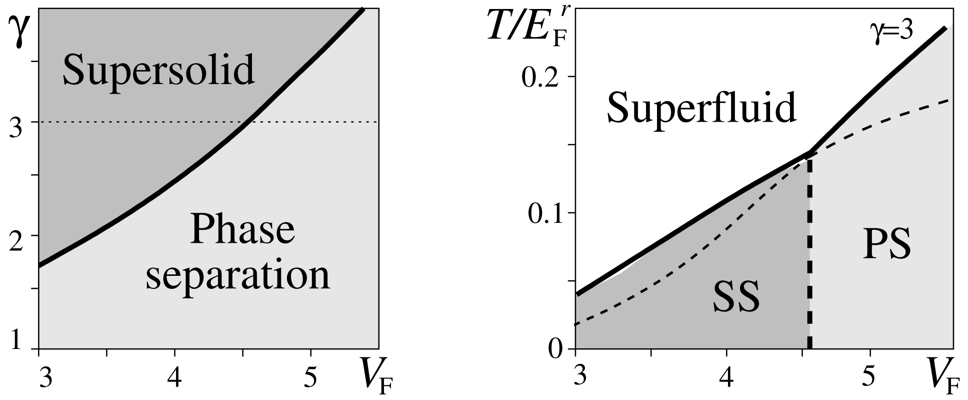

Figure 5.6: Left: V_{F}-γ phase diagram at low temperatures. Increasing the strength of the optical lattice allows to drive the transition from a supersolid to a phase separated state. Right: Transition temperatures for $\gamma = 3$. The first order transition line (solid-dashed line) separating the supersolid from the phase separated state is only a guide to the eye, and can be derived by a comparison of the condensation energies in the phase separated state and the supersolid phase.

a and a_z. The parameter $\gamma = 2a_z/\lambda$ denotes the increase in volume of the unit cell, and allows to tune the interaction strengths U_{B} and U_{FB} independent on the hopping amplitudes $J_{\text{F,B}}$. An alternative method to tune the interaction U_{FB} between the bosons and fermions can be realized via Feshbach resonances [57, 58, 59]. Fixing $V_{\text{F}}^z = 20$, $n_{\text{F}} = 1/2$, and $n_{\text{B}} = 3/2$, we obtain for $\gamma = 3$ and $V_{\text{F}} = 4.5$ the dimensionless coupling parameters $\lambda_{\text{FB}} \approx 0.39$, $t_{\text{B}} \approx 0.55$ with the transition temperature $T_{\text{DW}} \approx 48\,\text{nK}$; we enter a regime at the border of the validity of our weak coupling analysis. Using the above estimates, the V_{F}-γ phase diagram at low temperatures is shown in Fig. 5.6, and we find that changing the strength of the optical lattice V_{F} allows to drive the transition from the supersolid to a phase separated state. The supersolid state is easily detected via the usual coherence peak of a bosonic condensate in an optical lattice: after a ballistic expansion of the condensate the interference pattern of the bosons reveal the reciprocal lattice structure of the optical lattice. Within the supersolid phase, the induced density wave then produces additional coherence peaks at $\mathbf{k}_{\text{DW}}$. Using the above parameters, the weight of these additional peaks involve 15% of the total particle number.

In conclusion, we have identified a new supersolid phase in a 2D Fermi-Bose gas mixture subject to an optical lattice. The boson play the role of phonons in a condensed matter system and mediate an attraction between the fermions. The perfect Fermi-surface nesting with $\mathbf{k}_{\mathrm{DW}}$ leads to the appearance of a fermionic density wave and the condensation of the bosons at $\mathbf{k}_{\mathrm{DW}}$. The bosonic density wave then appears via the interference between the condensate at $\mathbf{k}_{\mathrm{DW}}$ and the usual bosonic condensate at $\mathbf{k} = 0$. This bosonic density wave and the condensate at $\mathbf{k} = 0$ then establish diagonal long-range order (DLRO) and off-diagonal long-range order (ODLRO), the characteristic property of a supersolid phase.

Appendix A

Quantum Nucleation Rates

In this appendix, we perform the analytic continuation of the integral expression (2.59) and (2.63). All integral formulas used are tabulated in Ref. [157, 139]. The duplication and reflection formula for the Gamma function will be used often and take the form

$$\begin{aligned} \frac{2^{2\mu-2}}{\sqrt{\pi}}\Gamma(\mu)\Gamma(\mu-\frac{1}{2}) &= \Gamma(2\mu-1), &\text{(A.1)}\\ \Gamma(\mu)\Gamma(1-\mu) &= \frac{\pi}{\sin\pi\mu}. &\text{(A.2)} \end{aligned}$$

We start with the infinite wire at finite temperature $T = 1/\beta$. The decay rate (2.59) takes the form

$$\Gamma = \frac{\lambda^2}{\kappa}\frac{L}{c_s\kappa}\left(\frac{\pi\kappa}{\hbar\beta}\right)^{2\mu-2} \mathrm{Im}\left\{\int_\gamma \frac{dw}{2}\int_0^\infty d\lambda \frac{2^\mu \exp(w\alpha)}{(\cosh\lambda-\cos w)^\mu}\right\}$$

with the dimensionless variables for the space coordinate $\lambda = 2\pi x/c_s\hbar\beta$ and the time coordinate $w = 2\pi\tau/\hbar\beta$, while the driving current is given by $\alpha = \hbar\beta I/2e$. The integration contour γ is defined by the analytic continuation of the integral [158, 107, 109]. We follow the real axis up to the saddle point and then integrate to $+i\infty$. The integration along the real axis contributes only to the real part. The analytic properties of the integrand allows to shift the contour to the imaginary axis and we obtain with $w = iu$

$$\mathrm{Im}\left\{\int_\gamma dw\right\} = \mathrm{Im}\left\{\int_0^{+i\infty} dw\right\} = \mathrm{Re}\left\{\int_0^\infty du\right\} \tag{A.3}$$

Note, that in the integral expression we drop the high energy cut-off κ, and the integral converges only for $0 < \mu < 1$. As the imaginary part of the integral is regular in μ, we obtain the result for $\mu > 1$ via analytic continuation. The integration over λ can be performed by using a decomposition of the integral by

$$I_1 = I_2 + I_3 = \int_0^\infty d\lambda \frac{1}{(\cosh\lambda - \cos w)^\mu}$$

$$= \int_u^\infty d\lambda \frac{1}{(\cosh\lambda - \cosh u)^\mu} + \int_0^u d\lambda \frac{\exp(i\pi\mu)}{(\cosh u - \cosh\lambda)^\mu}$$

The contour γ acquires a small negative real part due to the analytic continuation, i.e., $w = (i - |\epsilon|)u$ and consequently the branch cut of the logarithm leads to a term $(-1)^{-\mu} = \exp(i\pi\mu)$. Both integrals are tabulated and we obtain

$$\begin{aligned} I_2 &= \sqrt{\frac{2}{\pi}}\Gamma(\mu)\frac{e^{i\pi(\mu-1/2)}}{(\sinh u)^{\mu-1/2}} Q_{-1/2}^{1/2-mu}(\cosh u) && \text{(A.4)} \\ I_3 &= \sqrt{\frac{\pi}{2}}\Gamma(1-\mu)\frac{e^{i\pi\mu}}{(\sinh u)^{\mu-1/2}} P_{-1/2}^{\mu-1/2}(\cosh u) && \text{(A.5)} \end{aligned}$$

with $P_{-1/2}^{\mu-1/2}$and $G_{-1/2}^{1/2-\mu}$ Legendre functions. The Legendre functions can be expressed by Hypergeometric function ${}_2F_1$ implying

$$\begin{aligned} I_2 &= 2^\mu \frac{\pi}{\sin\pi\mu} z^{\mu/2}(1-z)^{1-2\mu}\ {}_2F_1(1-\mu, 1-\mu; 1; z) \\ I_3 &= -2^\mu \frac{\pi e^{i\pi\mu}\cos\pi\mu}{\sin\pi\mu}\frac{\Gamma(2\mu-1)}{\Gamma(\mu)^2} z^{\mu/2}(1-z)^{1-2\mu} \\ &\qquad {}_2F_1(1-\mu, 1-\mu; 2-2\mu; 1-z) \end{aligned}$$

with $z = \exp(-2u)$. We first perform the remaining integral over u with the integrand I_3 and obtain

$$\begin{aligned} J_3 &= \int_0^\infty \frac{du}{2} 2^\mu \exp(\alpha i u) I_3(u) = \int_0^1 dz 2^\mu z^{-i\alpha/2-1} I_3(z) \\ &= 2^{2\mu-1} e^{\pi i\mu} \frac{\sin^2\pi\frac{\mu-i\alpha}{2}}{\sin^2\pi\mu} \frac{|\Gamma\left(\frac{\mu-i\alpha}{2}\right)\Gamma\left(\frac{\mu+i\alpha}{2}\right)|^2}{\Gamma(\mu)^2} \end{aligned}$$

The singularities in μ represent the fact that the integrals converge only for $0 < \mu < 1$. However, we can now apply the analytic continuation of J_3 to any value of μ and obtain the real part of J_3 via the relation

$$\mathrm{Re}\left\{2e^{\pi i\mu}\frac{\sin^2\pi(\frac{\mu-i\alpha}{2})}{\sin^2\pi\mu}\right\} = e^{\pi\alpha} - 2\frac{|\sin\pi\frac{\mu-i\alpha}{2}|^2}{\sin^2\pi\mu} \qquad \text{(A.6)}$$

The first part is regular and determines the decay rate, while the second term is canceled by the real part of J_2 the integral over u with the integrand I_2. Therefore the decay rate becomes

$$\Gamma = \frac{y^2 L}{\kappa^2 c_s} \left(\frac{2\pi\kappa}{\hbar\beta}\right)^{2\mu-2} \exp(\frac{\hbar\beta I}{2e}) \frac{\left|\Gamma\left(\frac{\mu}{2} - i\frac{\hbar\beta I}{4e}\right)\right|^4}{\Gamma(\mu)^2} \tag{A.7}$$

The zero temperature limit is obtained via the relation

$$\left|\Gamma\left(\frac{\mu - i\alpha}{2}\right)\right|^4 \approx \exp(-\pi\alpha)\left(\frac{\alpha}{2}\right)^{2\mu-2}. \tag{A.8}$$

For J_2 we obtain

$$\begin{aligned} J_2 &= \int_0^\infty \frac{du}{2} 2^\mu \exp(\alpha i u) I_2(u) = \int_0^1 dz z^{-i\alpha/2-1} I_2(z) \\ &= 2^{2\mu} \frac{\pi^2 \; {}_3F_2\left(1-\mu, 1-\mu, \frac{\mu-i\alpha}{2}; 1, 2-\frac{3\mu+i\alpha}{2}; 1\right)}{\sin\pi\mu \sin\pi(2\mu-1)\Gamma(2\mu-1)\Gamma\left(2-\frac{3\mu+i\alpha}{2}\right)} \end{aligned}$$

For $\alpha = 0$ we can apply the relation

$$\begin{aligned} {}_3F_2(a, b, c; 1+a-b, 1+a-c; 1) &= \\ \frac{2^{-a}\sqrt{\pi}\Gamma(1+a-b)\Gamma(1+a-c)}{\Gamma(1/2+a/2)\Gamma(1+a/2-b)\Gamma(1+a/2-c)} & \frac{\Gamma(1+a/2-b-c)}{\Gamma(1+a-b-c)} \end{aligned} \tag{A.9}$$

and obtain

$$J_2 = 2^{2\mu-3} \frac{1}{\cos^2 \pi\frac{\mu}{2}} \frac{\Gamma\left(\frac{\mu}{2}\right)^4}{\Gamma(\mu)^2} \tag{A.10}$$

which shows that it cancels the singular part in J_3. For $\alpha \neq 0$ we have not yet been able to prove analytically that the real part of J_2 exactly cancels the singularities in J_3. However, numerical calculations with Mathematica confirm this hypothesis.

In this second part we calculate the decay rate (2.63) for a finite wire with length L at zero temperature;

$$\Gamma = \frac{\lambda^2}{\kappa} \frac{L}{c_s\kappa} \left(\frac{\pi c_s \kappa}{L}\right)^{2\mu-2} \mathrm{Im}\left\{\int_\gamma \frac{dw}{2} \int_0^\pi d\lambda \frac{2^{2\mu}\exp(w\alpha)}{(\cosh\lambda - \cos w)^\mu}\right\} \tag{A.11}$$

with $\lambda = 2\pi x/L$, $w = 2\pi\tau/c_s L$ and $\alpha = IL/2ec_s$. For $I < I_w$ the analytic continuation acquires a small positive real part and the contour γ does not provide an imaginary part; the decay rate vanishes identically. The integral over λ is tabulated and we obtain

$$\begin{aligned} I_4 &= \int_0^{\pi} d\lambda \frac{1}{(\cosh w - \cos\lambda)^{\mu}} && \text{(A.12)} \\ &= \pi 2^{\mu} e^{i\pi(1-2\mu)} \left[1 - z\right]^{1-2\mu} z^{\mu} \, {}_2F_1(1-\mu, 1-\mu; 1; z) \end{aligned}$$

with $z = \exp(2w)$. The remaining integral along the contour γ is also tabulated and takes the form

$$\begin{aligned} J_4 &= \int_{\gamma} \frac{dw}{2} 2^{2\mu} I_4(w) && \text{(A.13)} \\ &= (-1)\pi 2^{2\mu-2} e^{i\pi(1-2\mu)} \frac{\Gamma\left(\frac{\mu+\alpha}{2}\right)\Gamma\left(2-2\mu\right)}{\Gamma\left(\frac{\mu+\alpha}{2}+2-2\mu\right)} && \text{(A.14)} \\ &\quad \times {}_3F_2\left(1-\mu, 1-\mu, \frac{\mu+\alpha}{2}; 1, \frac{\mu+\alpha}{2}+2-2\mu; 1\right) \end{aligned}$$

The singularities in μ of this expression disappear by taking the imaginary part

$$\mathrm{Im}\left\{(-1)\Gamma(2-2\mu)e^{i\pi(1-2\mu)}\right\} = \frac{\pi}{\Gamma(2\mu-1)} \qquad \text{(A.15)}$$

and we obtain the decay rate

$$\begin{aligned} \Gamma &= \frac{\lambda^2 L}{\kappa^2 c_s} \frac{\pi^2}{\Gamma\left(2\mu-1\right)} \frac{\Gamma\left(\frac{\mu}{2}+\frac{IL}{4ec_s}\right)}{\Gamma\left(2+\frac{IL}{4ec_s}-\frac{3\mu}{4}\right)} \left(\frac{2\pi c_s \kappa}{L}\right)^{2\mu-2} && \text{(A.16)} \\ &\quad \times {}_3F_2\left(1-\mu, 1-\mu, \frac{\mu}{2}+\frac{IL}{4ec_0}; 1, 2+\frac{IL}{4ec_s}-\frac{3\mu}{2}; 1\right). \end{aligned}$$

For $I = I_w$ the decay rate is finite indicating a jump in the decay rate at the critical value

$$\Gamma(I_w) = \frac{\pi^2\lambda^2 L}{\kappa^2 c_s}\left(\frac{2\pi c_s \kappa}{L}\right)^{2\mu-2} f(\mu) \qquad \text{(A.17)}$$

where $f(\mu) \approx 1$ collects the terms containing the Hypergeometric function and Gamma functions. For large currents we obtain the asymptotic behavior of the decay rate

$$\int_0^1 dz\,(1-z)^{1-2\mu} z^{\frac{\mu+\alpha}{2}-1} \, {}_2F_1(1-\mu, 1-\mu; 1; z) \approx \frac{\Gamma(2-2\mu)\Gamma\left(\frac{\mu+\alpha}{2}\right)}{\Gamma\left(\frac{\mu+\alpha}{2}+2-2\mu\right)} \frac{\Gamma(2\mu-1)}{\Gamma(\mu)^2} \qquad \text{(A.18)}$$

and

$$\frac{\Gamma\left(\frac{\mu+\alpha}{2}\right)}{\Gamma\left(\frac{\mu+\alpha}{2}+2-2\mu\right)} \approx \left(\frac{\alpha}{2}\right)^{2\mu-2} \qquad \text{(A.19)}$$

and recover the nuclation rate in an infinite wire at zero temperature.

Appendix B

Modified Renormalization Group Equation

In this section we derive the scaling equation for a Coulomb gas. The derivation of the scaling equation for an interaction between a vortex-antivortex pair without boundary conditions is given in Ref. [8]. The similar scaling analysis for the 1D situation is studied in Ref. [105, 106, 159]. Here, we show that the scaling equation remain invariant by imposing boundary conditions to the system, i.e., the interaction G between the vortex-antivortex pair denotes the Greens function of the Laplace equation with appropriate boundary conditions.

The scaling is carried out in real space. We introduce the variable $\mathbf{r}_i = (x_i, c_s\tau_i)$. Increasing the cut-off parameter x_0 to $x_0 + dx$ leads to the integral relation

$$\begin{aligned} \int_{D_1 \ldots D_{2n}} \prod_i^{2n} d\mathbf{r}_i \;&=\; \int_{D'_1 \ldots D'_{2n}} \prod_i^{2n} d\mathbf{r}_i \\ &+\frac{1}{2}\sum_{i\neq j} \int_{D'_1 \ldots \cancel{D}'_j \ldots \cancel{D}'_i \ldots D'_{2n}} \prod_{k\neq i,j} d\mathbf{r}_k \int_{\delta_i(j)} d\mathbf{r}_i \int_{\overline{D}_j} d\mathbf{r}_j + O(dx) \end{aligned} \tag{B.1}$$

where D_i and D'_i is defined as the the whole plane except the circles $|\mathbf{r}_i - \mathbf{r}_j| < x_0$ and $|\mathbf{r}_i - \mathbf{r}_j| < x_0 + dx$, respectively, while $\delta_i(j)$ is the area $x_0 < |\mathbf{r}_i - \mathbf{r}_j| < x_0 + dx$, and $\overline{D}_j$ is the whole plane except the circles with radius x_0 around the other $2n-2$ points, $\mathbf{r}_k$. The decomposition $1/2\sum_{i\neq j}$ selects a particle i, j and pairs it with particle j, while the integration over $\delta_i(j)$ restricts to relative distance between the paired particles to the change in the scale $x_0 < |\mathbf{r}_i - \mathbf{r}_j| < x_0 + dx$. The integration over $\overline{D}_j$ then moves this pair to all positions in the allowed region.

The interaction energy between two particles with the same charge $\nu_i = \nu_j$ is large and is neglected, i.e., we restrict the calculations to particle-antiparticle–pairs.

We select all terms in the integrand containing i, j and apply an expansion in the small inter-particle distance $\bar{\mathbf{r}} = \mathbf{r}_i - \mathbf{r}_j$ to second order (summation over indices k, l is always restricted to $k, l \neq i, j$)

$$\begin{aligned}
&\int_{\delta_i(j)} d\mathbf{r}_i \exp\left(\mu \sum_k [\nu_i \nu_k G(\mathbf{r}_i, \mathbf{r}_k) + \nu_j \nu_k G(\mathbf{r}_j, r_k)]\right) \\
&= \int_{\delta_i(j)} d\mathbf{r}_i \left(1 + \frac{\mu^2}{2} \sum_{k,l} \nu_j^2 \nu_l \nu_k [\bar{\mathbf{r}}\, \nabla G(\mathbf{r}_j, \mathbf{r}_k)][\bar{\mathbf{r}}\, \nabla G(\mathbf{r}_j, \mathbf{r}_l)]\right. \\
&\qquad \left. - \frac{\mu}{2} \sum_k \nu_j \nu_k \partial_\alpha \partial_\beta G(\mathbf{r}_j, \mathbf{r}_k) r_\alpha r_\beta \right) \qquad \text{(B.2)}
\end{aligned}$$

Performing the integral over $\mathbf{r}_i$, the last term becomes $\frac{\mu\pi}{2} \sum_k \nu_j \nu_k \Delta G(\mathbf{r}_j, \mathbf{r}_k) x_0^2 = 0$ and drops out, while the remaining part simplifies to

$$= x_0 dx \left[2\pi + x_0^2 \frac{\pi \mu^2}{2} (\nabla\phi)^2\right]. \qquad \text{(B.3)}$$

Finally the remaining integral over $\overline{D}_j$ can be performed and leads to

$$= 2\pi x_0 dx \left[A - x_0^2 \pi \mu \sum_k \nu_k \nu_l G(\mathbf{r}_k, \mathbf{r}_l)\right] \qquad \text{(B.4)}$$

where A denotes the whole area of the configuration space. Writing this term as an exponent leads to a modification of the interaction between the particles of the form

$$G(\mathbf{r}_i, \mathbf{r}_j) \to \left[1 + \frac{4\mu\pi^2}{\tau} y^2\right] G(\mathbf{r}_i, \mathbf{r}_j) \qquad \text{(B.5)}$$

which proves the scale invariance of the system in first order perturbation theory of the Coulomb gas with boundary conditions and determines the scaling equation of μ

$$\partial_l \mu = 4\pi^2 \mu^2 y^2 \qquad \text{(B.6)}$$

with $l = (x_0 + dx)/x_0$. The first term in (B.4) determines the change in free energy due to the presence of particle-antiparticle–pairs on short distances and is irrelevant for the consideration of the decay rate. The scaling of the fugacity y is obtained by the replacement of the cut-off x_0 by the new cut-off $x_0 + dx$ and the scaling is determined by the invariance of

$$y^{2n} \int \prod_i^{2n} \frac{d\mathbf{r}_i}{x_0^2} e^{2n \ln x_0^2} = y^{2n}(l) \int \prod_i^{2n} \frac{d\mathbf{r}_i}{(l x_0)^2} e^{2n \ln (l x_0)^2} \qquad \text{(B.7)}$$

and leads to the scaling law

$$\partial_l y = (2 - \mu) y. \tag{B.8}$$

This calculations show that imposing boundary conditions to the Coulomb gas leaves the scaling equation invariant.

Appendix C

Effective Action within a Path Integral Approach

An exact derivation for the effective interaction mediated by the fermions is obtained by integrating out the fermions within a path integral formalism. Here, we start with the path integral in imaginary time for the bosons and fermions at finite temperature T

$$\mathcal{Z} = \int \mathcal{D}[c^{+}]\mathcal{D}[c\,]\mathcal{D}[b^{+}]\mathcal{D}[b\,] \exp\left(-\frac{S_{\mathrm{E}}}{\hbar}\right). \tag{C.1}$$

The Euclidean action takes the form $S_{\mathrm{E}} = S_{\mathrm{B}} + S_{\mathrm{F}} + S_{\mathrm{FB}}$ with

$$\begin{aligned} S_{\mathrm{B}} &= T \sum_{s\in\mathbf{Z},\mathbf{k}\in K} \left\{ [i\,\omega_s + \epsilon_{\mathrm{B}}(\mathbf{k})]\, b^{+}_{\mathbf{k}}(\omega_s) b_{\mathbf{k}}(\omega_s) + \frac{U_{\mathrm{B}}}{2} n_{\mathrm{B}}(\omega_s,\mathbf{k}) n_{\mathrm{B}}(\omega_s,\mathbf{k}) \right\} \\ S_{\mathrm{F}} &= T \sum_{s\in\mathbf{Z},\mathbf{k}\in K} [i\,\Omega_s + \epsilon_{\mathrm{F}}(\mathbf{k})]\, c^{+}_{\mathbf{k}}(\Omega_s) c_{\mathbf{k}}(\Omega_s) \\ S_{\mathrm{FB}} &= T \sum_{s\in\mathbf{Z},\mathbf{k}\in K} U_{\mathrm{FB}} n_{\mathrm{B}}(\omega_s,\mathbf{k}) n_{\mathrm{F}}(\Omega_s,\mathbf{k}) \end{aligned} \tag{C.2}$$

Here, $\omega_s = 2\pi s T/\hbar$ denotes the Matsubara frequency respecting periodic boundary conditions of the bosonic field operators, while $\Omega_s = \pi(2s+1)T/\hbar$ accounts for the Matsubara frequency respecting anti-periodic boundary conditions of the fermionic field operator. Furthermore, we introduced $n_{\mathrm{B}}(\omega_s,\mathbf{q})$ for the bosonic density operator

$$n_{\mathrm{B}}(\omega_s,\mathbf{q}) = \sum_{\mathbf{k},\mathbf{k}',\mathbf{K}_m} b^{+}_{\mathbf{k}}(\omega_s)\, b_{\mathbf{k}'}(\omega_s)\, \delta(\mathbf{q} + \mathbf{k} - \mathbf{k}' + \mathbf{K}_m) \tag{C.3}$$

$$n_{\mathrm{F}}(\Omega_s,\mathbf{q}) = \sum_{\mathbf{k},\mathbf{k}',\mathbf{K}_m} c^{+}_{\mathbf{k}}(\Omega_s)\, c_{\mathbf{k}'}(\Omega_s)\, \delta(\mathbf{q} + \mathbf{k} - \mathbf{k}' + \mathbf{K}_m) \tag{C.4}$$

with $\mathbf{K}_m$ in the reciprocal lattice. It follows, that the path integral is quadratic in the fermionic field operators $c_{\mathbf{k}}^{+}$ and $c_{\mathbf{k}}$, and the integration over the fermionic fields can be performed exactly. Then, we obtain

$$\mathcal{Z} = \int \mathcal{D}[b^{+}]\mathcal{D}[b\,] \det\left\{G^{-1} + F\left[n_{\mathrm{B}}\right]\right\} \exp\left(-\frac{S_{\mathrm{B}}}{\hbar}\right) \tag{C.5}$$

with G the fermionic Greens function defined via

$$G^{-1}(\Omega_s, \Omega_s', \mathbf{k}, \mathbf{k}') = [\, i\Omega_s + \epsilon_{\mathrm{F}}(\mathbf{k})]\, \delta(\Omega_s - \Omega_s')\delta(\mathbf{k} - \mathbf{k}' + \mathbf{K}_m) \tag{C.6}$$

and the perturbation

$$F(\Omega_s, \Omega_s', \mathbf{k}, \mathbf{k}') = n_{\mathrm{B}}(\Omega_s - \Omega_s', \mathbf{k} - \mathbf{k}'). \tag{C.7}$$

The effective action for the bosons than takes the form $S_{\mathrm{B}} + S_{\mathrm{int}}$ with

$$S_{\mathrm{int}} = -\mathrm{Tr}\ln\left\{G^{-1} + F\right\} \tag{C.8}$$

Expanding this expression in second order

$$S_{\mathrm{int}} = -\mathrm{Tr}\ln G^{-1} + \mathrm{Tr}GF - \frac{1}{2}\mathrm{Tr}GFGF \tag{C.9}$$

The first term describes the contribution of the fermions in the noninteracting system, while the second term takes the form

$$\begin{aligned}
\mathrm{Tr}GF &= U_{\mathrm{FB}} n_{\mathrm{B}}\, T \sum_{s\in\mathbf{Z},\mathbf{k}\in K} \frac{1}{i\hbar\Omega_s + \epsilon_{\mathrm{F}}(\mathbf{k})} && \text{(C.10)}\\
&= U_{\mathrm{FB}} n_{\mathrm{B}} \frac{2\pi}{\hbar} \sum_{\mathbf{k}\in K} \oint_{\gamma} dz \frac{1}{1+\exp(iz\hbar/T)} \frac{1}{i\hbar z + \epsilon_{\mathrm{F}}(\mathbf{k})} && \text{(C.11)}\\
&= U_{\mathrm{FB}} n_{\mathrm{B}} \sum_{\mathbf{k}\in K} \frac{1}{1+\exp\left[\epsilon_{\mathrm{F}}(\mathbf{k})/T\right]} = U_{\mathrm{FB}} n_{\mathrm{B}} n_{\mathrm{F}} && \text{(C.12)}
\end{aligned}$$

and induces a shift $U_{\mathrm{FB}} n_{\mathrm{F}}$ in the chemical potential of the bosons. The third term then reduces to

$$\begin{aligned}
\mathrm{Tr}GFGF &= U_{\mathrm{FB}}^2 T^2 \sum_{s,s'\in\mathbf{Z},\mathbf{k},\mathbf{k}'\in K} \frac{1}{i\hbar\Omega_s + \epsilon_{\mathrm{F}}(\mathbf{k})} n_{\mathrm{B}}(\Omega_s - \Omega_{s'}, \mathbf{k} - \mathbf{k}')\\
&\qquad \times \frac{1}{i\hbar\Omega_{s'} + \epsilon_{\mathrm{F}}(\mathbf{k}')} n_{\mathrm{B}}(\Omega_{s'} - \Omega_s, \mathbf{k}' - \mathbf{k}) && \text{(C.13)}\\
&= U_{\mathrm{FB}}^2 \sum_{s\in\mathbf{Z},\mathbf{q}\in K} n_{\mathrm{B}}(\omega_s, \mathbf{q}) \chi\left(i\omega_s, \mathbf{q}, T\right) n_{\mathrm{B}}(-\omega_s, -\mathbf{q}) && \text{(C.14)}
\end{aligned}$$

Here, χ denotes the Lindhard function

$$\chi\left(i\omega_s, \mathbf{q}, T\right) = \sum_{\mathbf{k}\in K} \frac{f\left[\epsilon_{\mathrm{F}}(\mathbf{k})\right] - f\left[\epsilon_{\mathrm{F}}(\mathbf{k}+\mathbf{q})\right]}{\omega + \epsilon_{\mathrm{F}}(\mathbf{k}) - \epsilon_{\mathrm{F}}(\mathbf{k}+\mathbf{q}) + i\eta} \tag{C.15}$$

Appendix D

General concepts of physics on low dimensions

D.1 The boundary sine-Gordon problem

In the recent years great progress has been made in solving 1+1 dimensional quantum field theory problems. Here, we focus on the exactly solvable boundary sine-Gordon problem on a half line [160, 161] The action in imaginary time takes the form

$$\mathcal{S} = \int_0^{1/T} d\tau \int_0^{\infty} dx \left[\frac{K}{4\pi} \left(\partial_\mu \phi\right)^2 + \lambda \cos(\phi) \delta(x) \right. \\ \left. + \Lambda \cos(2\phi) \; + \frac{F}{2\pi} \partial_x \phi \right] . \tag{D.1}$$

The last term describes a driving term and allows to consider non-equilibrium properties of the system. Of special interest is the limit $\Lambda \to 0$ due to its applications to many physical system, e.g., impurity problems (see Chapter D.2.1), and a particle with damping in a periodic potential (see Chapter D.2.2). We will restrict our discussion to this particular limit $\Lambda = 0$. Applying perturbation theory in λ, provides the partition function at $F = 0$ [23, 162]

$$\mathcal{Z} = \sum_n \frac{1}{(n!)^2} \lambda^{2n} \mathcal{Z}_n \tag{D.2}$$

with

$$\mathcal{Z}_n = \int_0^{1/T} \prod_i^{2n} d\tau_i \; \exp\left(\frac{1}{2} \sum_{i \neq j} \nu_i G\left(\tau_i, \tau_j\right) \nu_j \right) . \tag{D.3}$$

This partition function describes a classical gas of 1d charges $|\nu_i| = 1$ with charge neutrality $\sum_i \nu_i = 0$ and logarithmic interaction

$$G(\tau_i, \tau_j) = \frac{1}{K} \ln \left[\left(\frac{\kappa}{T\pi} \right)^2 \sin^2 \pi T (\tau_i - \tau_j) \right] \tag{D.4}$$

where κ is a system depending renormalization constant. There are two critical points of the system: weak coupling with $\lambda = 0$ and strong coupling $\lambda \to \infty$. For finite coupling λ, the behavior is controlled by the dimensionless parameter K. The first order RG equation has been calculated in [159] and take the form

$$\partial_l [\lambda/\kappa] = (1 - \frac{1}{K})[\lambda/\kappa]. \tag{D.5}$$

For $K < 1$ the system flows to weak coupling in the infrared limit (IR) and to strong coupling in the ultraviolet (UV), while for $K > 1$ the properties of the system are determined by the strong coupling fix-point in the IR and weak coupling in the UV.

	IR	UV
$K > 1$	strong coupling	weak coupling
$K < 1$	weak coupling	strong coupling

The exact solution of the boundary sine-Gordon model allows not only to calculate thermodynamic quantities, but also to derive the response function $X(F,T) = \partial_t \int_0^\infty dx \partial_x \phi$ for arbitrary driving forces F and temperatures T. The response function is a universal function of F/T and T/T_B [110]

$$X(K, \frac{F}{T}, \frac{T}{T_B}) \tag{D.6}$$

with

$$T_B = \kappa' \lambda^{\frac{K}{K-1}} \tag{D.7}$$

and κ' a system depending renormalization factor (for a relation between κ' and κ see Eq. D.9 and Eq. D.24). The response function is derived by using a special set of quasiparticle states where the scattering matrix at the boundary and the scattering of quasi particles in the bulk is exactly known from the exact solution of the sine-Gordon problem. Via the thermodynamic Bethe-ansatz technology the density of states and the distribution function are calculated. The response function is then derived via a kinetic (Boltzmann) equation due to scattering at the boundary of the quasiparticles [110].

A duality in the system was first predicted by Schmid [23] who noted that the perturbative expansion (D.2) coincides with an instanton expansion under the duality $K \to 1/K$ and $\lambda \to \widetilde{\lambda} \propto \lambda^{-1/K}$. As a consequence, the perturbative calculation in λ of the response X in the case $K < 1$ [163] lead to similar algebraic corrections as the instanton expansion for quantum tunneling in the case $K > 1$ [17, 99] under the above duality transformation. Using the exact solution, the duality implies a relation for the response function at zero temperature $T = 0$ [110, 164]

$$\mathcal{X}\left(K, u\right) = 1 - \mathcal{X}\left(1/K, u\right) = \frac{i}{4u} \int_{\gamma} dx \frac{1}{\sqrt{x + x^{K} - u^{2}}} \tag{D.8}$$

where we have introduced the new variables

$$u = \frac{F}{T_{B}'} \qquad \mathcal{X} = \frac{KX}{F} \qquad T_{B}' = T_{B} \frac{2\sqrt{\pi} K \Gamma\left[\frac{1}{2} + \frac{1}{2(K-1)}\right]}{\Gamma\left[\frac{1}{2(K-1)}\right]} \tag{D.9}$$

The above duality relation is expected to hold also at finite temperature and allows to calculate transport properties in the strong coupling limit via perturbation theory in the weak coupling limit.

D.2 Application to physical relevant systems

D.2.1 Luttinger liquid with impurity

It is well known that interacting fermions in 1D have non-Fermi–liquid behavior known as Luttinger liquid. Applying the usual bosonization procedure [100] leads to the action

$$\mathcal{S} = \frac{\hbar}{K\pi} \int_{0}^{\infty} d\tau \int_{-\infty}^{\infty} dx \left\{ \frac{1}{2v} \left(\partial_{\tau} \theta\right)^{2} + \frac{v}{2} \left(\partial_{x} \theta\right)^{2} \right\} \tag{D.10}$$

with v the sound velocity and K the Luttinger parameter describing the interaction between the fermions, i.e., $K > 1$ for attractive fermions, while $K < 1$ describes repulsive fermions, and $K = 1$ is the limit of free electrons. The field θ is a bosonic field and is called the charge field due to its properties that $Q = e\partial_{x}\theta/\pi$ describes the charge density for the electrons, while $I = -e\partial_{t}\theta/\pi$ is the current density. On the other hand the bosonization also provides the dual phase field ϕ

$$\partial_{x}\phi = -\frac{1}{Kv}\partial_{t}\theta \qquad \partial_{t}\phi = \frac{v}{K}\partial_{x}\theta \tag{D.11}$$

and the equivalent description of the system by the action

$$\mathcal{S} = \frac{\hbar K}{\pi} \int_0^{1/T} d\tau \int_{-\infty}^{\infty} dx \left\{ \frac{1}{2v} \left(\partial_\tau \phi\right)^2 + \frac{v}{2} \left(\partial_x \phi\right)^2 \right\}. \tag{D.12}$$

However, in the one-dimensional electron liquid the charge is the measurable quantity and transport properties are performed by applying a voltage across the channel, which leads to a driving force

$$\mathcal{S}_F = \int_0^{1/T} d\tau \int_{-\infty}^{\infty} dx \frac{eV}{\pi} \partial_x \theta. \tag{D.13}$$

This is in contrast to the superconducting case discussed in the next section where the phase field is the macroscopic variable and standard calculations are performed for a current biased (see Eq. D.18).

Transport properties in this system with a single impurity was extensively studied by Kane and Fisher [123, 163]. They considered two different models for the impurity:

	$H_{\text{int}}/\hbar$	$K > 1$	$K < 1$
weak impurity:	$\lambda \cos 2\theta(0)$	weak coupling	strong coupling
weak link: (strong impurity)	$\widetilde{\lambda} \cos 2\phi(0)$	strong coupling	weak coupling

For each kind of impurity they calculated via the perturbative expansion in λ in the weak coupling regime the algebraic corrections to the current voltage characteristic. However, the exact response function (D.6) allows now also to calculate the exact current voltage characteristic in the weak and strong coupling limit.

The mapping of the Luttinger liquid with impurity to the boundary sine-Gordon problem on a half line is obtained via a the non-local transformation of the fields [110] which separates the problem in a "free" Luttinger problem on a half line and a boundary sine-Gordon problem on the half line. The "free" part does not contribute to the current voltage characteristic which is determined by Eq. D.6 with

$$\frac{e}{2\pi} X = I \qquad F = \frac{eV}{\hbar}. \tag{D.14}$$

An crucial question is weather the response of the weak impurity problem in the strong coupling regime is equivalent to the response of the weak link in the weak coupling limit. The answer is again provided by duality [164] which proves that the difference between the strong impurity problem with λ and the weak link with coupling $\widetilde{\lambda}$ differs by irrelevant operators which do not contribute to the response function. As a consequence the perturbative calculation in the weak link problem provides the non-perturbative expansion in the strong coupling regime of the weak impurity problem, and vis versa.

D.2.2 Particle in periodic potential with damping

The dynamics of a superconducting Josephson junction is equivalent to a quantum particle with damping in a periodic potential and the action takes the form

$$\begin{aligned} \mathcal{S} &= \hbar \int_0^{1/T} \int_0^{1/T} d\tau d\tau' G_0^{-1}(\tau - \tau') \phi(\tau) \phi(\tau') \\ &\quad + \int_0^{1/T} d\tau \left\{ E_J \left(1 - \cos\phi(\tau)\right) - \frac{\hbar I}{e'} \phi \right\} \end{aligned} \tag{D.15}$$

with $e' = 2e$ and the propagator

$$G_0^{-1} = \frac{\hbar}{16 E_C} \omega^2 + \frac{K}{2\pi} |\omega|. \tag{D.16}$$

The last term describes a driving term appearing via current bias of the system, while E_C and E_J denote the standard charging and Josephson energies [98]. For zero driving force, the system exhibits a quantum phase transition at $K = 1$ [23, 104], where the mobility changes from diffusive behavior ($K < 1$ corresponding to weak coupling) to a localized response ($K > 1$ and strong coupling). This transition is in agreement with the result for a Luttinger liquid with a weak link. In the strong coupling case several approaches via instanton techniques provide a algebraic current-voltage characteristic [17, 99]. The action of a damped particle can be written in the form

$$\begin{aligned} \mathcal{S} &= \frac{\hbar K}{4\pi} \int_0^{1/T} d\tau \int_0^{\infty} dx \left[(\partial_\tau \phi)^2 + (\partial_x \phi)^2 \right] \\ &\quad + \int_0^{1/T} d\tau \left\{ E_J \cos\phi(0) + \frac{\hbar^2}{16 E_C} \left[\partial_\tau \phi(0)\right]^2 \right\}. \end{aligned} \tag{D.17}$$

The mass term is an irrelevant operator for $K > 0$ and drops out for low drives. The driving term takes the form

$$\mathcal{S}_F = \int_0^{1/T} d\tau \int_0^{\infty} dx \frac{\hbar I}{e'} \partial_x \phi \tag{D.18}$$

and the voltage across the weak link is obtained as a response function via the Josephson relation $V = \hbar\partial_t\phi(0)/e'$, i.e.,

$$\frac{\hbar}{e'}X = V \qquad F = \frac{2\pi I}{e'} \qquad \lambda = \frac{E_J}{\hbar}. \tag{D.19}$$

D.3 Quantitative Comparison

A comparison of the first order perturbative expansion or algebraic correction derived via instanton technique allows to determine the system depending renormalization factors $T_{\scriptscriptstyle B}$, κ, and κ'. Therefore, we expand $\mathcal{X}$ in u [164]

$$\begin{aligned} \mathcal{X} &= 1 - \sum_{n=1}^{\infty} a_n(1/K) u^{2n(1/K-1)} && \text{(D.20)} \\ \mathcal{X} &= \sum_{n=1}^{\infty} a_n(K) u^{2n(K-1)} && \text{(D.21)} \\ a_n(K) &= \frac{(-1)^{n+1}}{n!} \frac{\sqrt{\pi}}{2} \frac{\Gamma[nK+1]}{\Gamma[3/2+n(K-1)]} && \text{(D.22)} \end{aligned}$$

and compare the expansion (D.21) with the perturbative serie derived in [123]

$$I(V) = \frac{e^2 V}{2\pi K\hbar}\left[1 - \frac{\pi^2}{K\Gamma(2/K)}\left(\frac{eV}{K}\right)^{2/K-2}\left(\lambda\kappa^{-1/K}\right)\right]. \tag{D.23}$$

We obtain the relation between T'_B and the cut-off κ defined by the two-point correlation function (D.4)

$$\lambda\kappa^{-1/K} = \frac{2^{1/K}}{2\pi}\Gamma(1/K)\left(\frac{T'_{\scriptscriptstyle B}}{K}\right)^{1-1/K}. \tag{D.24}$$

Furthermore, the result derived in [99] for quantum tunneling which is a large K expansion takes the form

$$V = \frac{2\pi\hbar}{e'}\left(\frac{16E_C}{\hbar}\right)^2 \frac{\hbar}{E_J}\frac{K^{7/2}}{8\pi^{7/2}}\left(\frac{I\hbar}{e'E_J}\right)^{2K-1} \tag{D.25}$$

and is comparable to (D.20), which leads to the relation

$$\kappa = K\,\frac{4\sqrt{2}e^C}{\pi}\frac{E_C}{\hbar} \approx 1.6\,K\,\frac{E_C}{\hbar}. \tag{D.26}$$

The knowledge of these relations allows the determine the system depending renormalization factors κ' and also leads to a relation between κ and κ'.

Bibliography

[1] J. Bardeen, L. N. Cooper, and J. R. Schrieffer, Phys. Rev. **108**, 1175 (1957).

[2] L. P. Gor'kov, Sov. Phys. JETP **9**, 1364 (1959).

[3] D. R. Tilley and J. Tilley, *Superfluidity and Superconductivity*, Adam Hilger, 1990.

[4] M. H. Anderson, J. R. Ensher, M. R. Matthews, C. E. Wieman, and E. A. Cornell, Science **269**, 198 (1995).

[5] K. B. Davis et al., Phys. Rev. Lett. **75**, 3969 (1995).

[6] O. Penrose and L. Onsager, Phys. Rev. **104**, 576 (1956).

[7] J. M. Kosterlitz and D. J. Thouless, J. Phys. C **6**, 1181 (1973).

[8] J. M. Kosterlitz, J. Phys. C **7**, 1046 (1974).

[9] J. S. Langer and V. Ambegaokar, Phys. Rev. **164**, 498 (1967).

[10] D. E. McCumber, Phys. Rev. **172**, 427 (1968).

[11] J. E. Lukens, R. J. Wartburton, and W. W. Webb, Phys. Rev. Lett. **25**, 1180 (1970).

[12] R. S. Newbower, M. R. Beasley, and M. Tinkham, Phys. Rev. B **5**, 864 (1972).

[13] N. Giordano, Physica B **203**, 460 (1994).

[14] A. D. Zaikin, D. S. Golubev, A. van Otterlo, and G. T. Zimányi, Phys. Rev. Lett. **78**, 1552 (1997).

[15] I. Affleck, Phys. Rev. Lett. **46**, 388 (1981).

[16] H. Grabert and U. Weiss, Phys. Rev. Lett. **52**, 2193 (1984).

[17] A. O. Caldeira and A. J. Leggett, Ann. Phys. (N.Y.) **149**, 374 (1983).

[18] A. I. Larkin and Y. N. Ovchinnikov, Sov. Phys. JETP **86**, 420 (1983).

[19] G. Schön and A. D. Zaikin, Phys. Rep. **198**, 237 (1990).

[20] R. F. Voss and R. A. Webb, Phys. Rev. Lett. **47**, 265 (1981).

[21] M. H. Devoret, J. M. Martinis, and J. Clarke, Phys. Rev. Lett. **55**, 1908 (1985).

[22] J. M. Martinis, M. H. Devoret, and J. Clarke, Phys. Rev. B **35**, 4682 (1987).

[23] A. Schmid, Phys. Rev. Lett. **51**, 1506 (1983).

[24] A. J. Leggett et al., Rev. Mod. Phys. **59**, 1 (1987).

[25] J. S. Penttilä, Ü. Parts, P. J. Hakonen, M. A. Paalanen, and E. B. Sonin, Phys. Rev. Lett. **82**, 1004 (1999).

[26] M. Watanabe and D. B. Haviland, Phys. Rev. Lett. **86**, 5120 (2001).

[27] A. J. V. Run, J. Romijn, and J. E. Mooij, Jpn. J. Appl. Phys. **26**, 1765 (1987).

[28] S. Saito and Y. Murayama, Phys. Lett. A **135**, 55 (1989).

[29] S. Saito and Y. Murayama, Phys. Lett. A **139**, 85 (1989).

[30] J. M. Duan, Phys. Rev. Lett. **74**, 5128 (1995).

[31] A. van Otterlo, D. S. Golubev, A. D. Zaikin, and G. Blatter, Eur. Phys. J. B **10**, 131 (1999).

[32] J. E. Mooij and G. Schön, Phys. Rev. Lett. **55**, 114 (1985).

[33] B. Camarota, F. Parage, F. Balestro, P. Delsing, and O. Buisson, Phys. Rev. Lett. **86**, 480 (2001).

[34] V. A. Kashurnikov, A. I. Podlivaev, N. V. Prokof'ev, and B. V. Svistunov, Phys. Rev. B **53**, 13091 (1996).

[35] F. W. J. Hekking and L. I. Glazman, Phys. Rev. B **55**, 6551 (1997).

[36] P. Xiong, A. V. Herzog, and R. C. Dynes, Phys. Rev. Lett. **78**, 927 (1997).

[37] F. Sharifi, A. V. Herzog, and R. C. Dynes, Phys. Rev. Lett. **71**, 428 (1993).

[38] J. M. Duan, Phys. Rev. Lett. **79**, 3316 (1997).

[39] A. D. Zaikin, D. S. Golubev, A. van Otterlo, and G. T. Zimányi, Phys. Rev. Lett. **79**, 3317 (1997).

[40] A. Bezryadin, C. N. Lau, and M. Tinkham, Nature **404**, 971 (2000).

[41] C. N. Lau, N. Markovic, M. Bockrath, A. Bezryadin, and M. Tinkham, Phys. Rev. Lett. **87**, 217003 (2001).

[42] D. S. Golubev and A. D. Zaikin, Phys. Rev. B **64**, 014504 (2001).

[43] D. B. Haviland, Y. Liu, and A. M. Goldman, Phys. Rev. Lett. **62**, 2180 (1989).

[44] A. M. Finkel'stein, Physica B **197**, 636 (1994).

[45] S. Maekawa and H. Fukuyama, J. Phys. Soc. Jpn. **51**, 1380 (1982).

[46] H. Takagi and Y. Kuroda, Solid State Commun. **41**, 643 (1982).

[47] M. P. A. Fisher, P. B. Weichman, G. Grinstein, and D. S. Fisher, Phys. Rev. B **40**, 546 (1989).

[48] M. P. A. Fisher, Phys. Rev. Lett. **65**, 923 (1990).

[49] A. Larkin, Ann. Phys. (Leipzig) **8**, 785 (1999).

[50] Y. Oreg and E. Demler, eprint **cond-mat/0106645**, 0 (2001).

[51] Y. Oreg and A. M. Finkel'stein, Phys. Rev. Lett. **83**, 191 (1999).

[52] R. A. Smith, B. S. Handy, and V. Ambegaokar, Phys. Rev. B **63**, 094513 (2001).

[53] S. Bose, Z. Phys. **26**, 178 (1924).

[54] A. Einstein, Sitzungber. Preuss. Akad. Wiss. **1925**, 3 (1925).

[55] W. Ketterle and N. J. van Druten, Phys. Rev. A **54**, 656 (1996).

[56] A. J. Leggett, Rev. Mod. Phys. **73**, 307 (2001).

[57] J. L. Roberts et al., Phys. Rev. Lett. **81**, 5109 (1998).

[58] J. Stenger et al., Phys. Rev. Lett. **82**, 2422 (1999).

[59] S. L. Cornish, N. R. Claussen, J. L. Roberts, E. A. Cornell, and C. E. Wieman, Phys. Rev. Lett. **85**, 1795 (2000).

[60] F. Dalfovo, S. Giorgini, L. P. Pitaevksii, and S. Stringari, Rev. Mod. Phys. **71**, 463 (1999).

[61] C. Raman et al., Phys. Rev. Lett. **83**, 2502 (1999).

[62] R. Onofrio et al., Phys. Rev. Lett. **85**, 2228 (2000).

[63] T. Winiecki, J. F. McCann, and C. S. Adams, Phys. Rev. Lett. **82**, 5186 (1999).

[64] J. S. Stiessberger and W. Zwerger, Phys. Rev. A **61**, 061601 (2000).

[65] M. R. Matthews et al., Phys. Rev. Lett. **83**, 2498 (1999).

[66] K. W. Madison, F. Chevy, W. Wohlleben, and J. Dalibard, Phys. Rev. Lett. **84**, 806 (2000).

[67] J. R. Abo-Shaeer, C. Raman, J. M. Vogels, and W. Ketterle, Science **292**, 476 (2001).

[68] D. Jaksch, C. Bruder, J. I. Cirac, C. W. Gardiner, and P. Zoller, Phys. Rev. Lett. **81**, 3108 (1998).

[69] M. Greiner, O. Mandel, T. Esslinger, T. W. Hänsch, and I. Bloch, Nature **415**, 39 (2002).

[70] M. Greiner*, et al.*, Nature **419**, 51 (2002).

[71] M. Girardeau, J. Math. Phys. **1**, 516 (1960).

[72] E. H. Lieb and W. Liniger, Phys. Rev. **130**, 1605 (1963).

[73] E. H. Lieb, Phys. Rev. **130**, 1616 (1963).

[74] D. S. Petrov, G. V. Shlyapnikov, and J. T. M. Walraven, Phys. Rev. Lett. **85**, 3745 (2000).

[75] M. Olshanii, Phys. Rev. Lett. **81**, 938 (1998).

[76] V. Dunjko, V. Lorent, and M. Olshanii, Phys. Rev. Lett. **86**, 5413 (2001).

[77] M. D. Girardeau and E. M. Wright, Phys. Rev. Lett. **84**, 5239 (2000).

[78] M. D. Girardeau and E. M. Wright, Phys. Rev. Lett. **87**, 05043 (2001).

[79] M. D. Girardeau and E. M. Wright, Phys. Rev. Lett. **87**, 210401 (2001).

[80] K. Kanual, M. D. Girardeau, and E. M. Wright, Phys. Rev. Lett. **89**, 110402 (2002).

[81] A. Görlitz et al., Phys. Rev. Lett. **87**, 130402 (2001).

[82] W. Hänsel, P. Hommelhoff, T. W. Hänsch, and J. Reichel, Nature **413**, 498 (2001).

[83] H. Ott, J. Fortagh, G. Schlotterbeck, A. Grossmann, and C. Zimmermann, Phys. Rev. Lett. **87**, 230401 (2001).

[84] R. Folman et al., Phys. Rev. Lett. **84**, 4749 (2000).

[85] M. Greiner, I. Bloch, O. Mandel, T. W. Hänsch, and T. Esslinger, Phys. Rev. Lett. **87**, 160405 (2001).

[86] A. G. Truscott, K. E. Strecker, W. I. McAlexander, G. B. Partridge, and R. G. Hulet, Science **291**, 2570 (2001).

[87] F. Schreck et al., Phys. Rev. Lett. **87**, 080403 (2001).

[88] Z. Hadzibabic et al., Phys. Rev. Lett. **88**, 160401 (2002).

[89] G. Roati, F. Riboli, G. Modugno, and M. Inguscio, Phys. Rev. Lett. **89**, 150403 (2002).

[90] K. Mølmer, Phys. Rev. Lett. **80**, 1804 (1998).

[91] L. Viverit, C. J. Pethick, and H. Smith, Phys. Rev. A **61**, 053605 (2000).

[92] G. Modugno et al., Science **297**, 1320 (2002).

[93] M. Houbiers, R. Ferwerda, and H. T. C. Stoof, Phys. Rev. A **56**, 4864 (1997).

[94] L. Viverit, Phys. Rev. A **65**, 021605 (2002).

[95] W. Hofstetter, J. I. Cirac, P. Zoller, E. Demler, and M. D. Lukin, Phys. Rev. Lett. **89**, 220407 (2002).

[96] M. H. Devoret et al., Phys. Rev. Lett. **64**, 1824 (1990).

[97] G. L. Ingold and H. Grabert, Phys. Rev. Lett. **83**, 3721 (1999).

[98] M. Tinkham, *Introduction to Superconductivity*, McGraw-Hill, 1996.

[99] S. E. Korshunov, Sov. Phys. JETP **65**, 1025 (1987).

[100] F. D. M. Haldane, Phys. Rev. Lett. **47**, 1840 (1981).

[101] D. S. Golubev and A. D. Zaikin, Phys. Rev. B **64**, 014504 (2001).

[102] V. L. Berezinksii, Sov. Phys. JETP **34**, 610 (1971).

[103] A. M. Tsvelik, *Quantum Field Theory in Condensed Matter Physics*, Cambridge University Press, 1995.

[104] S. A. Bulgadaev, Sov. Phys. JETP Lett. **39**, 317 (1984).

[105] P. W. Anderson, G. Yuval, and D. R. Hamann, Phys. Rev. B **1**, 4464 (1970).

[106] P. W. Anderson and G. Yuval, J. Phys. C **4**, 607 (1971).

[107] S. Coleman, Phys. Rev. D **16**, 2929 (1977).

[108] C. G. Callan and S. Coleman, Phys. Rev. D **16**, 1762 (1977).

[109] U. Weiss, H. Grabert, P. Hänggi, and P. Riseborough, Phys. Rev. B **35**, 9535 (1987).

[110] P. Fendley, A. W. W. Ludwig, and H. Saleur, Phys. Rev. B **52**, 8934 (1995).

[111] G. Schön, Nature **404**, 948 (2000).

[112] L. D. Landau, J. Phys. U.S.S.R. **5**, 71 (1941).

[113] T. Frisch, Y. Pomeau, and S. Rica, Phys. Rev. Lett. **69**, 1644 (1992).

[114] V. Hakim, Phys. Rev. E **55**, 2835 (1997).

[115] S. Giovanazzi, A. Smerzi, and S. Fantoni, Phys. Rev. Lett. **84**, 4521 (2000).

[116] B. Jackson, J. F. McCann, and C. S. Adams, Phys. Rev. A **61**, 051603 (2000).

[117] J. Reichel, W. Hänsel, and T. W. Hänsch, Phys. Rev. Lett. **83**, 3398 (1999).

[118] M. Greiner, I. Bloch, O. Mandel, T. W. Hänsch, and T. Esslinger, Phys. Rev. Lett. **87**, 160405 (2001).

[119] Y. Kagan, V. N. Prokof'ev, and B. V. Svistunov, Phys. Rev. A **61**, 045601 (2000).

[120] H. P. Büchler, V. B. Geshkenbein, and G. Blatter, Phys. Rev. Lett. **87**, 100403 (2001).

[121] J. W. Negele and H. Orland, *Quantum Many-Particle Systems*, Perseus Books, Massachusetts, 1998.

[122] N. Bogoliubov, J. Phys **11**, 23 (1947).

[123] C. L. Kane and M. P. A. Fisher, Phys. Rev. Lett. **68**, 1220 (1992).

[124] J. H. Davies and J. W. Wilkins, Phys. Rev. B **38**, 1667 (1988).

[125] K. K. Likharev and A. B. Zorin, J. Low Temp. Phys. **59**, 347 (1985).

[126] G. D. Mahan, *Many-Particle Physics*, Plenum Press, New York, 1990.

[127] H. P. Büchler, G. Blatter, and W. Zwerger, Phys. Rev. Lett. **90**, 130401 (2003).

[128] W. Krauth, M. Caffarel, and J.-P. Bouchaud, Phys. Rev. B **45**, 3137 (1992).

[129] T. D. Kühner and H. Monien, Phys. Rev. B **58**, R14741 (1998).

[130] S. Rapsch, U. Schollwöck, and W. Zwerger, Europhys. Lett. **46**, 559 (1999).

[131] S. Coleman, Phys. Rev. D **11**, 2088 (1975).

[132] A. Luther, Phys. Rev. B **15**, 403 (1977).

[133] P. B. Wiegmann, J. Phys. C **11**, 1583 (1978).

[134] G. I. Japaridze and A. A. Nersesyan, Nucl. Phys. B **230**, 511 (1984).

[135] A. O. Gogolin, A. A. Neresyan, and A. m. Tsvelik, *Bosonization and Strongly Correlated Systems*, Cambridge University Press, 1998.

[136] S. Kehrein, Phys. Rev. Lett. **83**, 4914 (1999).

[137] S. Kehrein, Nucl. Phys. B **592**, 512 (2001).

[138] V. L. Pokrovsky and A. L. Talapov, Phys. Rev. Lett. **42**, 65 (1979).

[139] M. Abramowitz and I. A. Stegun, *Handbook of Mahtematical Functions*, Dover Publications, New York, 1972.

[140] H. J. Schulz, Phys. Rev. B **22**, 5274 (1980).

[141] J. Villain, Theories of commensurate-incommensurate transitions on surfaces, in *Ordering in Two Dimensions*, edited by S. K. Shina, page 123, North Holland, 1980.

[142] G. Girkl, M. Gatzke, I. H. Deutsch, S. L. Rolston, and W. D. Phillips, Phys. Rev. Lett. **75**, 2823 (1995).

[143] M. Weidemüller, A. Hemmerich, A. Görlitz, T. Esslinger, and T. W. Hänsch, Phys. Rev. Lett. **75**, 4583 (1995).

[144] A. F. Andreev and I. M. Lifshitz, Sov. Phys. JETP **29**, 1107 (1967).

[145] A. J. Leggett, Phys. Rev. Lett. **25**, 1543 (1970).

[146] G. A. Lengua and J. M. Goodkind, J. Low Temp. Phys. **79**, 251 (1990).

[147] M. W. Meisel, Physica B **178**, 121 (1992).

[148] G. G. Batrouni, R. R. Scalettar, G. T. Zimanyi, and A. P. Kampf, Phys. Rev. Lett. **74**, 2527 (1995).

[149] E. Frey and L. Balents, Phys. Rev. B **55**, 1050 (1997).

[150] G. G. Batrouni and R. R. Scalettar, Phys. Rev. Lett. **84**, 1599 (2000).

[151] K. Góral, L. Santos, and M. Lewenstein, Phys. Rev. Lett. **88**, 170406 (2002).

[152] G. Grüner, *Density Waves in Solids*, Perseus Publishing, Cambridge, Massachusetts, 2000.

[153] M. Amoruso, A. Minguzzi, S. Stringari, M. P. Tosi, and L. Vichi, Eur. Phys. J. D **4**, 261 (1998).

[154] D. Y. Xing, M. Liu, and C. D. Gong, Phys. Rev. B **44**, 12525 (1991).

[155] A. A. Abrikosov, L. P. Gorkov, and I. E. Dzyaloshinski, *Methods of Quantum Field Theory in Statistical Physics*, Dover Publications, Inc., 180 Varick Street, New-York 10014, 1963.

[156] J. E. Hirsch and D. J. Scalapino, Phys. Rev. Lett. **56**, 2732 (1986).

[157] I. S. Gradshteyn and I. M. Ryshik, *Table of Integrals, Series, and Products*, Academic Press, San Diego, 1980.

[158] J. S. Langer, Ann. Phys. (N.Y.) **41**, 108 (1967).

[159] S. A. Bulgadaev, Phys. Lett. A **86**, 213 (1981).

[160] S. Ghoshal and A. Zamolodchikov, Int. J. Mod. Phys. A **9**, 3841 (1994).

[161] P. Fendley, H. Saleur, and N. P. Warner, Nucl. Phys. B **430**, 577 (1994).

[162] P. Fendley, F. Lesage, and H. Saleur, J. of Stat. Phys. **79**, 799 (1995).

[163] C. L. Kane and M. P. A. Fisher, Phys. Rev. B **46**, 15233 (1992).

[164] P. Fendley and H. Saleur, Phys. Rev. Lett. **81**, 2518 (1998).

Acknowledgments

It is great pleasure to express my gratitude to my supervisor Gianni Blatter. He was an excellent supervisor and I had many extensive and interesting discussions with him. I also would like to thank Dima Geshkenbein for interesting collaborations and his introduction to the 'russian style' of solving problems. A special thank also goes to Willi Zwerger with whom I enjoyed many fascinating discussions during his sabbatical at ETH Zürich, and who provided many suggestions for interesting problems. I owe a dept of gratitude to Tilman Esslinger who introduced me into the experimental techniques of creating Bose-Einstein condensates and who organized many interesting contacts and discussions. I would like to thank H. Katzgraber, G. Zimáni, L. Bulaevskii, P. Martinoli, V. Vinokur , L. Levitov, M. Tinkham and L. Glazman for organizing my visits to UC Santa Cruz, UC Davis, Los Alamos National Laboratory, Univeristy of Neuchâtel, Argonne National Laboratory, MIT, Harvard Univserity, and University of Minneapolis. I owe my gratitude to M. Rice, M. Sigrist, M. Troyer, T. Ihn, D. Ivanov, M. Dogdson ,W. Ketterle, P. Young, A. Zaikin, A. Bezryadin, M. Paalanen, M. Köhl for interesting discussions. A special thanks go to all my office mates Rolf Heeb, Malek Bou-Diab, Daniel Kuhn, Jérôme Koopmann, and H. Katzgraber. We always enjoyed a special atmosphere in the E8 with a lot of fun but also hard work and extensive discussions. I also seize the opportunity to thank my colleagues and friends Mathias Körner, Dominic Rau, A. Läuchli. and G. Schmid, and Samuel Wehrli, and to express my gratitude to my parents who supported my during my study. Finally, I owe a very special thank to my best friend Brigitte Oberholzer who always opened my eyes to the beauty in the world, which gave me a lot of strength in writing this thesis.

CURRICULUM VITAE

Personal Data

Name:	Hans Peter Büchler
Born:	December 5, 1973 (Wattwil, Switzerland)
Nationality:	Swiss citizen (St. Peterzell/SG and Zürich/ZH)

Education

1981 –1989	Primary and secondary school in Wattwil
1989 –1994	Kantonsschule in Wattwil Final degree: Matura
19/1994 - 10/1998	Undergraduate studies in physics at the Swiss Federal Institute of Technology Zürich (ETH-Zürich)
10/1999 - 10/1999	Diploma thesis on “Macroscopic Quantum Phenomena in Superconducting Structures” at the Institute of Theoretical Physics, ETH-Zürich under the supervision of Prof. G. Blatter
4/1999	Diploma in theoretical physics with distinction
7/1999 - 4/2003	Graduate studies at the Institute of Theoretical Physics at the ETH-Zürich under the supervision of Prof. G. Blatter